

AD-A274 357

TURBULENT BOUNDARY LAYER INNER-OUTER INTERACTIONS

by

David G. Bogard, Choon L. Gan and Atul Kohli

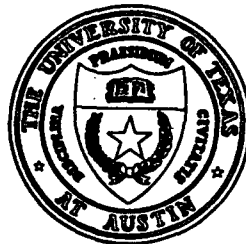
Report TTCRL 93-4

Final Report for August 1, 1989 to December 31, 1992

S DTIC  
ELECTE  
JAN 05 1994  
A

Submitted to  
Office of Naval Research  
800 North Quincy Street  
Arlington, Virginia 22217-5000

This document has been approved  
for public release and sale; its  
distribution is unlimited.



Turbulence and Turbine Cooling Research Laboratory  
Department of Mechanical Engineering  
The University of Texas at Austin  
Austin, Texas 78712

December 1993

94-00099

97 1 08 024

Unclassified

CLASSIFICATION OF THIS PAGE

Form Approved  
OMB No. 0704-0188

## REPORT DOCUMENTATION PAGE

1a. REPORT SECURITY CLASSIFICATION Unclassified		1d. RESTRICTIVE MARKINGS	
2a. SECURITY CLASSIFICATION AUTHORITY		3. DISTRIBUTION/AVAILABILITY OF REPORT Approved for public release; distribution unlimited	
2b. DECLASSIFICATION/DOWNGRADING SCHEDULE			
4. PERFORMING ORGANIZATION REPORT NUMBER(S) TTCRL 93-4		5. MONITORING ORGANIZATION REPORT NUMBER(S)	
6a. NAME OF PERFORMING ORGANIZATION University of Texas	6b. OFFICE SYMBOL (If applicable)	7a. NAME OF MONITORING ORGANIZATION Office of Naval Research	
6c. ADDRESS (City, State, and ZIP Code) Department of Mechanical Engineering The University of Texas at Austin Austin, Texas 78712-1063		7b. ADDRESS (City, State, and ZIP Code) Fluid Mechanics, Code 1132F Arlington, VA 22217-5000	
6a. NAME OF FUNDING/SPONSORING ORGANIZATION	8b. OFFICE SYMBOL (If applicable)	9. PROCUREMENT INSTRUMENT IDENTIFICATION NUMBER N00014-89-J-1701	
8c. ADDRESS (City, State, and ZIP Code)		10. SOURCE OF FUNDING NUMBERS	
		PROGRAM ELEMENT NO.	PROJECT NO.
		TASK NO.	WORK UNIT ACCESSION NO.
11. TITLE (Include Security Classification) Turbulent Boundary Layer Inner-Outer Interactions (unclassified)			
12. PERSONAL AUTHOR(S) Bogard, David Guy; Gan, Choon Lim and Kohli, Atul			
13a. TYPE OF REPORT Final	13b. TIME COVERED FROM 890801 TO 921231	14. DATE OF REPORT (Year, Month, Day) 931206	15. PAGE COUNT 187
16. SUPPLEMENTARY NOTATION			
17. COSATI CODES		18. SUBJECT TERMS (Continue on reverse if necessary and identify by block number) Scanning laser Doppler velocimeter, burst, sweep, shear layer, large scale structure, conditional sampling, rough wall, LEBU device, convection velocity, spatial detection, two and three dimensional mapping.	
FIELD	GROUP	19. ABSTRACT (Continue on reverse if necessary and identify by block number) A summary of work performed to study the interactions between the inner and outer regions of a turbulent boundary layer is presented. The interactions were studied by observing the response of the boundary layer to different perturbations. The inner region was modified by adding surface roughness, and the outer region suppressed using LEBU's. Velocity measurements were made with a three component LDV, a scanning LDV, and an X-type hot-film probe. The scanning LDV was developed to obtain continuous time history measurements of instantaneous velocity profiles down to $y^+ = 10$ . Details of the structure of bursts, sweeps, and shear layers over smooth and rough walls were determined using conditional sampling with simultaneous measurements from a detector probe and a mapping probe. This allowed the mapping of the complete three-dimensional structure of the three-component velocity field for these structures. Both single point detection, using quadrant and VITA techniques, and a unique spatially coherent structure detection technique were used. The spatial detection technique developed in this project takes advantage of the two-dimensional velocity field information obtained from the scanning LDV. These multi-	
20. DISTRIBUTION/AVAILABILITY OF ABSTRACT <input checked="" type="checkbox"/> UNCLASSIFIED/UNLIMITED <input type="checkbox"/> SAME AS RPT <input type="checkbox"/> DTIC USES		21. ABSTRACT SECURITY CLASSIFICATION Unclassified	
22a. NAME OF RESPONSIBLE INDIVIDUAL Dr. L. P. Purcell		22b. TELEPHONE (Include Area Code) (703) 696-4405	22c. OFFICE SYMBOL N00014

19.

sensor experiments also allowed us to track the streamwise movement of the structure and thereby determine convection velocities. Characteristics of bursts were found to be similar at different detection heights, with a slight increase in size with increase in height. Spatially resolved conditional samples showed large scale high speed fluid associated with bursts over smooth walls but not for rough walls. These results suggest an outer stimulus to bursts for smooth walls that is not evident for rough walls. The variation of convection velocities of the burst, sweep, and shear layer events over the smooth wall indicates that these events are essentially independent events. The rough wall, which more than doubled the near wall turbulent shear stress, produced an almost immediate increase in the burst strength, but no change in the burst or ejection frequency, or the burst duration. There were significant changes in the spatial structure of bursts, sweeps, and shear layers over the rough wall.

DTIC QUALITY INSPECTED 5

Accession For	
NTIS (CRASH)	<input checked="" type="checkbox"/>
DTIC TAG	<input type="checkbox"/>
Unannounced	<input type="checkbox"/>
Justification:	
By _____	
Distribution /	
Availability (check)	
Dist	Aval. and/or Special
A-1	

## Table of Contents

<b>List of Figures</b>	<b>ii</b>
<b>1. Overview</b>	<b>1</b>
<b>2. Research Goals</b>	<b>2</b>
<b>3. Task Descriptions and Results</b>	<b>3</b>
<b>3.1. Development of the Scanning LDV</b>	<b>3</b>
<b>3.2. Evolution of Large Scale Structures</b>	<b>5</b>
<b>3.3. Mapping of Turbulent Structures: Smooth Wall</b>	<b>6</b>
<b>3.4. Conditional Sampling Using Spatial Detection</b>	<b>11</b>
<b>3.5. Effects of Rough Surfaces and LEBU devices on Turbulent Structure</b>	<b>14</b>
<b>3.5.1. Rough Surface Effects</b>	<b>14</b>
<b>3.5.2. LEBU Device Effects</b>	<b>17</b>
<b>3.5.3. Comparison of the Effects of the LEBU Device and Rough Surfaces on Turbulent Structure</b>	<b>18</b>
<b>4. Conclusions</b>	<b>20</b>
<b>References</b>	<b>22</b>
<b>Appendix A. Detection of Coherent Structures in Smooth and Rough Wall Turbulent Boundary Layer Flows Using a Scanning LDV System</b>	<b>55</b>

## List Of Figures

**Figure 1(a)** Scanning mean velocity profile compared with profile from stationary measurements and Spalding's Law. 23

**Figure 1(b)** Scanning rms profile compared with rms profiles from stationary measurements, Gan (1989) and Purtell et al. (1981). 23

**Figure 2** Quadrant burst detected at  $y_d^+ = 30$ ,  $u^+$  velocity contour levels. (a) x based on time history measurements and a convection velocity, (b) direct spatial measurement. 24

**Figure 3** Quadrant burst detected at  $y_d^+ = 30$ ,  $u-v$  fluctuating velocities relative to burst convection velocity. (a) Based on time history measurements and a convection velocity, (b) direct spatial measurement. 25

**Figure 4** Quadrant burst detected at  $y_d^+ = 60$ , direct spatial measurement of  $u^+$  velocity defect contour levels. 26

**Figure 5** Spanwise cross-sections of quadrant bursts detected at: (a)  $y_d^+ = 30$  and (b)  $y_d^+ = 60$ .  $u^+$  contour levels. 27

**Figure 6** Spanwise cross-sections of quadrant bursts detected at: (a)  $y_d^+ = 30$  and (b)  $y_d^+ = 60$ .  $v^+$  contour levels. 28

**Figure 7** Spanwise cross-sections of quadrant bursts detected at: (a)  $y_d^+ = 30$  and (b)  $y_d^+ = 60$ .  $uv^+$  contour levels. 29

**Figure 8(a)** Spanwise cross-section of the quadrant burst detected at  $y_d^+ = 30$ .  $v-w$  velocity vectors. 30

**Figure 8(b)** Spanwise cross-section of the quadrant burst detected at  $y_d^+ = 60$ .  $v-w$  velocity vectors. 31

<b>Figure 9</b>	Evolution of uv contours for a quadrant burst detected at $y_d^+ = 30$ . Contour increments of $(uv)^+ = 0.6$ .	32
<b>Figure 10</b>	Ensemble averaged u velocity signal associated with the shear layer event detected at $y^+ = 30$ . Contour increments of $u^+ = 0.4$ .	33
<b>Figure 11</b>	Convection velocities of the burst, sweep, and shear layer event detected at $y^+ = 20, 30$ , and $60$ .	34
<b>Figure 12</b>	Time sequence of v-w velocity vectors for a quadrant burst detected at $y_d^+ = 30$ . Conditional samples centered on maximum -uv.	35
<b>Figure 13</b>	Time sequence of v-w velocity vectors for a quadrant burst detected at $y_d^+ = 30$ . Conditional samples centered on the leading edge of the uv pulse.	36
<b>Figure 14</b>	Time sequence of v-w velocity vectors for a quadrant burst detected at $y_d^+ = 30$ . Conditional samples centered on the trailing edge of the uv pulse.	37
<b>Figure 15</b>	Time sequence of v-w velocity vectors for a quadrant sweep detected at $y_d^+ = 30$ . Conditional samples centered on maximum -uv.	38
<b>Figure 16</b>	Time sequence of v-w velocity vectors for a VITA shear layer detected at $y_d^+ = 30$ . Conditional samples aligned with the center of the VITA event.	39
<b>Figure 17</b>	Schematic for the grouping of events using the spatial detection technique. Separate spatial structures indicated by dashed lines.	40
<b>Figure 18</b>	Low speed events over a smooth wall. Conditional samples based on spatial detection. Indicated heights are a classification of events in terms of the maximum height of the event.	41

**Figure 19** Profiles of  $\bar{uv}$  immediately upstream of the rough surface,  $x = -\delta_0$ , following the start of roughness,  $x = 2\delta_0$ , and in the fully developed rough wall flow,  $x = 24\delta_0$ . 42

**Figure 20** Effect of position with respect to the roughness elements on the  $\bar{uv}$  profiles for fully developed rough wall flow. 43

**Figure 21** Effect of the rough surface on the (a) ejection and (b) burst frequencies. Quadrant detection with threshold  $H = 1.0u'v'$ . 44

**Figure 22** Nondimensional (a) ejection and (b) burst frequencies for smooth and rough surfaces using outer variables. Quadrant detection with threshold  $H = 1.0u'v'$ . 45

**Figure 23** Effect of the rough surface on the ensemble average of the conditionally sampled  $uv$  signal. Measurements and detection made with same probe located in the near wall constant stress layer. Quadrant detection with threshold  $H = 1.0u'v'$ . 46

**Figure 24** Low speed events over a rough and smooth wall. Conditional samples based on spatial detection. Indicated heights are a classification of events in terms of the maximum height of the event. Results are presented in terms of outer variables. An appropriate convection velocity was used to obtain  $x_c$  ( $x_c = t.U_c$ ). 47

**Figure 25** Ensemble averaged conditional samples of smooth and rough wall bursts, with the time scale normalized by burst duration. Quadrant detection with threshold  $H = 1.0u'v'$ . 48

**Figure 26** Ensemble averaged conditional samples of smooth and rough wall shear layer events with averaging time based on burst duration. VITA detection with positive slope criterion and threshold  $k = 1.0u'$ . 49

**Figure 27** Convection velocities of the burst, sweep, and shear layer over the rough wall, and smooth wall with and without the LEBU device. Convection velocities relative to the convection velocity of the smooth wall burst without LEBU device. 50

**Figure 28** Ensemble averaged conditional samples of u velocity contours of the Quadrant burst over a smooth wall with and without the LEBU device, and over a rough wall. Length scales normalized by the length of the burst. Contour levels normalized by the burst convection velocity. 51

**Figure 29** Ensemble averaged conditional samples of u velocity contours of the Quadrant sweep over a smooth wall with and without the LEBU device, and over a rough wall. Length scales normalized by the length of the burst. Contour levels normalized by the burst convection velocity. 52

**Figure 30** Ensemble averaged conditional samples of u velocity contours of the VITA shear layer over a smooth wall with and without the LEBU device, and over a rough wall. Length scales normalized by the length of the burst. Contour levels normalized by the burst convection velocity. 53

**Figure 31** Comparison of the ensemble averaged conditional samples of shear layer events for the (a) smooth wall and (b) rough wall, detected with and without a positive slope criterion. 54

## **1. Overview**

The goal of this project was to develop a better understanding of the physics of turbulent boundary layer structures. In particular, the interactions between the inner and outer regions of the boundary layer were investigated by observing the response of the boundary layer to different perturbations. The wall region of the boundary layer was modified by adding surface roughness, and the outer region suppressed using LEBU's. Changes in the mean turbulence statistics and the conditionally sampled turbulent structures were studied to obtain a better understanding of the dynamics of the inner and outer structures.

A major component of this research was the development of a scanning LDV system which allowed us to make continuous time history measurements of instantaneous velocity profiles in the near wall region of the boundary layer. Velocity fields measured with the scanning LDV were analyzed using a unique spatial structure detection technique which allowed us to identify spatially coherent structures and resolve them in terms of size and distance from the wall.

Initial experiments were conducted to complete a detailed three-dimensional mapping of the burst, sweep, and shear layer structures over a smooth wall. These results were obtained using conditional sampling with simultaneous measurements from a two-component hot-film probe and a three-component LDV. Details of the evolution of these structures upstream and downstream of the detector probe, and at different heights from the wall have been determined.

For the case of smooth-to-rough transition, the rough surface had an equivalent wall shear that was double that for the smooth surface. Although pressure loads on the roughness elements dominate at the surface, these pressure loads must be balanced by significant increases in turbulent shear stresses immediately above the roughness elements. A primary goal of the project was to determine how the inner and outer structures adjust to produce the sudden increase in shear stress. The characteristics of the turbulence for the smooth wall before the start of the roughness were contrasted with changes in the turbulence at the start of roughness, and with changes for the fully developed rough wall flow.

## **2. Research Goals**

The fundamental goal of this research was to obtain a better understanding of the interaction between large scale outer structures and

small scale inner structures. The basis of the experimental program to achieve this goal was to perturb the inner structure using surface roughness and determine the effects on inner and outer structures. Similarly the outer structure was perturbed using a large eddy break-up (LEBU) device and effects on the inner and outer structure were determined with flow over a smooth surface. Three-dimensional spatial characteristics of bursts and sweeps (inner structures) were measured using simultaneous three-component laser Doppler velocimetry (LDV) and hot-film anemometry (X-type probe). A key measurement tool used in this study was the scanning LDV system. Another goal of this project was to further develop the scanning LDV system, and this system was used to measure essentially instantaneous velocity profiles.

The project was divided into five tasks. These tasks and specific goals for the these tasks were as follows:

1. Development of the scanning LDV system. Prior to this project, the scanning LDV system had been developed to the point of making velocity profile measurements in the wake of a cylinder. The goals of this task were to develop the capability of scanning boundary layer profiles down to at least  $y^+ = 15$ , and at a rate such that essentially instantaneous velocity profiles would be obtained with continuous time records. Also, sufficient spatial resolution to define structures as small as  $\Delta y^+ = 10$  was required. We also wanted to modify the system so that two-component measurements could be made.
2. Flow visualization study of the evolution of large-scale structures. Previous studies of large-scale structures were restricted to measurements or visualization of the structures as they passed some point in the flow. The goal of this task was to develop and implement flow visualization techniques which could track the large-scale structures over an extended distance allowing us to follow the evolution of the structures.
3. Three-dimensional mapping of bursts and sweeps over a smooth surface. This task was essentially a completion of work started in an earlier ONR contract to use conditional sampling techniques to obtain detailed three-dimensional characteristics of bursts. The goals of this task were to extend the conditional sampling analysis to sweep and shear layer structures, to evaluate the sensitivity to detector height, and to determine convection velocities of each of the structures as a function of distance from the wall.
4. Conditional sampling using spatial detection. The two-dimensional velocity field information available from the scanning LDV system allowed us to implement a unique spatial detection technique for conditional sampling analysis. The goals of this task were to develop the spatial detection techniques, then use these techniques to

investigate the burst and sweep structures at different stages of evolution.

## 5. Effects of rough surfaces and LEBU devices on turbulent structure.

- (i) Rough surface effects. This was a major part of this research program. The sudden increase in turbulent shear stress at the wall, and how the inner and outer structures adjusted to accommodate this increase, would provide new insight into the dynamics of these structures. The goals of this task were to obtain single point and scanning LDV measurements immediately following the smooth to rough transition and downstream in the fully development rough wall flow. These measurements were to be analyzed using conditional sampling techniques to educe changes in the turbulent structures.
- (ii) LEBU effects on smooth surfaces. The LEBU device tends to isolate the near wall region from the outer structures. Using the LEBU with would allow us to determine the importance of the outer structures. The goals of this task were to use conditional sampling techniques to educe changes in the inner structures when the LEBU device was implemented.

## 3. Task Descriptions and Results

### 3.1. Development of the Scanning LDV

The goal of this task was to develop the scanning LDV system to the point where it was a reliable tool for making continuous time history instantaneous velocity profiles of a boundary layer flow. A further improvement to be attempted was to modify the system so that two-component measurements could be made.

Development of scanning LDV system to the point that continuous time history boundary layer velocity profiles measurements were made is described by Bolton (1990) and by Bolton and Bogard (1992). Improvements to the near wall measurement capability of the scanning LDV system so that measurements down to at least  $y^+ = 15$  could be made, and improvements to the accuracy of the probe volume positioning are discussed in detail in the thesis by Kohli (1992) which is attached to this report as Appendix A.

Typical operational parameters for the scanning LDV system are listed in Table 1. By taking care to eliminate reflection of laser beams at the wall, which would saturate the photomultiplier tube, measurements were made

down to  $y^+ = 10$ . New alignment procedures for the scanning mirrors were also developed which improved the accuracy of the scanning measurements. Finally, a displacement transducer was attached to the scanning mirror and a dynamic calibration procedure was developed which resulted in a positioning accuracy of  $\pm 0.2$  mm. The accuracy of the scanning measurements is indicated by the mean and rms velocity profiles shown in Figures 1 (a) and (b), which show excellent agreement with single point measurements. Note, that the rms velocity measurements are a particularly good test of the accuracy of the scanning LDV system because any vibration effects would be revealed by an increase in the rms velocity measured.

Table 1. Operational parameters for the scanning LDV system.

<u>Parameter</u>	<u>Smooth wall</u>
Scan velocity	1.5 m/s (7.8 $U_\infty$ )
Scan frequency	28 scans/s
Scan range	2.3 cm (230 $y^+$ )
Time for one scan	17 msec (1.3 $T^+$ )
Time between scans	37 msec (2.9 $T^+$ )
Average data rate	40 points/scan
<u>Velocity uncertainty</u>	<u><math>\pm 3\%</math></u>

Modification to the scanning LDV system was implemented to allow two component velocity measurements. The second velocity component was in the scanning direction, which was the vertical component relative to the wall. Accurate measurements of this component requires that the scan velocity be known very accurately, because the scan velocity must be subtracted from the total measured velocity to yield the flow velocity. Given a scan velocity nominally 10x greater than the mean velocity, and an rms vertical velocity fluctuation of nominally 5% of the mean, the scan velocity is about 200x greater than the measured velocity. Even an accuracy of  $\pm 10\%$  for the measured vertical component requires an accuracy of 0.05% for the scan velocity. The stepping motor system used to drive the scanning mirror and/or the vibration of the scanning mirror did not allow for this extreme accuracy for the scanning velocity. Because of this limitation no further

efforts were made in this project to obtain two-component velocity measurements with the scanning LDV system.

### 3.2. Evolution of Large Scale Structures

The goal of this phase of the project was to study the long term evolution and characteristics of the large scale structures. The idea was to track the development of these structures, right from their inception to their dissipation. In order to do this, much effort was made to determine characteristics by which the larger scale structures might be reliably identified.

Most researchers have described large scale structures as bulges, vortices or large scale coherent motions in the outer region of the boundary layer. Very few have actually tried to define a large scale structure, or more importantly define their identifying features. Among the few definitions attempted are those by Falco (1977) and Smith (1978). Falco, using a smoke technique, defined large scale motions by the existence of smoke free regions or concentration gradients which extend deep into the layer on both the upstream and downstream side of the bulges. Smith, defined large scale motion as an agglomeration of smaller scale vortical structures of varying sizes, strengths, orientations and coherency with an overall spanwise rotation. These definitions were used as a guide to look for large scale structures in the present study.

To make full use of the above guidelines, a stationary side view of a vertical hydrogen bubble wire was studied. Combined dye and hydrogen bubble visualization was done with a wall dye slot showing the near wall structures in order to find any relationship between the outer and inner structures. To study how the structures evolved with time, they were followed over a distance of 70 cm ( $\sim 10\delta$ ) using a convecting camera. As the hydrogen bubbles tend to dissipate when they move downstream, two wires separated by about  $5\delta$  were used to form fresh bubbles. Combined dye and hydrogen bubble visualization was also done in the convected frame of reference. But, with the intermittent nature of the boundary layer and the wide variations in size and shape of the structures, it was very difficult to isolate a large scale structure and follow its development.

In an effort to better define large scale structures, other camera views and hydrogen bubble wire orientations were investigated. Side view of a horizontal bubble wire placed at various heights from the wall with a vertical laser sheet clearly showed the presence of transverse vortices throughout the boundary layer. When a multi-wire probe with three horizontal wires was used to get simultaneous information across the boundary layer, it clearly showed an outward movement of the transverse vortex motions. As

transverse vortex motions were found to be the dominant structure in the outer part of the boundary layer, their characteristic features were investigated.

The convecting camera was used to follow the transverse vortex motions for a distance of about  $10\delta$ . These vortices were very energetic initially, becoming bigger and slower as they move outwards and downstream, still retaining their identity. The transverse vortices appearing on the edge of the boundary layer combined to give rise to an overall tumbling motion, while entraining irrotational fluid as they moved downstream. The characteristic features of the transverse vortices were found by analyzing the flow visualization recordings using a high speed (200 frames/s) video system. Their streamwise extent was in the range  $0.15 < x/\delta < 0.3$  and they occurred at a normalized frequency of  $f\delta/U_0 = 0.84$ . Thus, the frequency of occurrence of the transverse vortices was much higher than the burst frequency ( $f\delta/U_0 = 0.22$ ) reported in Kohli and Bogard (1992). The transverse vortices had a spanwise extent in the range  $0.3 < z/\delta < 0.45$  at the edge of the boundary layer, which was obtained by using a horizontal laser sheet in conjunction with a horizontal wire. The convection velocities of transverse vortices depended on their distance from the wall, varying from  $0.9U_0$  to  $1.0U_0$ .

In the process of studying large scale structures, it has become clear that transverse vortex motions are an important part of the boundary layer dynamics. These transverse vortex motions will have to be investigated further in order to find out what makes a large-scale structure and how it evolves with time.

### 3.3. Mapping of Turbulent Structures: Smooth Wall

This task was a continuation of the burst mapping started in our previous ONR contract. In the previous work, measurements were made in a spanwise plane at a single streamwise location, and the streamwise spatial structure was deduced assuming a convected structure in accordance to the Taylor hypothesis of "frozen turbulence." In the present program we made a series of measurements upstream and downstream of the detector probe so that the actual streamwise spatial structure could be determined. These results were used to verify the previous use of the Taylor hypothesis to deduce spatial structure, and to determine the convection velocities of turbulent structures at various heights from the wall. The decay of turbulent structures at extended distances from the detector probe was also determined.

Further measurements were conducted in this task with the detector probe positioned at  $y^+ = 60$ , twice the height of  $y^+ = 30$  used in the original mapping work started in our previous ONR contract. These measurements were

conducted to establish the sensitivity of the conditionally sampled turbulent structures to the height of the detector probe. Recall that a major goal of this program was to determine how rough walls affect turbulent structures as deduced from conditional sampling. Since viscous scaling is not appropriate for flow over rough walls, establishing a detector height equivalent to  $y^+ = 30$  was problematic. Consequently we needed to know the sensitivity to detector height in order to distinguish changes in structure due to roughness from those due to differences in equivalent detector height.

The mapping plane consisted of 72 measurement locations covering the range of  $-250 \leq x^+ \leq 200$  and  $10 \leq y^+ \leq 100$ . The burst detection point was at  $(x^+, y^+, z^+) = (0, 30, 0)$ . A 2-component LDV system, a single component fiber-optic LDV system, and an X-type hot-film probe were used to make simultaneous velocity measurements. When mapping was done upstream of the detector, the X-type hot-film probe was used as the detector and the two LDV systems were combined to give three-component LDV measurements at the mapping position. When mapping was done downstream of the detector, the 3-component LDV was used as the detector and the X-type hot-film probe was used at the mapping position. The LDV data rates were greater than 300 samples/sec, which corresponds to an average time between measurements of  $\Delta t^+ = 0.3$  for the flow conditions, so that essentially continuous time records were obtained from the LDV systems.

Bursts were detected at the detection point using the quadrant technique with a threshold of  $H = 1.0$ . The data from the mapping probe were conditionally sampled at each measurement location using the occurrence of bursts as the condition. The conditionally sampled data were phase aligned with the maximum magnitude second quadrant  $uv$  of the detected bursts. This corresponds with the middle of the strongest ejection within the burst. The resulting ensemble average of the fluctuating  $u$  velocity associated with a burst is shown in Figure 2(b). For comparison, the ensemble average of the fluctuating  $u$  velocity of a burst deduced using a convected view of measurements at a single streamwise positioned (used in our previous study) is shown in Figure 2(a). Similar structural features were obtained from the spatial measurements and the convected frame of reference. In both cases the burst was found to have an inclined shear layer along the trailing edge and a somewhat rounded leading edge. The slightly longer extent of the burst structure with the convected view calls to question the convection velocity used to deduce this result. Techniques used to determine the convection velocity are discussed later in this section.

Further confirmation of the accuracy of the convected view is shown in Figure 3(a) and (b) where the velocity vectors for the fluctuating  $u$  and  $v$  velocities components are given. Again, the structural features indicated by these velocity vectors were similar for the spatial measurements and the convected frame of reference. Note that the velocity vectors show a strong

uplifting centered at the burst event, as expected, but do not show any downward flow before or after the burst event. This result is of interest since it indicates no evidence of a sweep upstream or downstream of the burst.

The previous mapping experiments were done with the event detection at  $y^+ = 30$ . Streamwise and spanwise mappings were also done with the detection at  $y^+ = 60$  to study the effect of detection height on the characteristics of the burst and sweep structures, including the convection velocities. For these mapping experiments the range covered in the streamwise plane was  $10 \leq y^+ \leq 120$  and  $-250 \leq x^+ \leq 200$ , and for the spanwise plane it was  $10 \leq y^+ \leq 120$  and  $-10 \leq z^+ \leq 120$ .

Since the development of these events changes with the distance from the wall, different classes of events are detected at different heights. For example, bursts detected at  $y^+ = 30$  are at an earlier stage of development than those detected at  $y^+ = 60$ . Thus, the conditionally sampled maps will show how the structures and the associated flow field differ for different classes of events.

The following comparisons are made for bursts detected at  $y^+ = 30$  and  $y^+ = 60$  using quadrant detection with a threshold of  $H = 1.0$ . Ensemble averages of the conditionally sampled  $u$  velocity in the streamwise plane for detection at  $y^+ = 30$  and  $y^+ = 60$  are presented in Figures 2(b) and 4, respectively. Not surprisingly, the maximum conditionally sampled negative velocity in each case occurred at the detection point. The overall shape of the burst is very similar for the two detection heights. While the streamwise extents of the bursts are very similar, the vertical extent for the bursts detected at  $y^+ = 60$  is significantly higher. Also, the bursts detected at  $y^+ = 30$  have a somewhat greater negative velocity at the center of the events.

Contours of the spanwise cross-section of the  $u$ ,  $v$ , and  $uv$  signals for bursts detected at  $y^+ = 30$  and  $y^+ = 60$  are shown in Figures 5, 6 and 7. These contours show similar structure for detection at both heights, and in each case the maximum in the  $u,v$ , and  $uv$  signals was centered at the detection height. The structure detected at  $y^+ = 60$  was 20% to 30% larger in height and width, but certainly not double the size even though the detection height was doubled. This result is important in that it shows that the size of the conditionally sampled structure does not scale with the height from the wall at which it is detected. Velocity vectors in the spanwise plane, based on the  $v$  and  $w$  velocity components, are shown in Figure 8(a) and (b). Again the structures are similar for detection at the two heights with the structure detected at  $y^+ = 60$  being slightly larger.

Conditionally sampled measurements with the mapping probe covering the streamwise plane far upstream and downstream of the detection point allows the tracking of the burst structure as it approaches the detection point, and following detection. An example of this streamwise tracking of the quadrant detected burst structure, with the detecting probe at  $y^+ = 30$ , is shown

in Figure 9. In this case contour levels of the conditionally sampled uv signal are presented; similar contour plots of the u and v signals were also analyzed. As expected, the uv signal increases in strength as it approaches the detection probe, and decreases in strength after passing through the detection probe. Recognizable u, v, and uv signals were found over the full range measured,  $250 \leq x^+ \leq 200$ . The contours of the u signal showed a slight increase in height,  $\Delta y^+ = 10$ , as the structure moved from  $x^+ = -50$  to  $x^+ = 40$ , which is consistent with the magnitude of the v signal during the detection. However, the v and uv contours showed no change in height. This suggests that the structure responsible for providing the lifting motion, and thereby uv Reynolds stress, is convecting streamwise at a relatively constant height from the wall.

Streamwise tracking of the burst structure was also done with the detecting probe at  $y^+ = 60$ . Results from analysis of the u, v, and uv contours were very similar to the results described above for detection at  $y^+ = 30$ , except the structures in this case were centered at  $y^+ = 60$ .

Conditional sampling along the streamwise plane was also done using 4th quadrant detection to identify sweeps, and using VITA with positive slope detection to identify shear layer events. The sweep structure consisted of a high speed region which was slightly larger than the low speed region for a burst. The shear layer structure, shown in Figure 10, consisted of a low speed region followed immediately by a high speed region. The shear layer between the high and low speed regions is at a steep angle near the wall, but becoming a much shallower angle further from the wall.

Tracking the burst, sweep, and shear layer structures in the streamwise plane allowed us to determine the convection velocities for each of these structures. Details of this analysis are given in Gan and Bogard (1991). Convection velocities determined with the detector probe located at  $y^+ = 20$ ,  $y^+ = 30$ , and  $y^+ = 60$ , are presented in Figure 11. The convection velocity of the burst detected at  $y^+ = 20$  and 30 are nominally the same, and that at  $y^+ = 60$  is higher. The difference in the convection velocities with height may be attributed to the different classes of bursts detected at those heights. At the lower heights, the bursts are at an early stage of development, and are ejecting away from the wall more strongly than at the higher height. Low velocity fluid from the wall region is thus more strongly pulled up, contributing to a lower convection velocity. Sweeps detected at  $y^+ = 20$  have a convection velocity similar to that at  $y^+ = 60$ , but the sweeps detected at  $y^+ = 30$  were unusually slow. The convection velocity of the shear layer event falls between that of the burst and sweep at each of the heights.

The nominal velocity of the sweep was about 20% faster than the burst. This higher velocity was maintained over the full distance that the structures were tracked, i.e.  $\Delta x^+ = 450$ . Consequently, during the time that it takes for the burst to travel this distance, the sweep travels a distance  $\Delta x^+ \approx 80$  further than

the burst. Recall that the scales of the burst and sweep are both nominally  $t^+ = 80$ . These results are significant when considering the possibility that the sweep and burst are part of the same overall structure. If the structure were to start with the sweep upstream of the burst, the sweep will move completely around the burst by the end of the tracking distance.

As in previous studies, our results showed that the shear layer structure is inclined in the direction of flow, and that it has a convection velocity that is nominally equal to the local mean. The conditionally sampled velocity contours for the shear layer structure show that it consists of a high speed structure upstream of a low speed structure. One might be inclined to associate these structures with a sweep and burst, respectively. However, as noted above, the sweep convection velocity is such that it would completely overtake the burst over the tracking distance. This would obliterate the fundamental character of the shear layer structure and it would not be detectable with the VITA technique. Since the shear layer structure was clearly detectable over the full tracking distance, it does not appear to be directly associated with the sweep and burst structures identified with the quadrant technique.

Further understanding of characteristics of bursts, sweeps, and shear layers was obtained by analyzing the time sequence of the spanwise cross-section of the velocity vectors. The time sequence of velocity vectors for a quadrant detected burst is shown in Figure 12. The velocity vectors at  $t^+ = 0$  are the same as that presented previously in Figure 8(a). Evident from this time sequence is that the strong upflow begins to occur at least  $t^+ = 5$  before the detection time, but has completely disappeared by  $t^+ = 5$  following the detection. Since the detection occurs at the strongest (largest -uv signal) part of the burst, this indicates that the strongest part of the burst occurs near the end of a burst. Furthermore, note that the spanwise inflow near the wall and towards the center of the burst is evident at  $t^+ = -10$ , and well established by  $t^+ = -5$ . A corresponding spanwise outflow at higher heights is not evident until  $t^+ = 0$  and later. At  $t^+ = 0$  the velocity vectors suggest a streamwise vortical motion, but there is a noticeable lack of downward motion so a complete rotation is not established. These observations suggests that the initiation of a burst is due to a near wall inflow which is not necessarily associated with a vortex motion.

The results for the burst described above were based on quadrant detection with phase alignment with the maximum negative uv peak during the burst. Phase alignment is critical in conditional sampling analysis, and details of the velocity field can be greatly diminished due to phase jitter. Because of this we investigated the effect of phase alignment with the leading and trailing edges of the burst. For this analysis the leading edge was defined as the point where the uv signal first passed the threshold of  $H = 1$ , and the trailing edge as the final point which fell below the threshold of  $H = 1$ . Cross-sections of the

velocity vectors for the leading edge of the burst, shown in Figure 13, indicate a strong uplifting at the leading edge ( $t^+ = 0$ ) and continuing after the leading edge. In contrast, Figure 14 shows that there is no significant lifting at the trailing edge, but significant lifting occurs  $t^+ = -5$  and  $-10$  before the trailing edge. Furthermore, alignment with the trailing edge shows a more significant spanwise outflow immediately before the trailing edge and at the trailing edge than was evident before. Both leading edge and trailing edge alignment show the strong spanwise inflow at the beginning of the burst, but neither show any more significant vertical motions than was evident in the original phase alignment with the maximum negative  $uv$  peak.

Spanwise cross-sections for a quadrant detected sweep are presented in Figure 15. The strong downflow at the detection time appears to occur towards the end of the event. Preceding the sweep at  $t^+ = -10$  and  $-5$ , there is a strong spanwise outflow which is evidently a precursor to the sweep event. Although the velocity vectors at  $t^+ = 0$  have a somewhat rotating pattern, there is not a strong lateral inflow and upflow which would unambiguously indicate a streamwise vortex.

Finally, velocity vector cross-sections for shear layer structures, detected using VITA with positive slope, a threshold of  $k = 1$ , and an averaging time of  $T_a^+ = 10$ , are presented in Figure 16. The shear layer structure is preceded with a relatively strong upflow and spanwise outflow. A strong outflow is evident at the detection time, and a downflow with outflow follows detection. Although the velocity vector characteristics at  $t^+ = -10$  are similar to those of a burst, the outflow at  $t^+ = -5$  is much greater than that observed for a burst. The inflow and near wall outflow at  $t^+ = 5$  are similar to that observed for a sweep.

### 3.4. Conditional Sampling Using Spatial Detection

A unique spatial detection technique was developed as part of this project which takes advantage of the two-dimensional velocity field information obtained from the scanning LDV system. The spatial detection technique is based on identifying spatially coherent velocity regions in the flow as opposed to point measurements as has been used in all previous studies using conditional sampling. There are distinct advantages to using the spatial detection technique since truly spatially coherent structures can be identified, and the size and position of the structures can be distinguished. Since bursts, sweeps, and shear layer can be associated with regions of low speed, high speed, and spatial velocity gradients, respectively, this method is well suited for detection of these events. As described in Section 3.1, the scanning LDV system has a range from  $y^+ = 10$  to the outer regions of the boundary layer which is also ideal for tracking the evolution of the burst, sweep, and shear

layer structures. However, at this time the scanning LDV system is capable of measurement of the streamwise  $u$  velocity component only; so vertical movement and regions of high Reynolds stress can not be identified. Details of the spatial detection technique are described in the thesis by Bolton (1990) and in Bolton and Bogard (1992). Conditional sampling studies of low speed events (bursts) are presented in Bolton and Bogard (1992), and both low speed and high speed (sweeps) events in Kohli and Bogard (1992) and in Appendix A. Conditional sampling studies of shear layer events is presented in Bolton (1990). This section briefly describes the spatial detection technique and then the conditional sampling analyses of the burst and sweep structures.

As the velocity measurements were randomly spaced within each scan, some processing of the data was required before the detection scheme could be applied. To obtain velocity values uniformly spaced across the scan range, raw velocity data were grouped together in  $\Delta y^+ = 10$  intervals. Multiple measurements within an interval were averaged, but when no data were measured within an interval, a linear interpolation was made if adjacent data were available. If adjacent data were not available a gap in the time record of the velocity field was indicated; the only gaps in the velocity record occurred intermittently very near the wall ( $y^+ < 25$ ). The time between scans was  $t^+ = 2.9$  allowing an essentially continuous time history of the velocity field. All further analyses was done on this uniformly spaced velocity data.

Use of low  $u$  velocities for detecting bursts is supported by the results of Bogard and Tiederman (1986) who showed that, for single point measurements, the  $u$ -level technique was comparable to the quadrant technique in effectively identifying bursts. For the spatial detection technique, a detection was indicated when the velocity fell below a set threshold over a "significant" region. An appropriate threshold for identifying significant low speed spatial structures was investigated (details given in Bolton and Bogard, 1992, and Bolton, 1990), and the frequency of spatial structures was found to be largely independent of threshold. The following results are based on a threshold of  $L = u/u_\tau$ .

Figure 17 illustrates how the spatial detection technique is used to detect low speed events. Discrete points where the velocity is below the threshold are indicated by  $\Delta$ , points above the threshold are indicated by the symbol  $O$ , and points where there are no data are indicated by dashes. An algorithm was written to recognize groups of discrete points with velocities lower than the threshold. A coherent event (group) was defined by using the following criteria:

1. A discrete detection must be located within 2 bins ( $\Delta y^+ = 20$ ) of another detection in the same scan.
2. A discrete detection must be located within an adjacent scan ( $T^+ \approx 3$ ) at the same bin height.

Discrete detections separated by more than  $\Delta y^+ = 20$  and  $T^+ = 3$  were classified as a new coherent grouping (see Figure 17). In this manner coherent groups of low (or high) speed events ranging in size and location were identified.

While the grouping of events was done, the size, top, bottom, start and end of each group was recorded. This allowed conditional sampling based on the size of the event and the minimum or maximum height of the event. As the bursts are known to move away from the wall, conditional sampling for the low speed events was based on their maximum height. Similarly, the conditional sampling of high speed events was based on their minimum height from the wall. Ensemble averaging was done on events with maximum or minimum heights within a certain  $y^+$  range, forming a "category". As each category was restricted to events at nominally the same height, categories at increasing heights showed the evolution of the event with distance from the wall. In all the conditional sampling analyses done in this study the events were phase aligned on their leading edge. An appropriate convection velocity was used from Gan and Bogard (1991) to convert the time sequence of the scanned data to a spatial x-y plane.

Figure 18 shows a sequence of ensemble averages of the low speed events which represent bursts at different heights from the wall. The low speed burst grows in size as it is detected at larger distances from the wall and finally detaches from the wall. The negative velocity levels, and the velocity gradients are significantly larger when the burst structure is near the wall. The velocity levels decay as the burst increases in size and moves away from the wall.

Figure 18 also shows the movement of a high speed structure associated with the burst event. Close to the wall, the high speed structure is present on top of the low speed structure. At higher heights the high speed fluid moves over and downstream of the low speed event. The high speed structure also increases in size and extends across the full range presented in the figure. The presence of a high speed structure along with the conditionally sampled low speed event is a characteristic of the burst event that has not been evident in previous studies which have used single point detection techniques. Single point detection on the same data does not show any high speed structure associated with the burst because it groups events of all sizes and different heights together. This is a clear example of how the newly developed spatial detection technique can give more insight into the interaction of coherent structures.

Similar analyses was done for the high speed events based on their minimum height from the wall. Results are not discussed here for sake of brevity and can be found in Appendix A.

### **3.5. Effects of Rough Surfaces and LEBU Devices on Turbulent Structure**

#### **3.5.1. Rough Surface Effects**

The goal of this task was to obtain a better understanding of the interaction of inner burst and sweep structures with the outer flow by suddenly perturbing the inner flow with a rough wall. We designed the rough surface to give an increase in shear stress by greater than a factor of two. By tracking the adjustment of the inner and outer structures to this sudden change in shear stress, and to the eventually fully developed rough wall flow, we expected to obtain a better understanding of the dynamics of burst and sweep development.

The rough wall comprised cylindrical elements placed in a square array (actually large LEGO blocks). The elements had a height of  $k = 4.5$  mm, and a diameter of  $d = 9$  mm. Spacing between elements was  $S = 16$  mm. In the self-sustaining region of the boundary layer where the fully developed flow measurements were taken, the dimensions of the roughness elements in wall units were  $k^+ = 65$ ,  $d^+ = 130$ , and  $S^+ = 230$ . This rough wall was in the fully rough regime (shown in Appendix A) and hence independent of viscous effects. This is a very important point when considering spatial and temporal scaling of the detected structures since commonly used inner scaling is no longer appropriate.

For the rough wall studies we needed to establish the accuracy of determining the wall shear stress using near wall measurements of the Reynolds shear stress. This was necessary because use of the mean velocity profile to establish wall shear is accurate only for fully developed rough wall flow, and not in the smooth-to-rough transition region. Measurements of the  $uv$  Reynolds stress were made in the near wall constant stress layer for a smooth wall and a fully developed rough wall. For these cases  $\tau_{wall}$  obtained from  $\bar{uv}_{max}$  was compared to  $\tau_{wall}$  obtained from the mean velocity profiles. Based on these comparisons we modified the LDV system to use a smaller pin hole for the photomultiplier tube which resulted in good accuracy for the  $\bar{uv}_{max}$  measurements. Subsequent determination of  $\tau_{wall}$  in the smooth-to-rough transition region was based on measurements of  $\bar{uv}_{max}$ .

Single point measurements were made of the Reynolds stress profiles over the smooth wall upstream of the rough wall, in the smooth-to-rough transition region, and in the fully developed fully rough region. As shown in Appendix A, the internal layer, which starts at the start of the roughness elements, grew until a fully developed rough wall flow was established at approximately 23 boundary layer thicknesses downstream ( $23\delta_{0,r}$ ). Measurements were made  $-1\delta_{0,r}$  upstream (smooth wall),  $2\delta_{0,r}$  downstream (transition region), and  $24\delta_{0,r}$  downstream (fully developed fully rough

region) of the step change to roughness, where  $\delta_{0,r}$  is the boundary layer thickness at the step change.

Figure 19 shows the  $\bar{uv}$  profiles for the three streamwise locations. Measurements over the rough surface were made at points corresponding to the open area within the roughness elements (the effect of the measurement position with respect to the roughness elements will be discussed later). Note that the origin for  $y$  used in this figure is the apparent origin for the rough wall which was approximately 2.2 mm below the tops of the roughness elements. As expected, based on our design of the rough surface, the Reynolds shear stress in the near wall region more than doubled almost immediately at  $x = 2\delta_{0,r}$  indicating a similar increase in wall shear stress. However,  $uv$  falls rapidly away from the wall, and by  $y/\delta = 0.3$  assumes values similar to the smooth wall values. This implies that the increase in Reynolds shear stress is confined to the internal layer which is developing in response to the rough surface (consistent with the results of Antonia and Luxton, 1971, although Antonia and Luxton indicated concern with the accuracy of their hot-wire measurements of  $uv$  near the wall).

For the fully developed rough flow at  $x = 24\delta_{0,r}$  the  $uv$  profile increased across the height of the boundary layer. Of particular interest was the sharp increase in  $uv$  very near the wall. This increase is actually a function of where  $uv$  is measured relative to the roughness elements. Figure 20 shows  $uv$  profiles for four different positions with respect to the roughness elements taken at  $x = 24\delta_{0,r}$ . For measurements taken at  $y \geq 3$  mm above the top of the roughness elements the  $uv$  values collapsed to similar profiles, but at  $y = 1$  mm there were significant differences. Immediately above the roughness element the  $uv$  level was greatly reduced which can be attributed to viscous damping. For all four positions there was a range of  $3 \text{ mm} \leq y \leq 7$  mm over which  $uv$  was relatively constant, and this was taken to be the constant stress layer.

The effect of the sudden smooth-to-rough transition on ejection and burst frequencies is shown dimensionally in Figure 21 (recall that a single burst event may contain one or more ejections). Similar to the results for  $uv$ , the ejection and burst frequencies changed only within the internal layer. However, surprisingly the ejection and burst frequencies did not change substantially. In fact, for the fully developed rough flow, both ejection and burst frequencies decreased. Obviously the increase in  $uv$  is not due to an increase in burst frequency, or in the number of ejections within a burst. Scaling of the burst or ejection frequencies with inner variables, as is typically done for smooth wall flows, would not be appropriate because the fully rough flow should be independent of viscosity. Therefore, it is not surprising that inner scaling does not collapse the data. Outer scaling, shown in Figure 22, does reasonably well in collapsing the data, but this may not be significant since only one flow condition was tested. One point of interest is that the

burst frequency for the fully developed rough wall flow has a 50% increase near the wall as distance from the wall increases. This is in contrast to the smooth wall which has essentially constant value across the boundary layer (note that the low burst frequency very near the wall for the smooth wall was measured at  $y^+ = 8$ ).

As discussed above, the large increase in uv over the rough wall was not due to increase burst or ejection frequencies. Quadrant analysis of the uv contributions showed negligible increase in the 4th quadrant contribution in the smooth-to-rough transition region, and a slight decrease in the 4th quadrant contribution in the fully developed rough wall flow region. These results show that the increase in the uv level over the rough wall is not due to increased contribution due to sweeps.

The ensemble averaged uv signal for quadrant burst detections over the smooth and rough walls are shown in Figure 23. For the smooth wall the detections were made at  $y^+ = 30$  ( $y/\delta = 0.07$ ) which was in the constant stress layer where uv is maximum. The equivalent heights for the smooth-to-rough transition region and the fully developed rough wall region were taken to be in the constant stress layers, also. For the smooth-to-rough transition region this corresponded to a detection height of  $y_t/\delta = 0.10$ , and for the fully developed rough region the detection height was  $y_t/\delta = 0.07$ , where  $y_t$  is measured from the top of the roughness elements. Immediately evident from Figure 23 is that the strength of the uv signal for the bursts over the rough wall was significantly greater than for the smooth wall, but the duration was nominally the same. These results indicate that the increased Reynolds shear stresses, which occur almost immediately with the start of the rough surface, are due to an increase in the strength of the bursts, and not to increased duration or frequency of bursts.

Further conditional sampling analysis of the effect of the rough wall on the burst structure was done using the spatial detection technique as described in section 3.4 for the smooth wall. As for the smooth wall, the spatial detection technique and conditional sampling analyses was used to construct ensemble averaged events at various height categories. Figure 24 shows typical results from the conditional sampling analyses of low speed events (bursts) over smooth and rough walls at two height categories. Results at other height categories have not been shown for sake of brevity. It is clear that the rough wall events are distinctly different than those found over the smooth wall. The burst over the rough wall is bigger and has lower velocity levels. Also, there is no indication of significant high speed fluid associated with the low speed event as there was for the smooth wall. Since the high speed fluid originates in the outer region of the flow, this suggests that a stimulus from the outer region is generating bursts over a smooth wall, but this stimulus does not occur over a rough wall.

Similar conditional sampling analysis was done using spatial detection of high speed events or sweeps (see details in Appendix A). Unlike the low speed events, the high speed events are not affected by the change in surface roughness, maintaining the same size and velocity levels. For both smooth and rough wall flows, the conditionally sampled high speed events showed a high speed structure only, with no associated low speed fluid event.

Simultaneous X-type hot-film anemometer and scanning LDV velocity measurements were also made in the fully developed fully rough region. The hot-film probe was used as an event detector while the scanner was used as a mapping probe. The mapping probe data was conditionally sampled using the occurrence of events at the detector as the condition. Unlike the spatial detection which detected events based on their  $u$  signal, the events detected here were based on their  $uv$  signal. The results are discussed in Section 3.5.3.

### 3.5.2. LEBU Device Effects

The goal of this task was to further gain a better understanding of the interactions of the burst and sweep structures with the outer flow by isolating the near wall region from the outer flow. The LEBU device comprised two stainless steel shimstock elements stretched across the entire width of the water channel, and were held at their ends by contoured brass supports. The supports were placed flush with the sides of the channel, and were used to apply tension to the LEBU elements, which had a thickness of  $t = 0.0023\delta_{0,l}$  and chord length of  $c = 0.6\delta_{0,l}$ . The elements were placed in tandem with a spacing of  $s = 4.7\delta_{0,l}$ , and were at a height of  $h = 0.3\delta_{0,l}$  above the wall, where  $\delta_{0,l}$  is the boundary layer thickness at the leading edge of the upstream element. The velocity measurements were taken at a location  $x = 15\delta_{0,l}$  downstream of the leading edge. These LEBU parameters were determined by Coughran (1988) to yield the most drag reduction.

Coughran measured the drag reduction by doing a momentum balance. In this study, a Clauser fit to Spalding's law of the wall was used to estimate the shear velocity, and hence the wall shear stress. The measurement showed between 15% and 20% wall shear stress reduction, close to that obtained by Coughran. Since the aim of this experiment was to use the LEBU device to perturb the flow field and to isolate the inner structures from the outer rather than to achieve maximum drag reduction, no attempt was made to further optimize the drag reduction capability of the LEBU device.

Conditional sampling analysis was done, similar to that for the rough wall using simultaneous hot-film anemometer and scanning LDV measurements. The results are discussed in the following section.

### 3.5.3. Comparison of the Effects of the LEBU Device and Rough Surfaces on Turbulent Structure

Simultaneous X-type hot-film anemometer and scanning LDV velocity measurements were made in a fully rough wall boundary layer, as well as in a smooth wall boundary layer with and without the LEBU device. Simultaneous hot-film and standard two component LDV measurements were also made to determine the convection velocities of the structures for each case. These rough wall velocity measurements were made in the fully developed region at  $x = 29\delta_{0,r}$  instead of at  $x = 25\delta_{0,r}$  previously. This new location was chosen so that the boundary layer thickness was the same as that of the corresponding smooth wall measurements. The wall shear stress increased by 2.5 times over the smooth wall.

The hot-film probe was used as an event detector while the scanner was used to map the flow field just upstream of the detector at a distance of  $\Delta x^+ = 20$  to 30. The detector was located at  $y^+ = 30$  for the smooth wall cases, and at  $y_t = 5$  mm above the tops of the roughness elements. The height of  $y_t = 5$  mm corresponds to the middle of the constant stress layer found for the rough wall. The quadrant method was used to detect bursts and sweeps. The VITA technique with a positive slope criterion was used to detect shear layer events. For a smooth wall boundary layer the VITA detection parameters of averaging time,  $T_a^+ = 10$ , and threshold,  $k = 1$ , are well established. Since inner scaling is inappropriate for rough walls, the averaging time of  $T_a^+ = 10$  is not valid. In order to establish an equivalent averaging time, a new scaling parameter needed to be determined first. As mentioned earlier, outer variables may not be appropriate as well. Since the focus here is on the comparison of the nearwall structures, a length scale obtained from the structures themselves would be appropriate. Such a scale will allow comparisons of the structures with each other, but will not be a universal scaling parameter.

Using the length of the burst as a length scale will allow comparisons of the sweep and shear layer events relative to the burst. The length of the burst was obtained from the time duration of the quadrant detected burst and its convection velocity. Figure 25 shows the ensemble averaged conditional samples of the smooth and rough wall burst, with the time being scaled by the burst duration. Normalizing with the respective burst durations forces the scale of the burst to be the same only at the threshold level. However, it can be seen that the conditional samples are similar for the entire burst. The ratio of the smooth wall burst duration to the rough wall burst duration was used as a scaling factor in determining the appropriate averaging time for the rough wall VITA detection. Figure 26 shows the ensemble averaged conditional samples for both smooth and rough wall shear layer events. The

velocity gradient for the rough wall shear layer is not as steep as that of the smooth wall event.

The convection velocities of the burst, sweep and shear layer in each of the boundary layer cases are shown in Figure 27. The convection velocities are relative to that of the smooth wall burst. For all three cases, the convection velocities of the sweep are 20% to 40% faster than those of the burst. Also, the convection velocities of the shear layer are between those of the burst and sweep for all cases, and are not significantly different between each case. Overall, the convection velocities for each structure are nominally the same for each case, with those for the rough wall case being slightly slower.

The scanning LDV velocity measurements were conditionally sampled using the occurrence of events at the detector as the condition. Figures 28 through 30 show the conditionally sampled fluctuating  $u$  velocity contours of the burst, sweep and shear layer for each of the three boundary layer cases. The streamwise  $x$  coordinates were obtained from the respective event convection velocities and time duration, and normalized by the length scale of the burst. The wall-normal  $y$  coordinates were similarly normalized, while the contour levels were normalized by the convection velocity of the burst.

As shown in Figure 28 the streamwise size of the bursts are nominally the same. This is expected since the scaling forces the bursts to be so. However, the overall shape of the structures is unforced, and it can be seen that the bursts for the smooth wall and LEBU-modified smooth wall are similar with the latter being slightly more elongated. The strengths of the bursts are also similar. The burst for the rough wall case, however, has a much greater wall-normal extent, and is not elongated. The sweeps, as shown in Figure 29, display the same trends. The sweeps for the smooth wall and LEBU-modified smooth wall are similar in both shape and size, although the LEBU sweep is slightly more elongated. The rough wall sweep is much larger. The strength of the sweeps of the smooth wall and LEBU-modified smooth wall is weaker as compared to their respective bursts. In contrast, the rough wall sweep is stronger than the burst.

The smooth wall and LEBU-modified smooth wall shear layers, as shown in Figure 30, are also similar in both shape and size. In the smooth wall case, the low speed event is stronger than the quadrant burst, while the high speed event is slightly weaker than the quadrant sweep. The strength of both the low speed and high speed events for the LEBU case is weaker compared to the quadrant burst and sweep. It can be seen that the overall size of the rough wall shear layer event is much larger than that of the smooth wall case. Of interest is the increase in strength of the high speed event relative to the low speed event. Typically, for the smooth wall the low speed event is stronger than the high speed one. For the rough wall, the high speed event is actually

slightly stronger. The increased strength of the high speed event is consistent with that found for the quadrant sweep over the rough wall.

The LEBU device acts to suppress the interaction between inner and outer regions. As mentioned earlier, the spatial detection results suggest that a stimulus from the outer region generates the bursts over a smooth wall. This is supported by the relatively steeper velocity gradient on the top of the quadrant burst towards the trailing edge in the results presented here (Figure 28). This steep velocity gradient indicates high speed fluid impinging on the burst. The slightly more elongated structures found for the LEBU case may be attributed to the suppression of this interaction. In the limit, if no ejections occurred, what is left will be the long streaks.

Over a rough wall, the spatial detection results suggest that there is no stimulus from the outer region. As shown in Figure 28, the lack of a relatively steep velocity gradient on the top of the quadrant burst towards the trailing edge tends to support this. This suggests that the roughness elements are stimulating the bursts. Recall from Figure 26 that the velocity gradient of the rough wall shear layer event was not as steep as that of the smooth wall event. This also supports the spatial detection results.

Although there does not appear to be a stimulus from the outer region, the quadrant sweep as well as the high speed event of the shear layer was found to be stronger than the burst. This is in contrast to the the smooth wall where the sweep and high speed event of the shear layer were weaker than the burst.

The shear layer events were detected using VITA with a positive slope criterion. For the smooth wall, positive slope events dominate negative slope events so that even without the slope criterion, the characteristic 'S' shape of the ensemble averaged shear layer is produced. Figure 31 shows the ensemble averaged shear layer events for smooth and rough walls using VITA with and without a slope criterion. As shown in Figure 31(a), for the smooth wall the strength of the event is only slightly weakened by the inclusion of the negative slope events. For the rough wall, however, it was found that the negative slope events occurred almost as frequently as the positive slope events, and consequently the strength is greatly reduced, as shown in Figure 31(b).

#### 4. Conclusions

In this research program we were able to develop a scanning LDV system which was proven to provide continuous time records of instantaneous velocity profiles in a turbulent boundary layer. This scanning LDV system

was used in conjunction with a unique technique for identifying true spatially coherent structures to show the spatial evolution of low speed bursts, high speed sweeps, and shear layer events. Three-dimensional mapping of these structures using conditional sampling techniques yielded details of the full three-component velocity field associated with these coherent structures. Contrary to general assumptions, results from these studies suggest that these structures occur relatively independently of each other.

Our studies of the effect of rough walls on turbulent structure showed very distinct differences in the character of bursts, sweeps, and shear layers over rough walls as compared to smooth walls. Using a rough wall designed to more than double the near wall turbulent shear stress, we found an almost immediate increase in the near wall burst strength, but no change in the burst or ejection frequency, or the burst duration. As the inner layer generated by the rough surface grew to a fully developed rough wall flow, the near wall burst characteristics remained essentially the same. Contrasting the burst structure over a smooth wall to that over a rough wall, there was a definite large scale high speed structure above the burst on the smooth wall, but not for the burst on the rough wall. This suggests that the outer flow has a greater role in stimulating bursts for smooth walls than for rough walls. Most striking, however, was the significantly stronger, and larger scale of the sweep structure over the rough wall compared to the smooth wall. These results suggest that, although the bursts on the rough surface are less dependent on stimulus from the outer flow, the stronger bursts from the rough surface cause a greater interchange of flow between the inner and outer parts of the boundary layer.

## References

Antonia, R.A. and Luxton, R.E. 1971 The response of a turbulent boundary layer to a step change in surface roughness, Part 1. Smooth to Rough. *J. Fluid Mech.* 48 (4), pp. 721-761.

Bolton, B.L. 1990 Detection of coherent structures in a turbulent boundary layer using a scanning LDV system. *M.S. Thesis*, The University of Texas at Austin.

Bolton, B.L. and Bogard, D.G. 1992 Detection of coherent structures in a turbulent boundary layer using a scanning LDV system. *Exp. Thermal and Fluid Science* 5, pp. 274-280.

Bogard, D.G. and Tiederman, W.G. 1986 Burst detection with single-point velocity measurements. *J. Fluid Mech.* 162, 389.

Coughran, M.T. 1988 Interdependence of large and small scale structures in a turbulent boundary layer. *PhD dissertation*, The University of Texas at Austin.

Falco, R.E. 1977 Coherent motions in the outer region of turbulent boundary layers. *Phys. Fluids*. 20 (10), pp. 124 - 132.

Gan, C.L. 1989 The burst structure and its associated flow field in a turbulent boundary layer. *M.S. Thesis*, The University of Texas at Austin.

Gan, C.L. and Bogard, D.G. 1991 Study of the convection velocities of the burst and sweep structures in a turbulent boundary layer. *Eighth Symposium on Turbulent Shear Flows*, Munich, Germany.

Kohli, A.K. 1992 Detection of coherent structures in smooth and rough wall turbulent boundary layer flows using a scanning LDV system. *M.S. Thesis*, University of Texas at Austin.

Kohli, A.K. and Bogard, D.G. 1992 Coherent structures in smooth and rough wall turbulent boundary layer flows. *Thirteenth Symposium on Turbulence*, Missouri-Rolla.

Purtell, L.P., Klebanoff, P.S. and Buckley, F.T. 1981 Turbulent boundary layer at low Reynolds number. *Phys. Fluids* 24 (5), 802.

Smith, C.R. 1978 Visualization of turbulent boundary layer structure using a moving hydrogen bubble wire probe. *Lehigh Workshop on Coherent Structure in Turbulent Boundary Layers*, ed. C.R. Smith, D.E. Abbot, pp. 48 - 97.

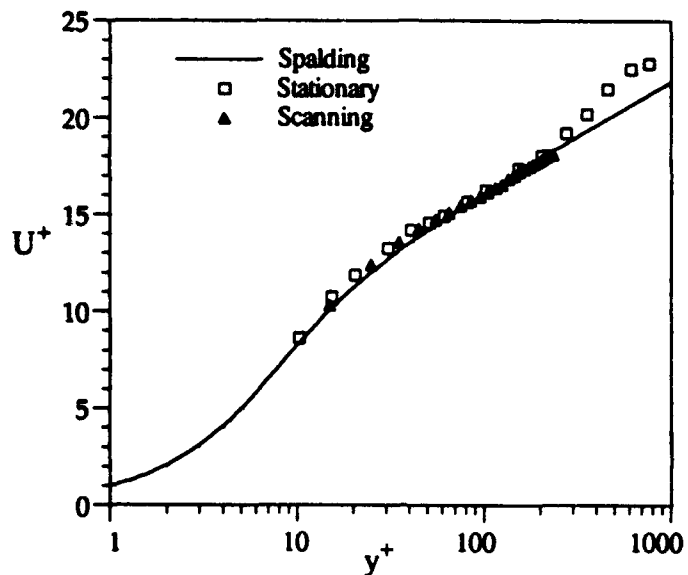


Figure 1(a) Scanning mean velocity profile compared with profile from stationary measurements and Spalding's law.

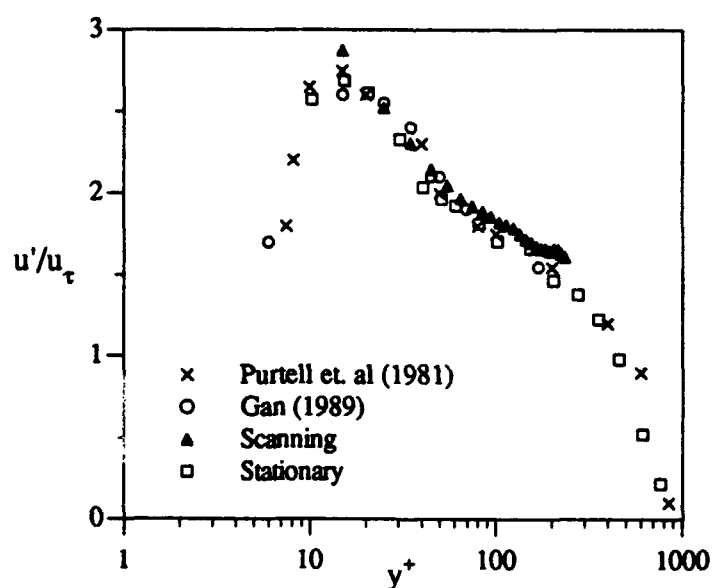


Figure 1(b) Scanning rms profile compared with rms profiles from stationary measurements, Gan (1989) and Purtell et. al (1981).

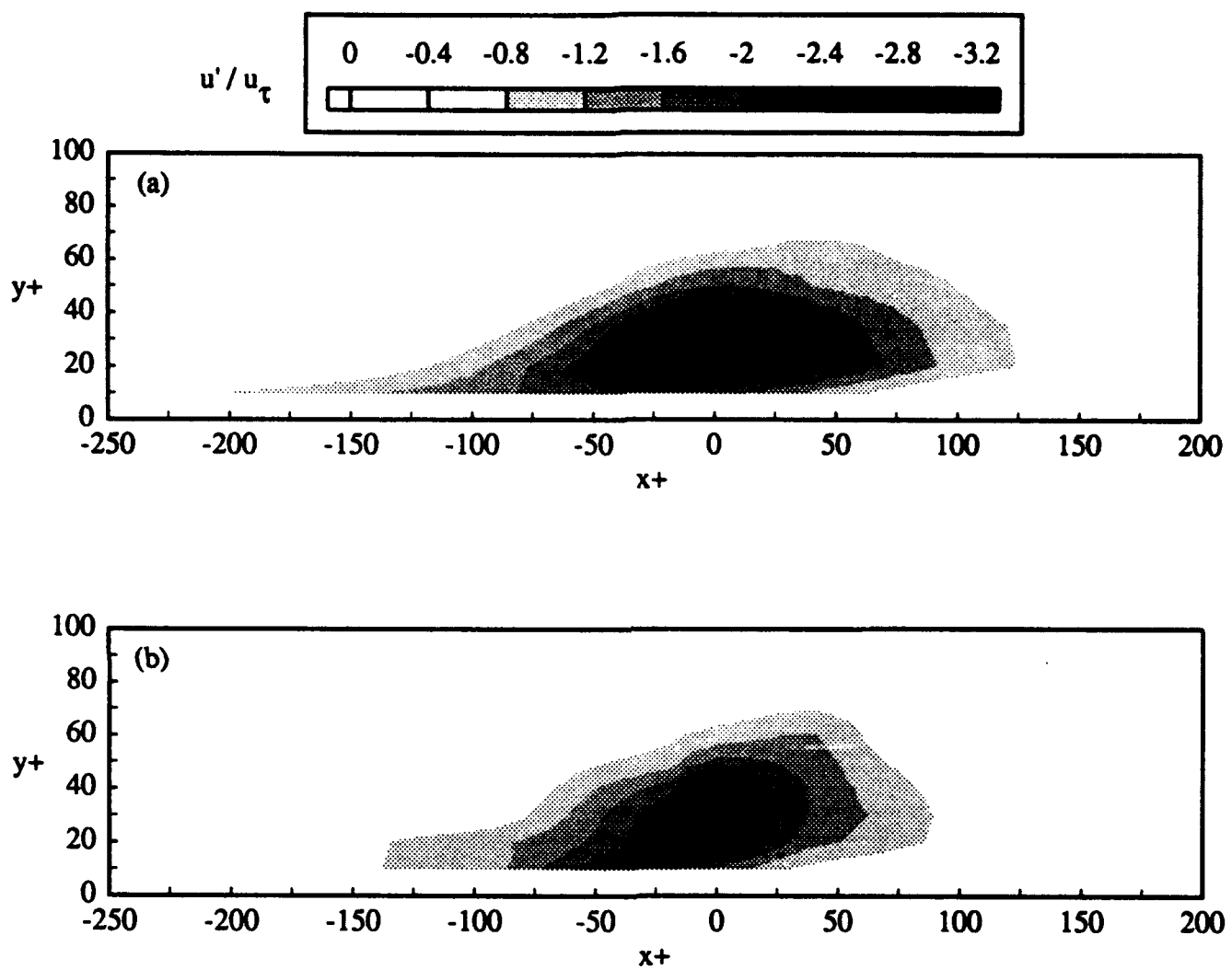
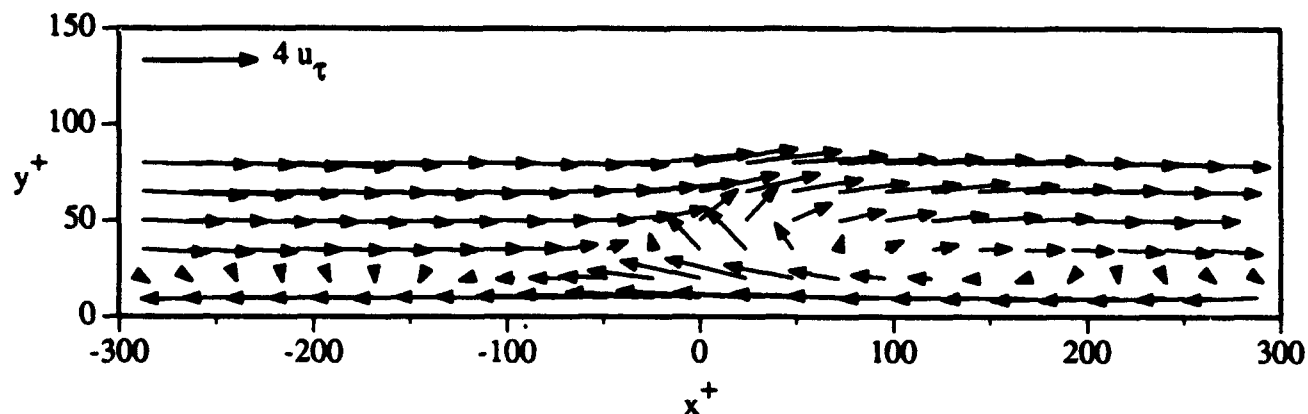
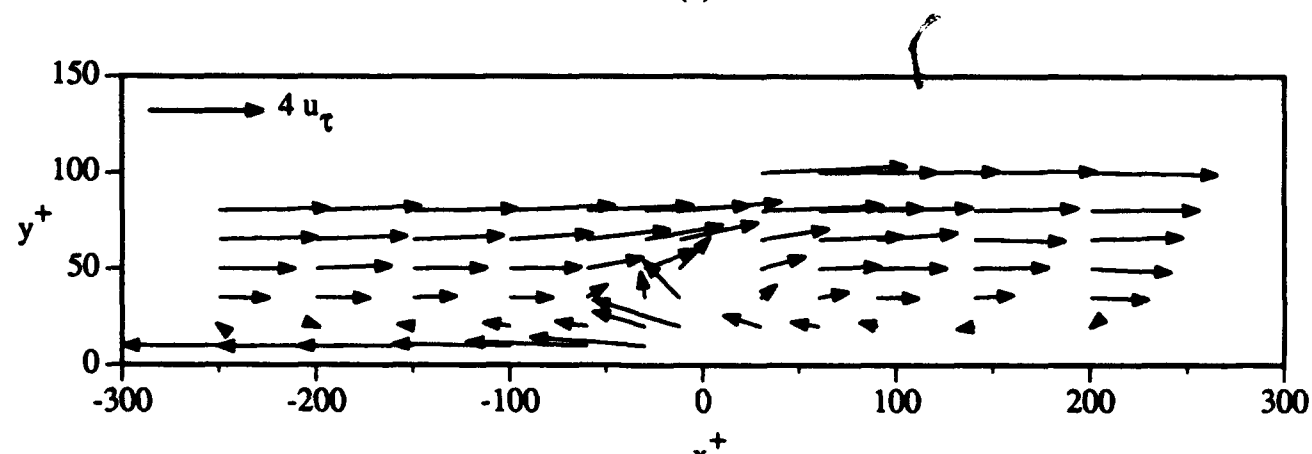


Figure 2 Quadrant burst detected at  $y_d^+ = 30$ ,  $u^+$  velocity defect contour levels. (a)  $x$  based on time history measurements and a convection velocity, (b) direct spatial measurement.



(a)



(b)

Figure 3. Quadrant burst detected at  $y_d^+ = 30$ ,  $u-v$  fluctuating velocities relative to burst convection velocity. (a) Based on time history measurements and a convection velocity, (b) direct spatial measurement.

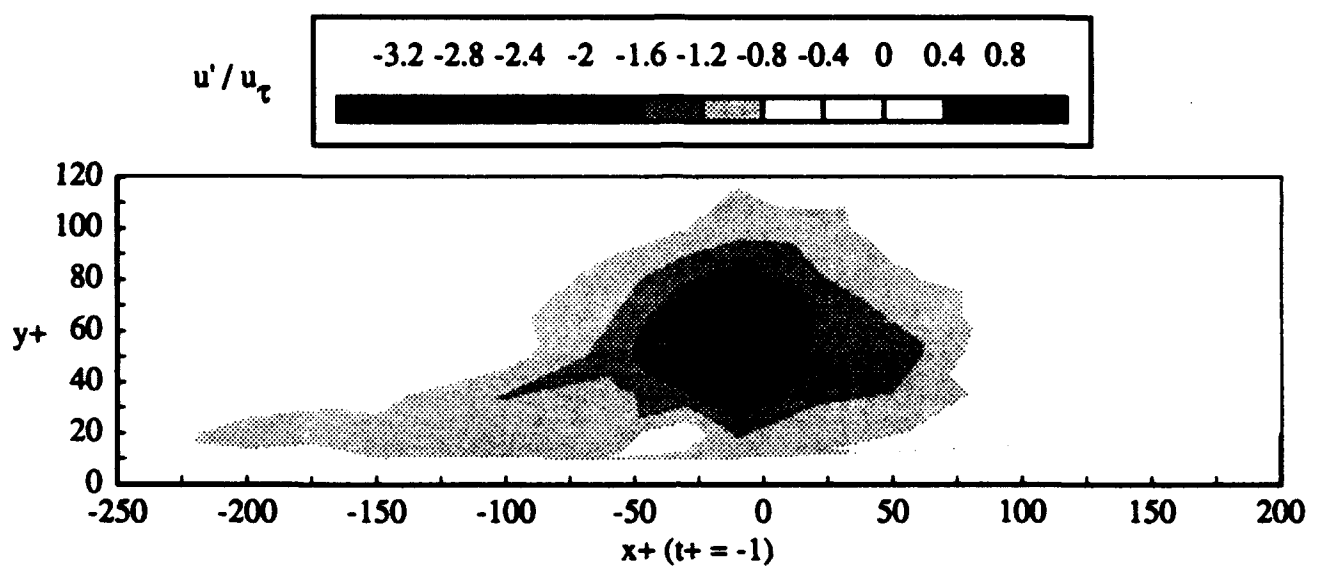


**Figure 4** Quadrant burst detected at  $y_d^+ = 60$ , direct spatial measurement of  $u^+$  velocity defect contour levels.

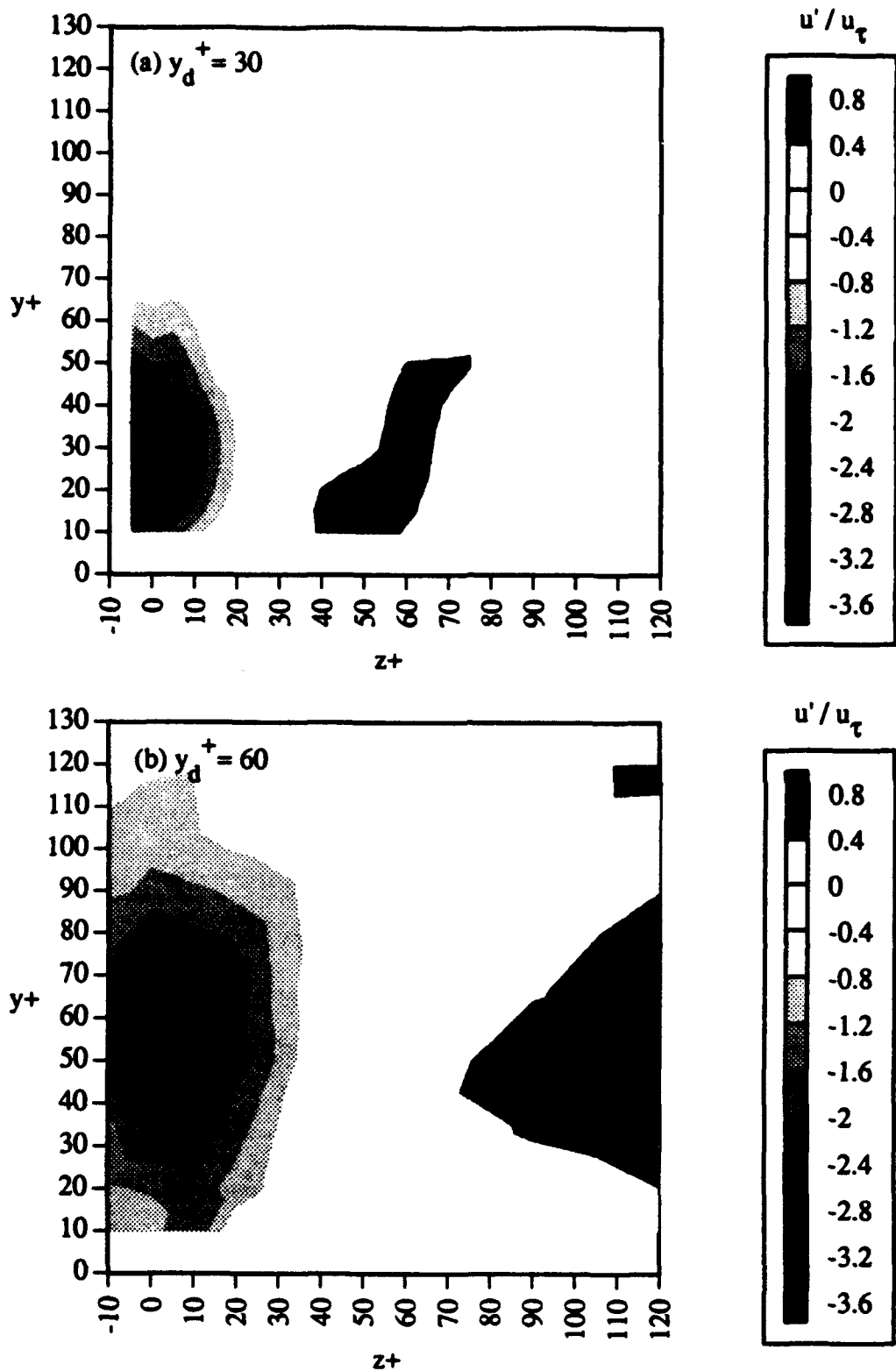


Figure 5 Spanwise cross-sections of quadrant bursts detected at: (a)  $y_d^+ = 30$  and (b)  $y_d^+ = 60$ .  $u^+$  contour levels.

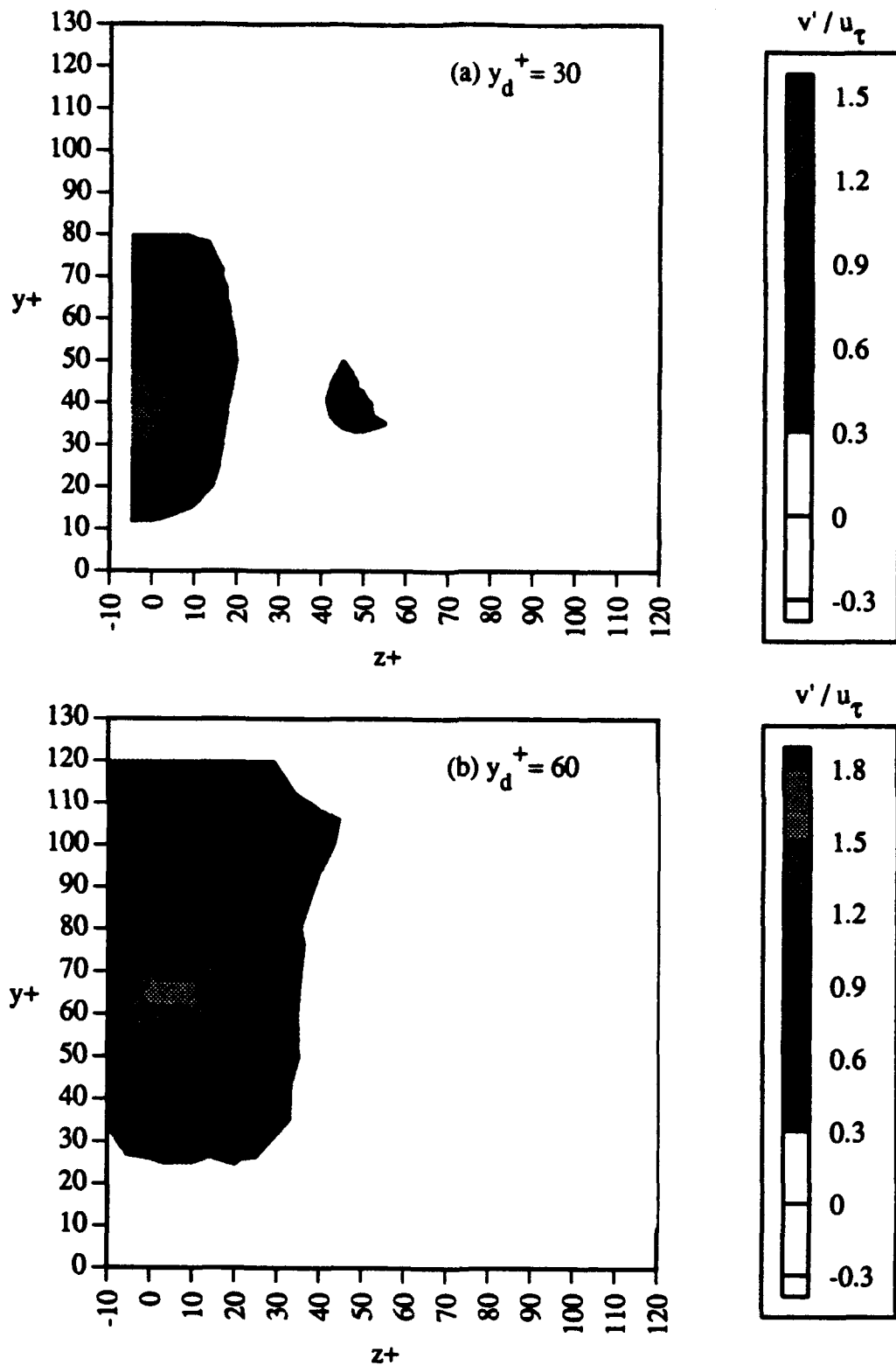


Figure 6 Spanwise cross-sections of quadrant bursts detected at: (a)  $y_d^+ = 30$  and (b)  $y_d^+ = 60$ .  $v^+$  contour levels.

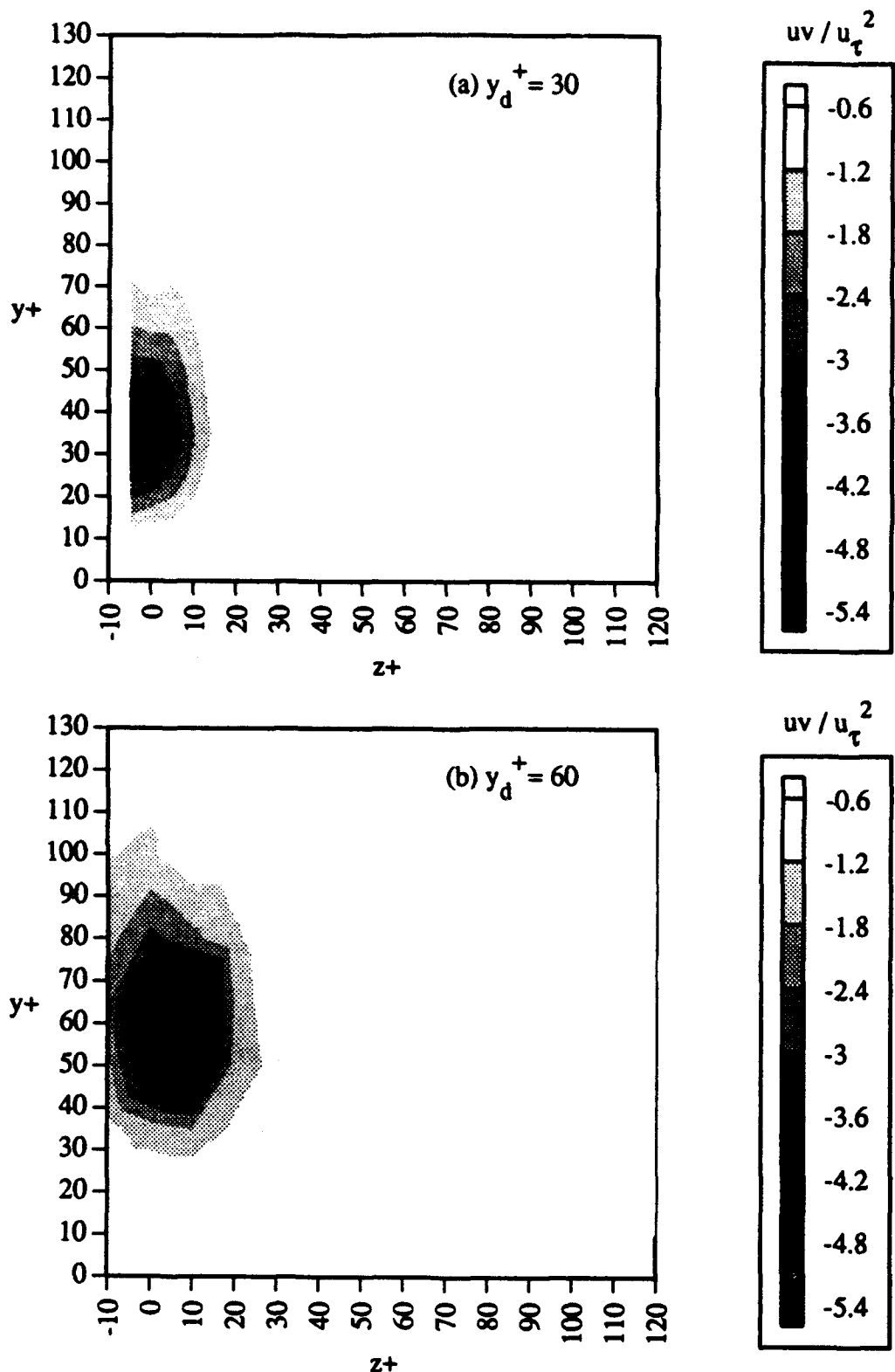


Figure 7 Spanwise cross-sections of quadrant bursts detected at: (a)  $y_d^+ = 30$  and (b)  $y_d^+ = 60$ .  $uv^+$  contour levels.

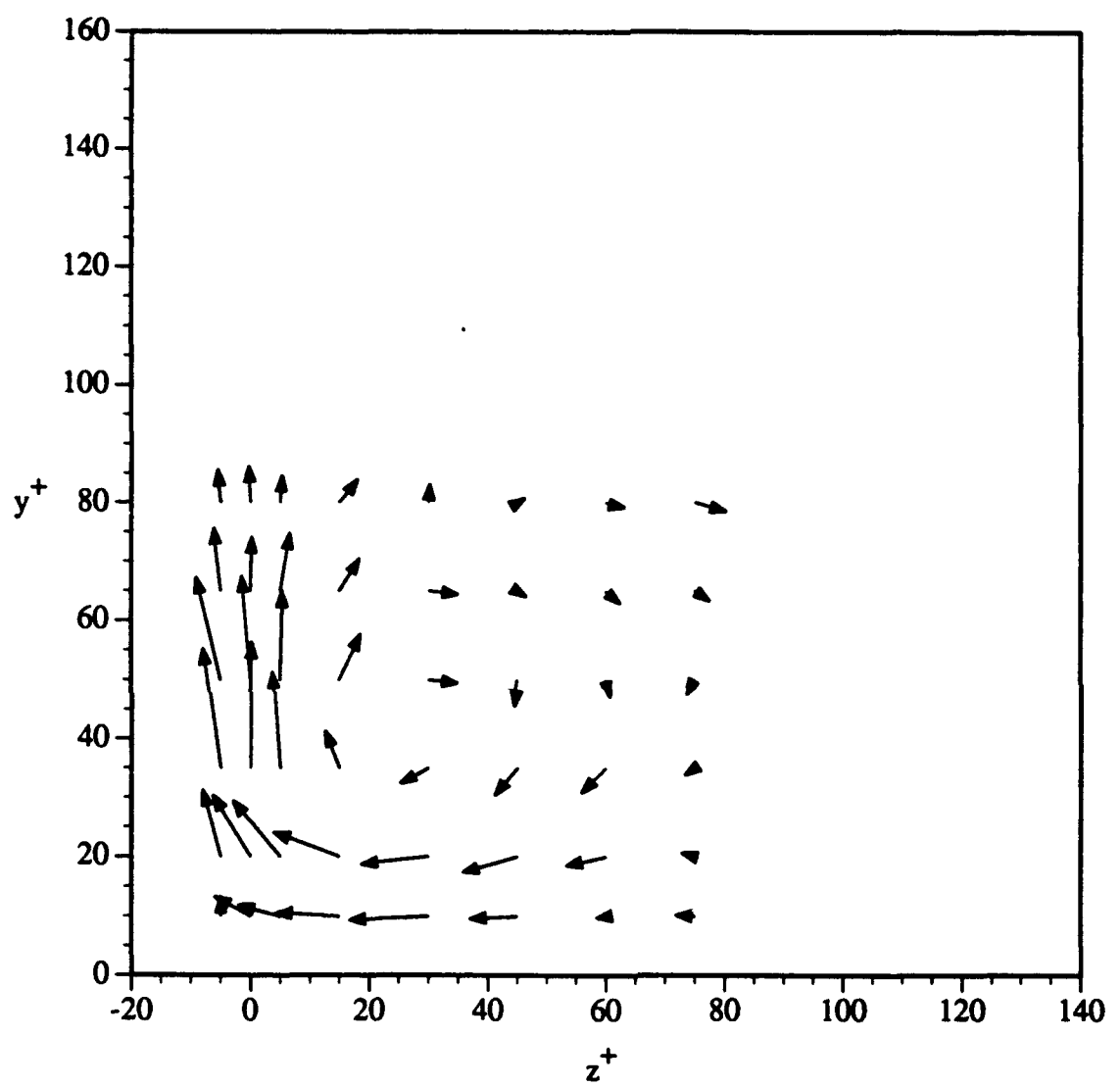


Figure 8(a) Spanwise cross-section of the quadrant burst detected at  $y_d^+ = 30$ .  
v-w velocity vectors.

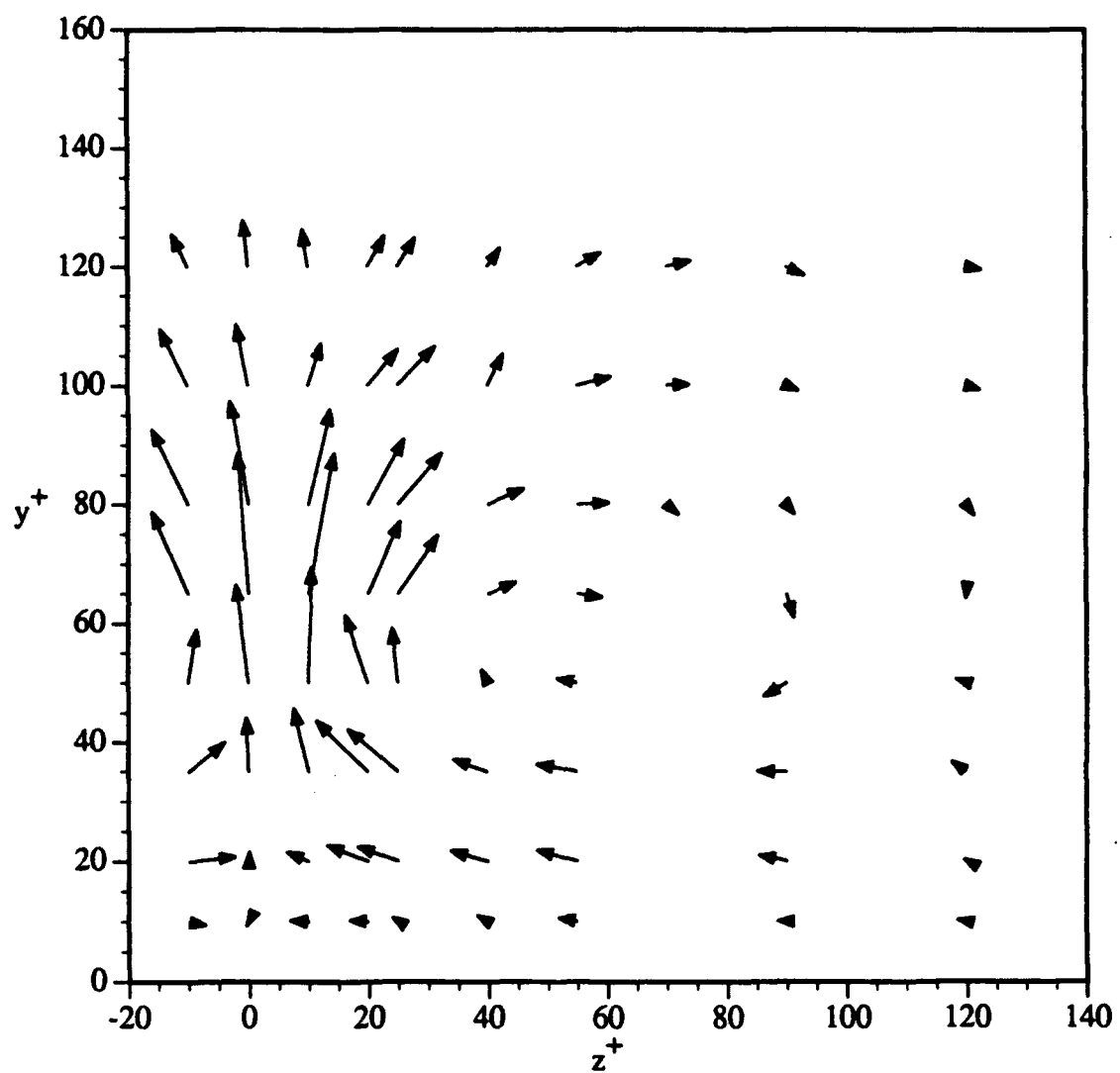


Figure 8(b) Spanwise cross-section of the quadrant burst detected at  $y_d^+ = 60$ .  
v-w velocity vectors.

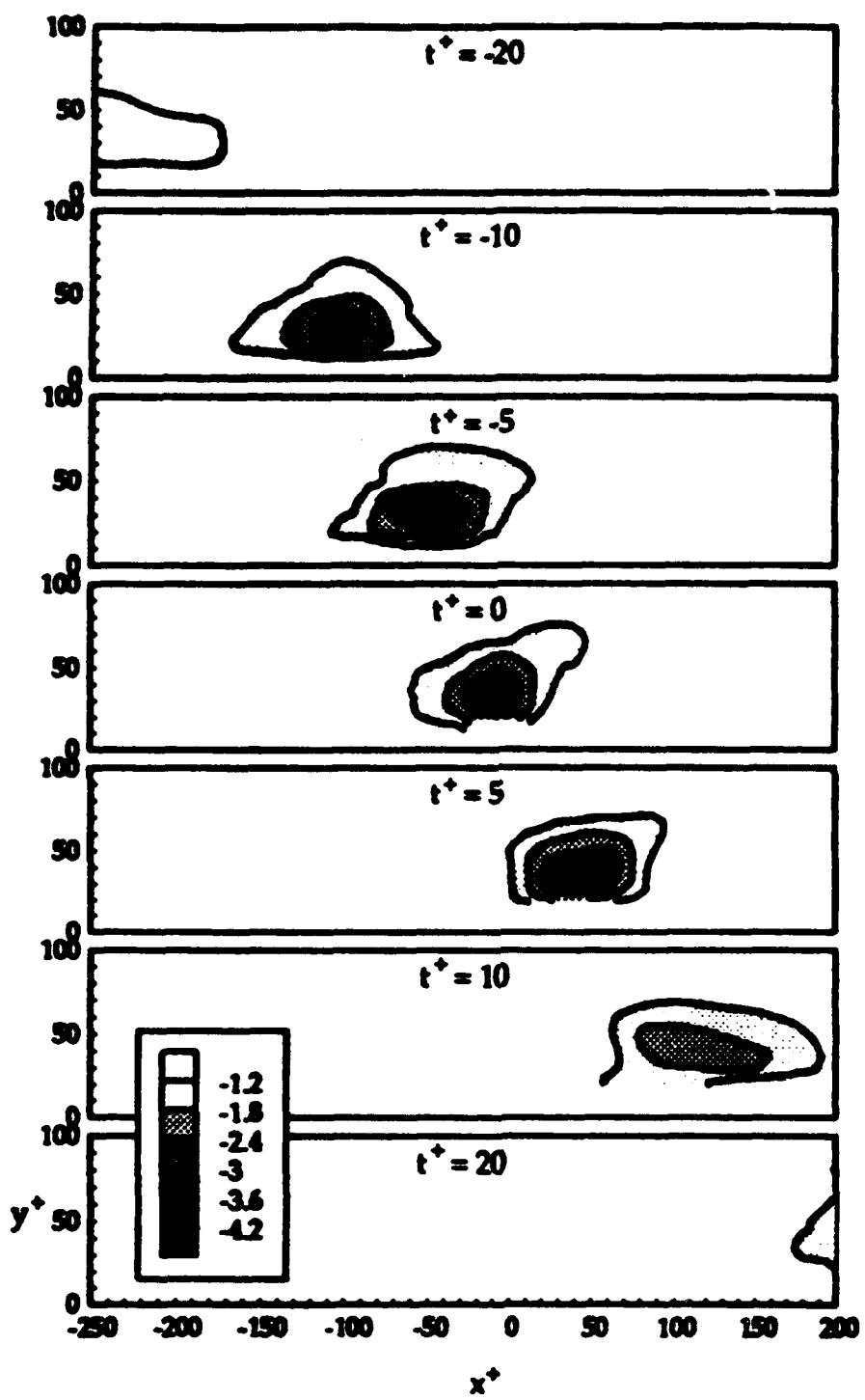


Figure 9 Evolution of  $uv$  contours for a quadrant burst detected at  $y_d^+ = 30$ .  
Contour increments of  $(uv)^+ = 0.6$ .

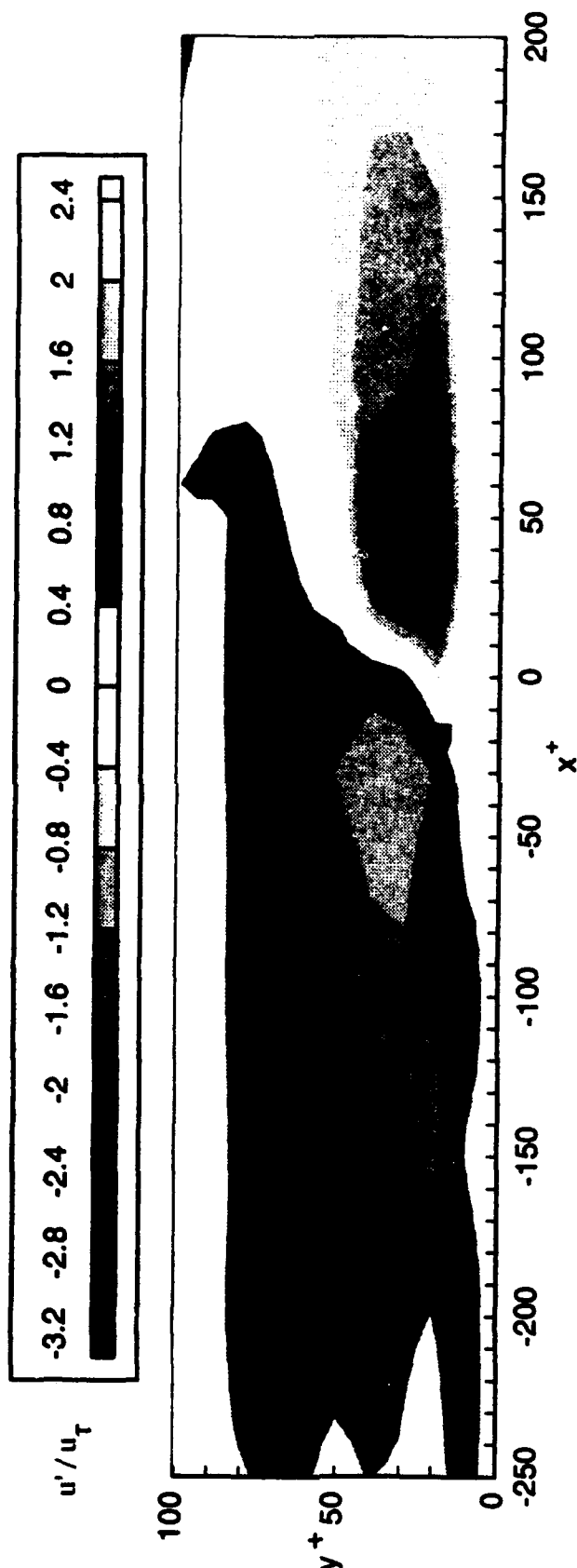


Figure 10 Ensemble averaged  $u$  velocity signal associated with the shear layer event detected at  $y^+ = 30$ .  
Contour increments of  $u^+ = 0.4$ .

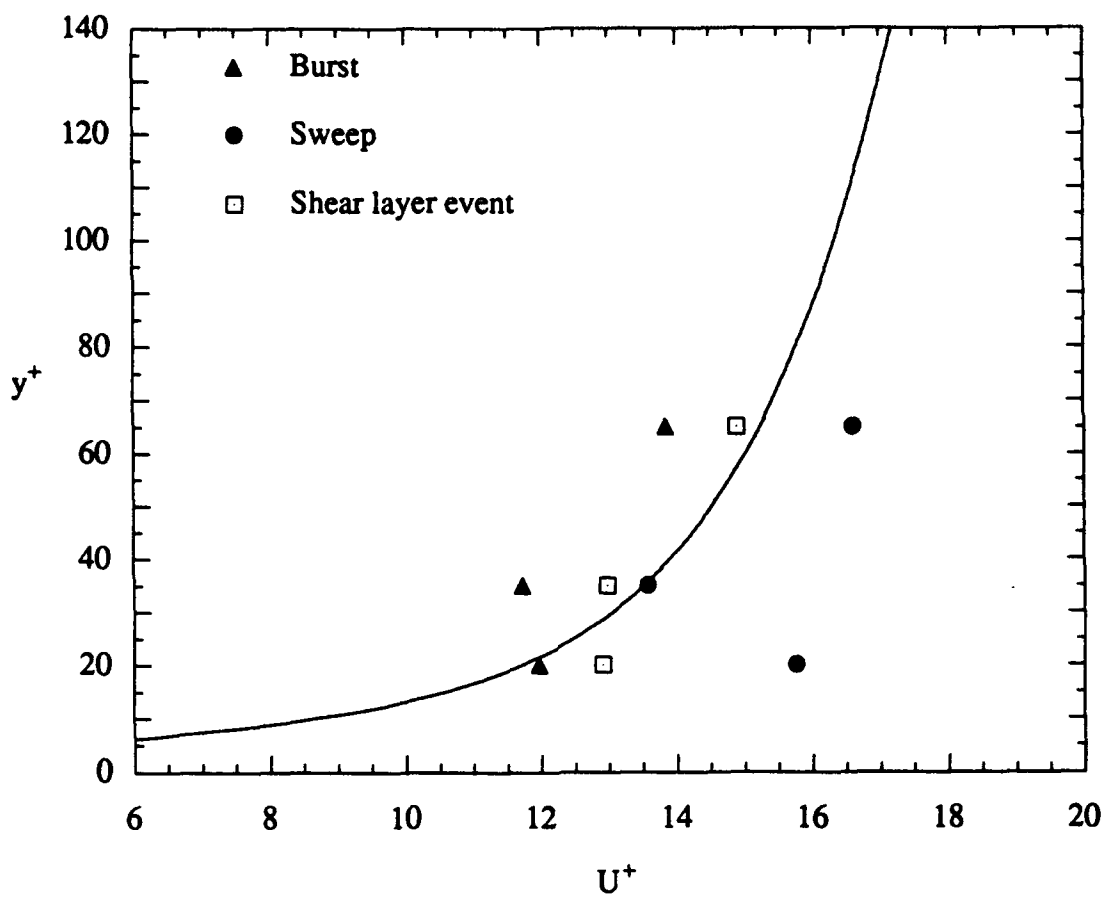
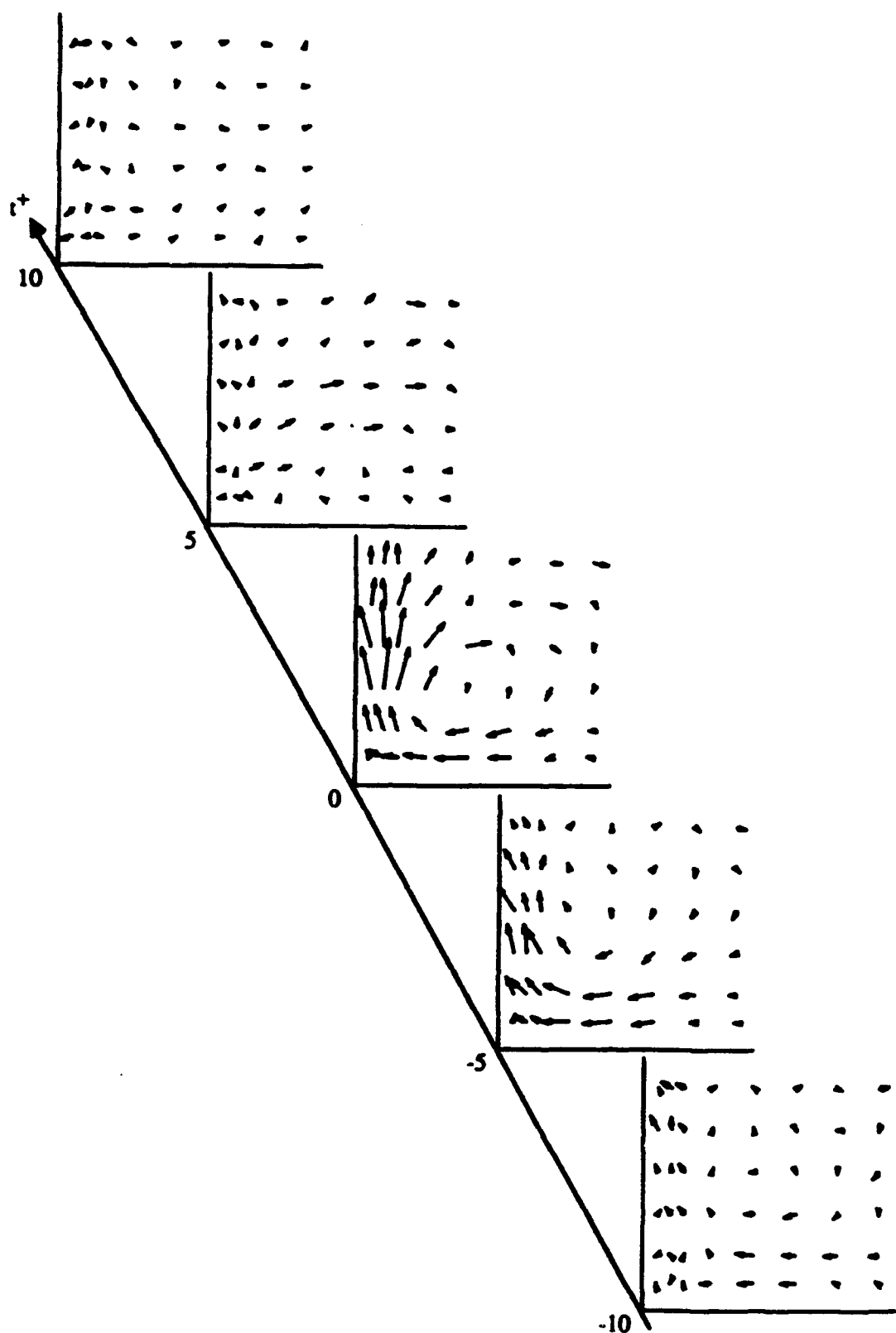
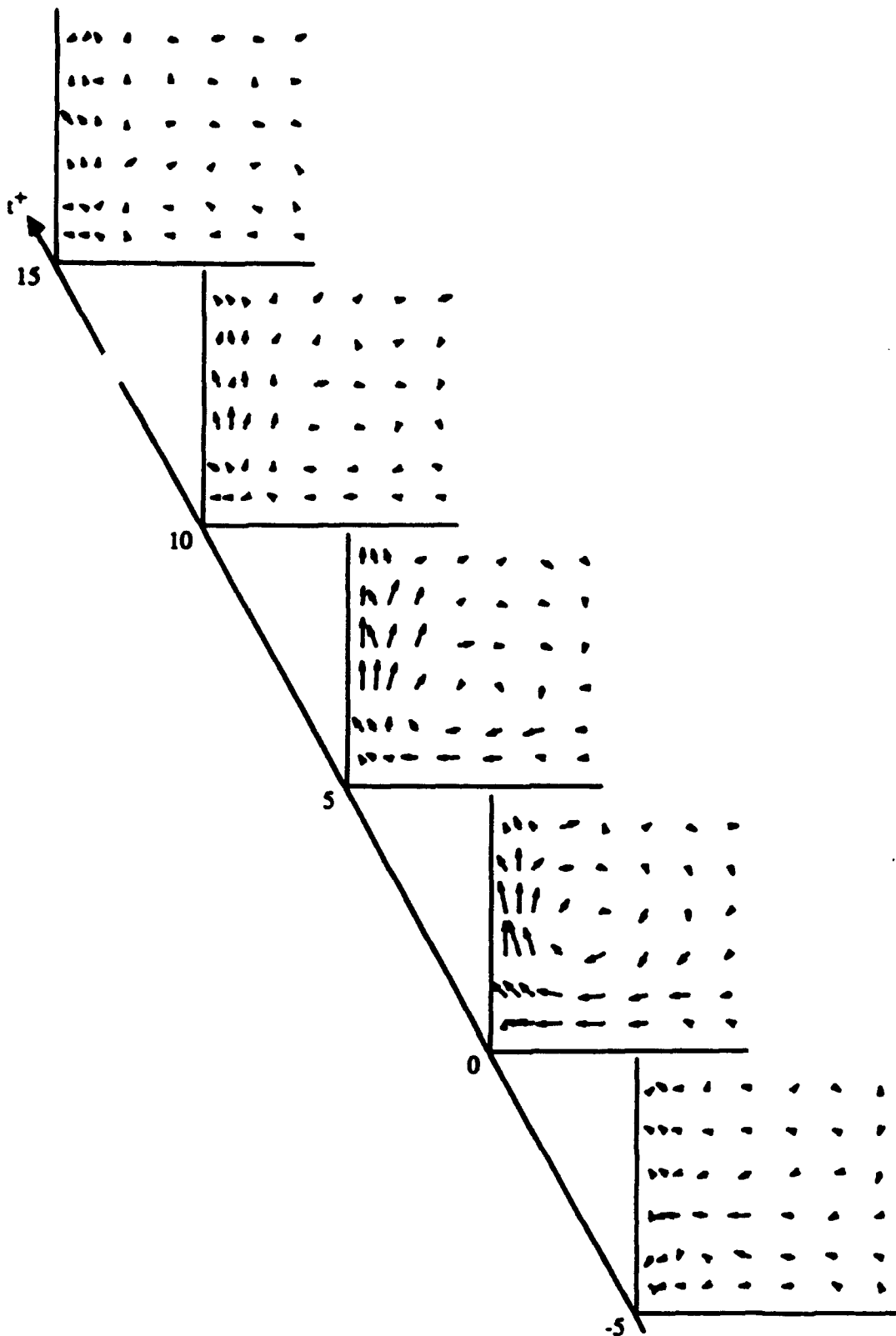


Figure 11 Convection velocities of the burst, sweep, and shear layer event detected at  $y^+ = 20, 30.$



**Figure 12** Time sequence of  $v$ - $w$  velocity vectors for a quadrant burst detected at  $y_d^+ = 30$ . Conditional samples centered on maximum  $-uv$ .



**Figure 13** Time sequence of  $v-w$  velocity vectors for a quadrant burst detected at  $y_d^+ = 30$ . Conditional samples centered on the leading edge of the uv pulse.

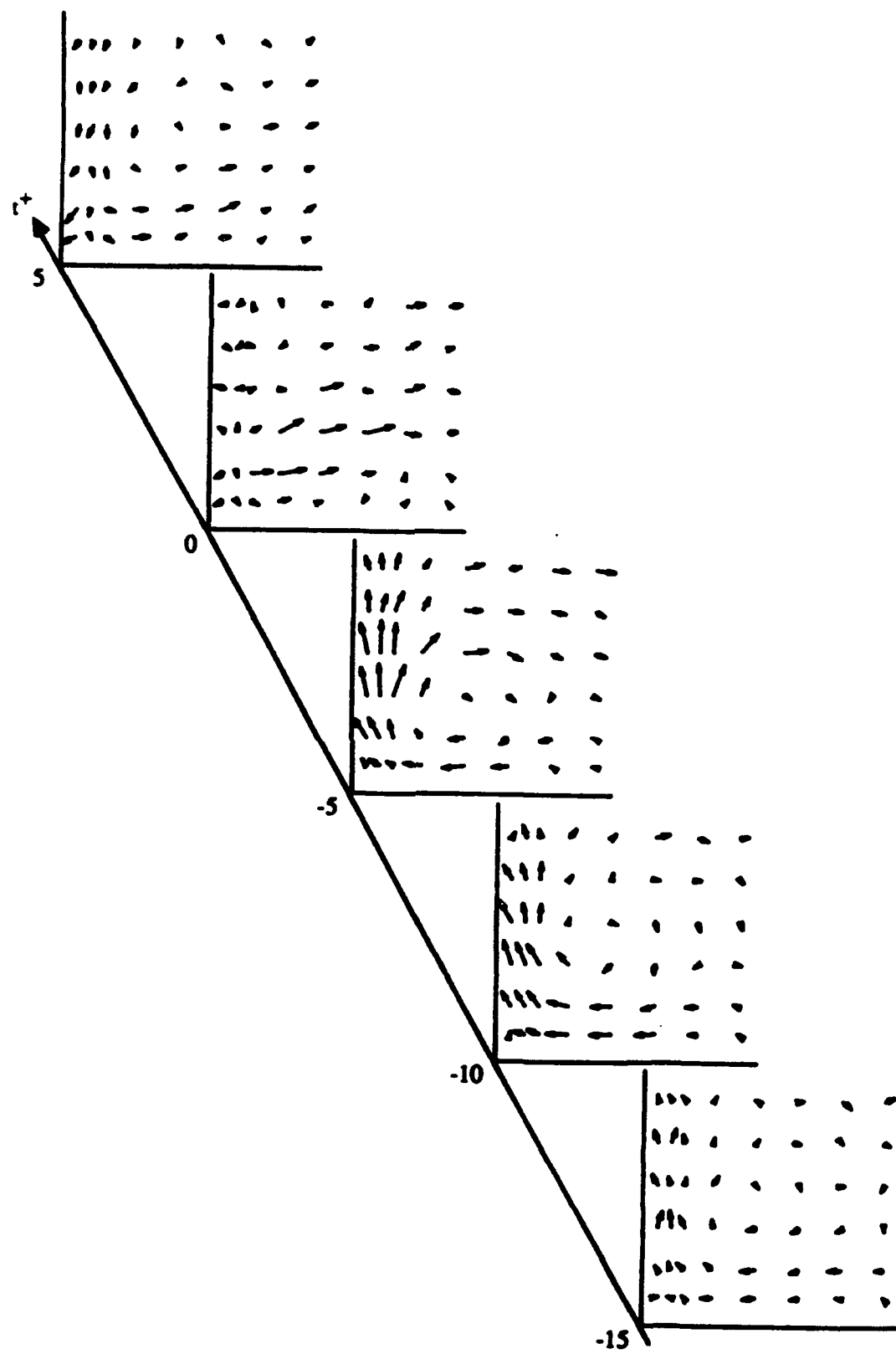


**Figure 14** Time sequence of v-w velocity vectors for a quadrant burst detected at  $y_d^+ = 30$ . Conditional samples centered on the trailing edge of the uv pulse.

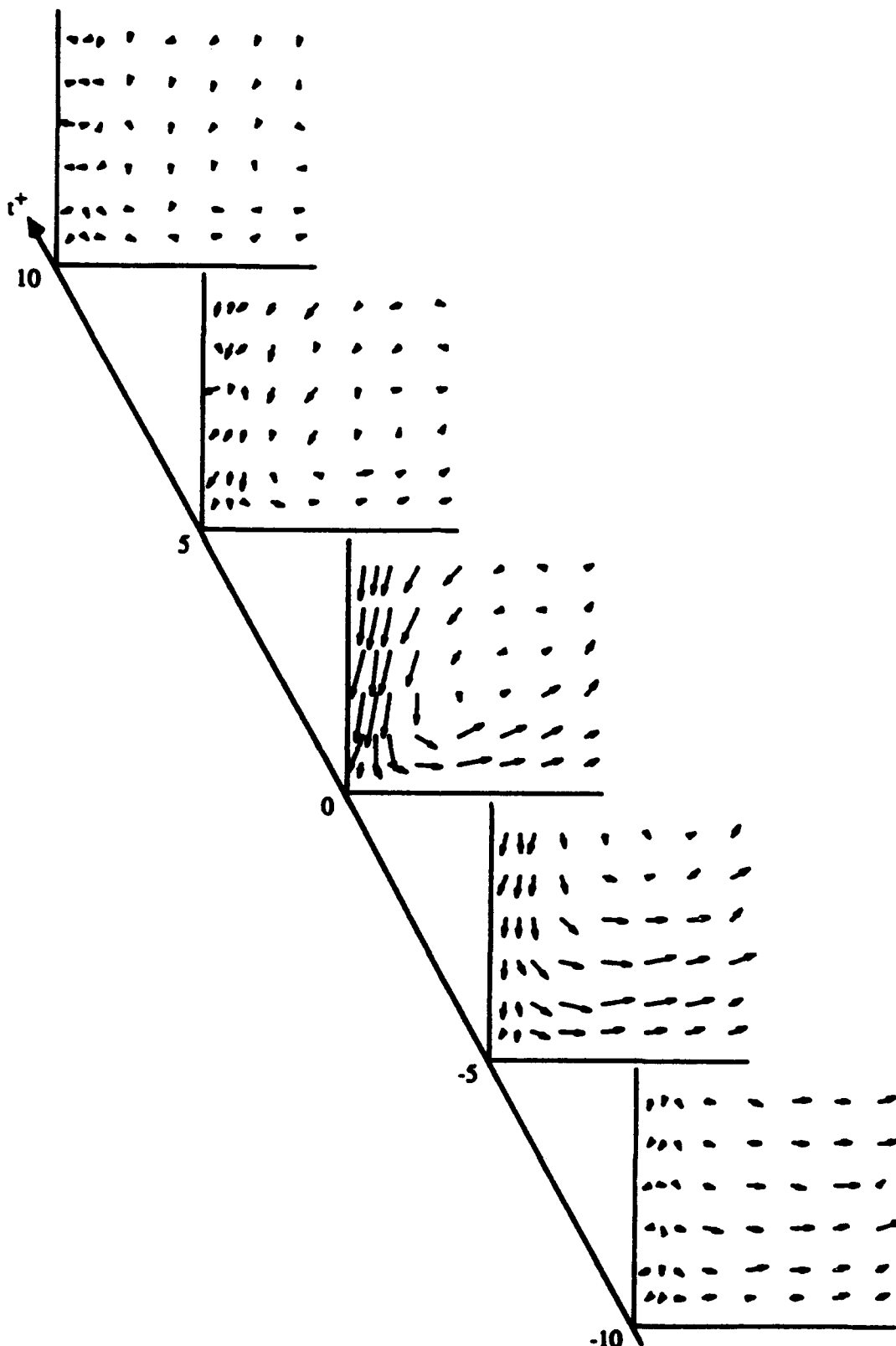


**Figure 15** Time sequence of  $v-w$  velocity vectors for a quadrant sweep detected at  $y_d^+ = 30$ . Conditional samples centered on maximum  $-uv$ .

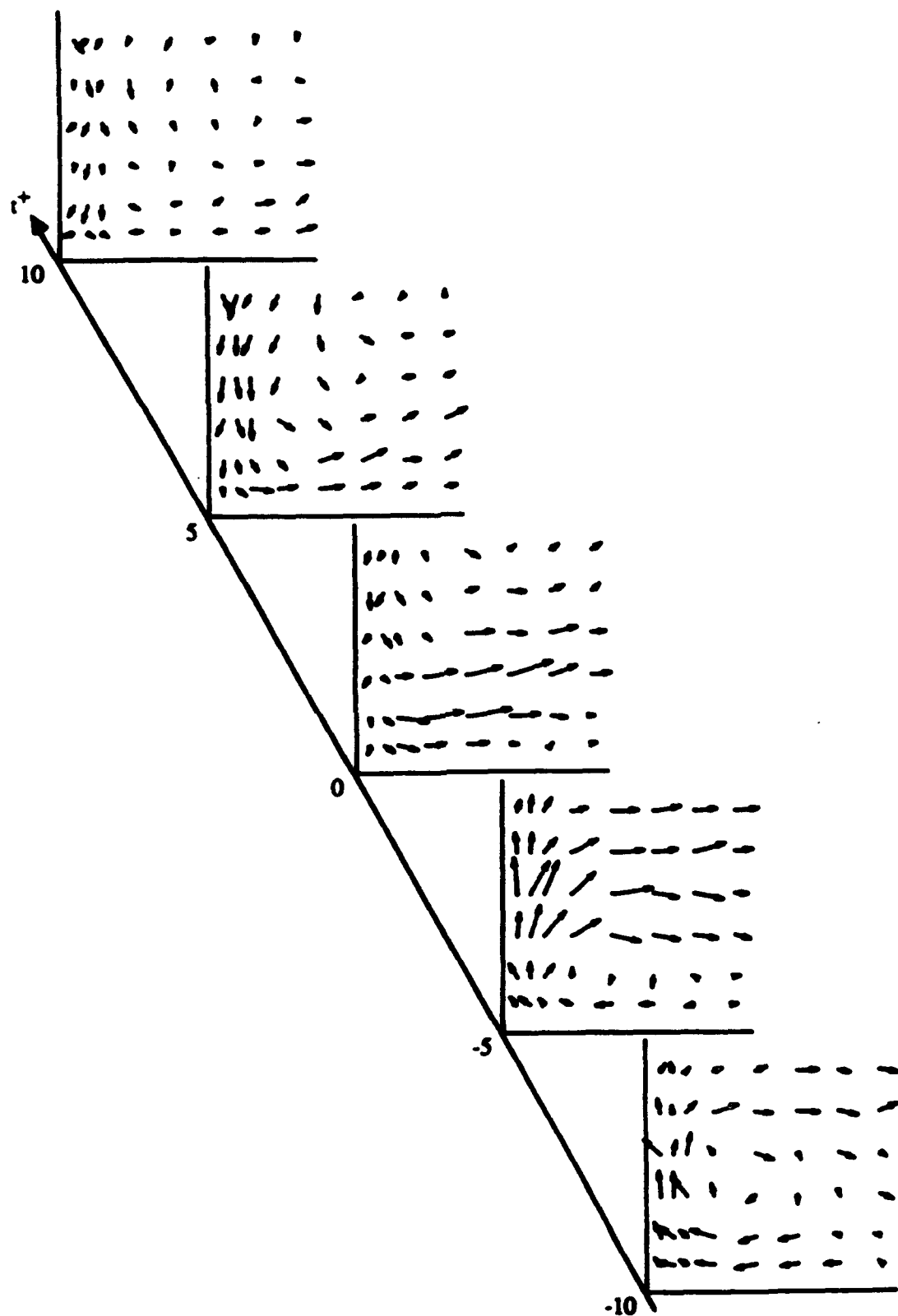
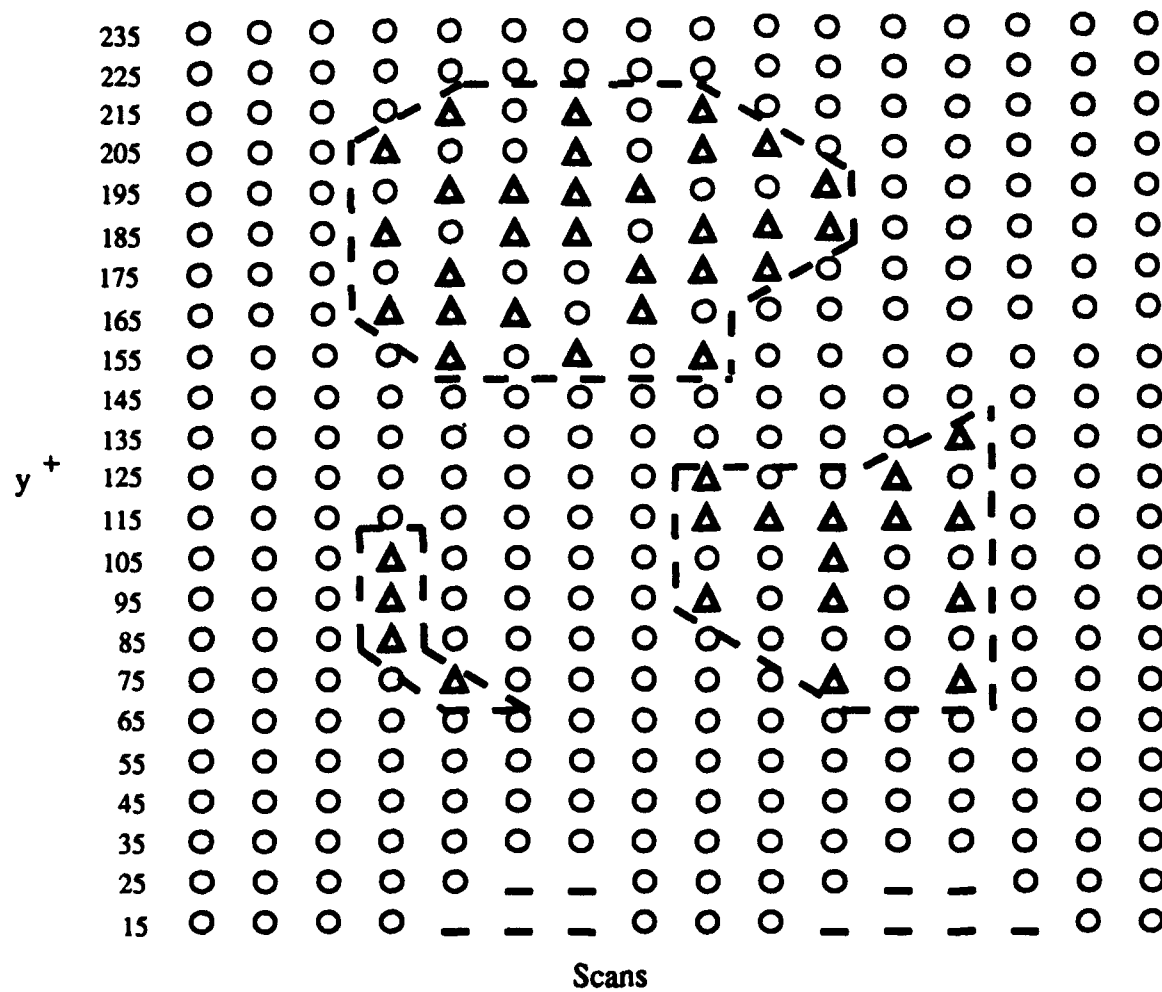


**Figure 16** Time sequence of v-w velocity vectors for a VITA shear layer detected at  $y_d^+ = 30$ . Conditional samples aligned with the center of the VITA event.



$\Delta$  Local velocity magnitude greater than threshold,  $u > L u_{rms}$

O Local velocity magnitude less than threshold

- No data

Figure 17 Schematic for the grouping of events using the spatial detection technique. Separate spatial structures indicated by dashed lines.

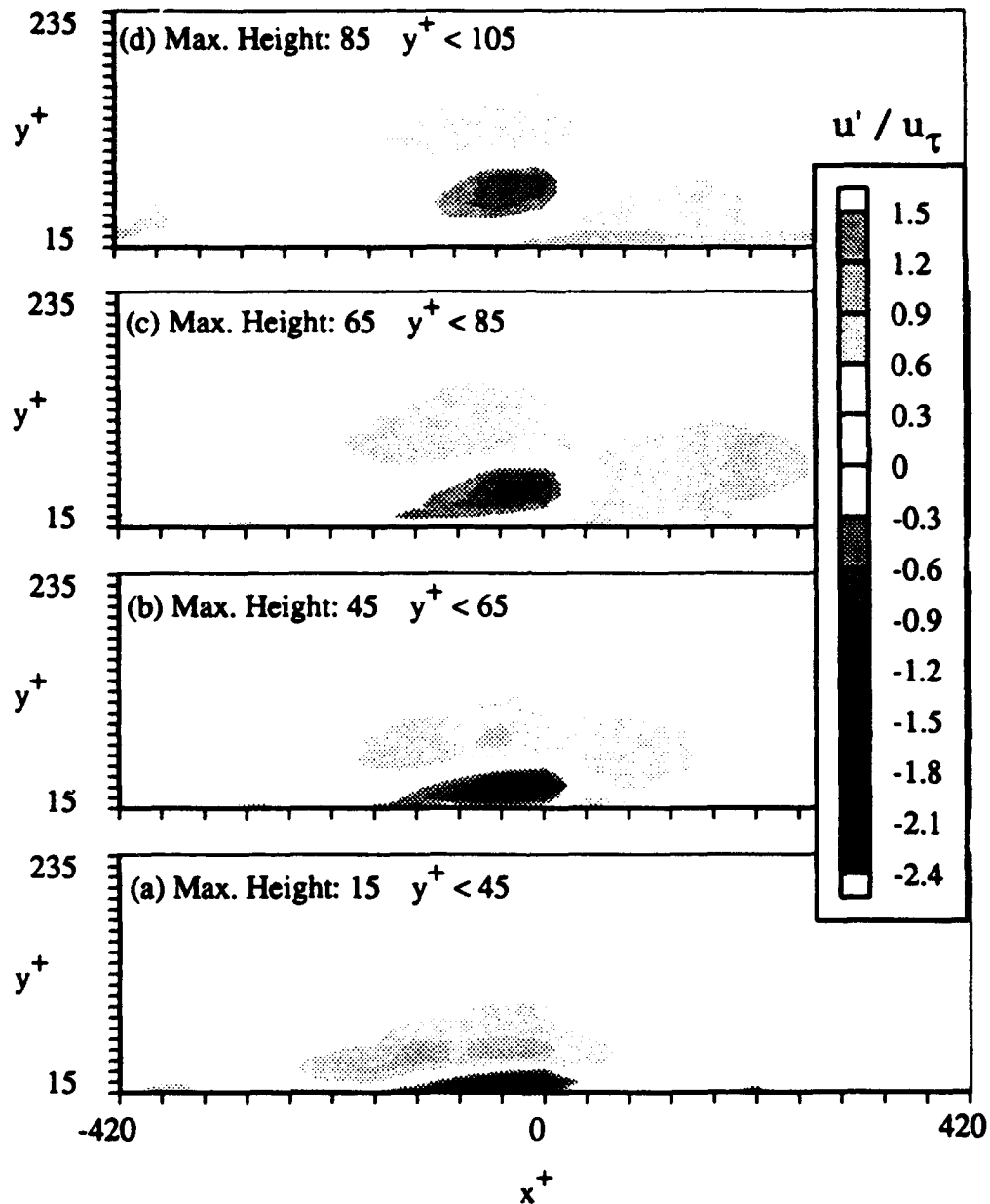


**Figure 18** Low speed events over a smooth wall. Conditional samples based on spatial detection. Indicated heights are a classification of events in terms of the maximum height of the event.

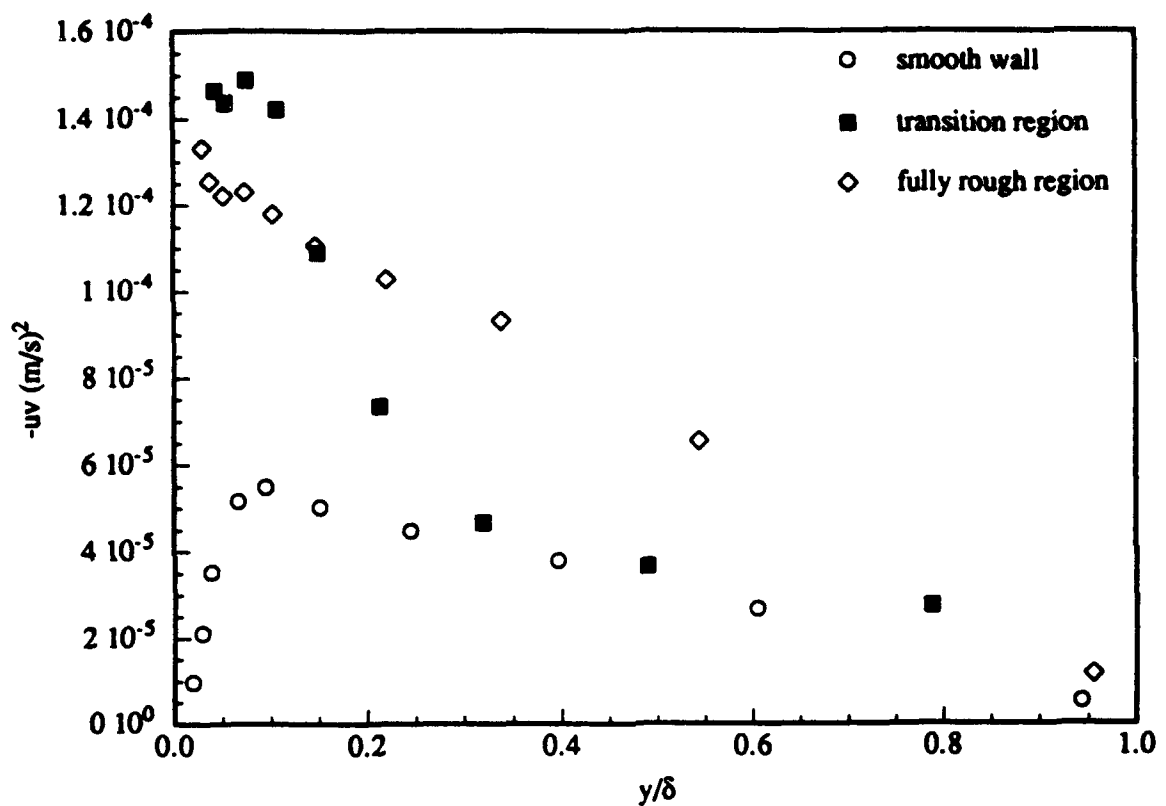


**Figure 19** Profiles of  $\bar{u}\bar{v}$  immediately upstream of the rough surface,  $x = -\delta_0$ , following the start of roughness,  $x = 2\delta_0$ , and in the fully developed rough wall flow,  $x = 24\delta_0$ .

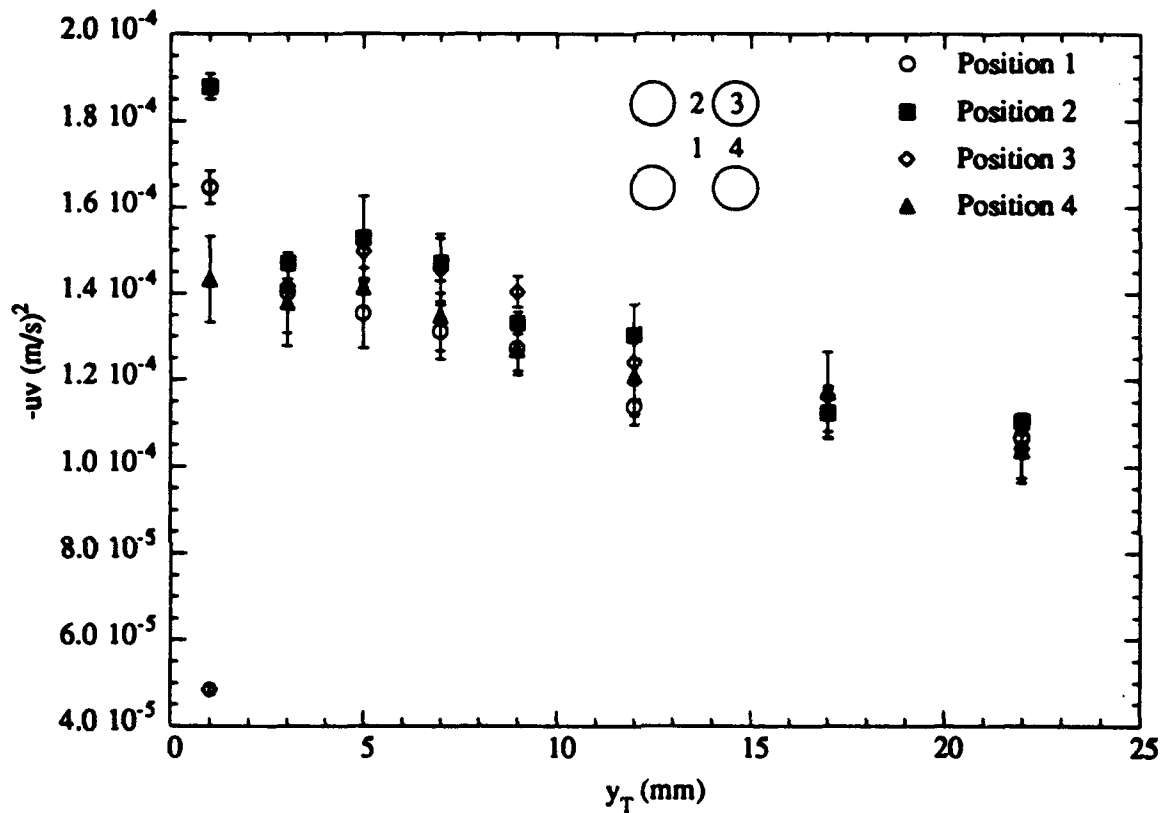
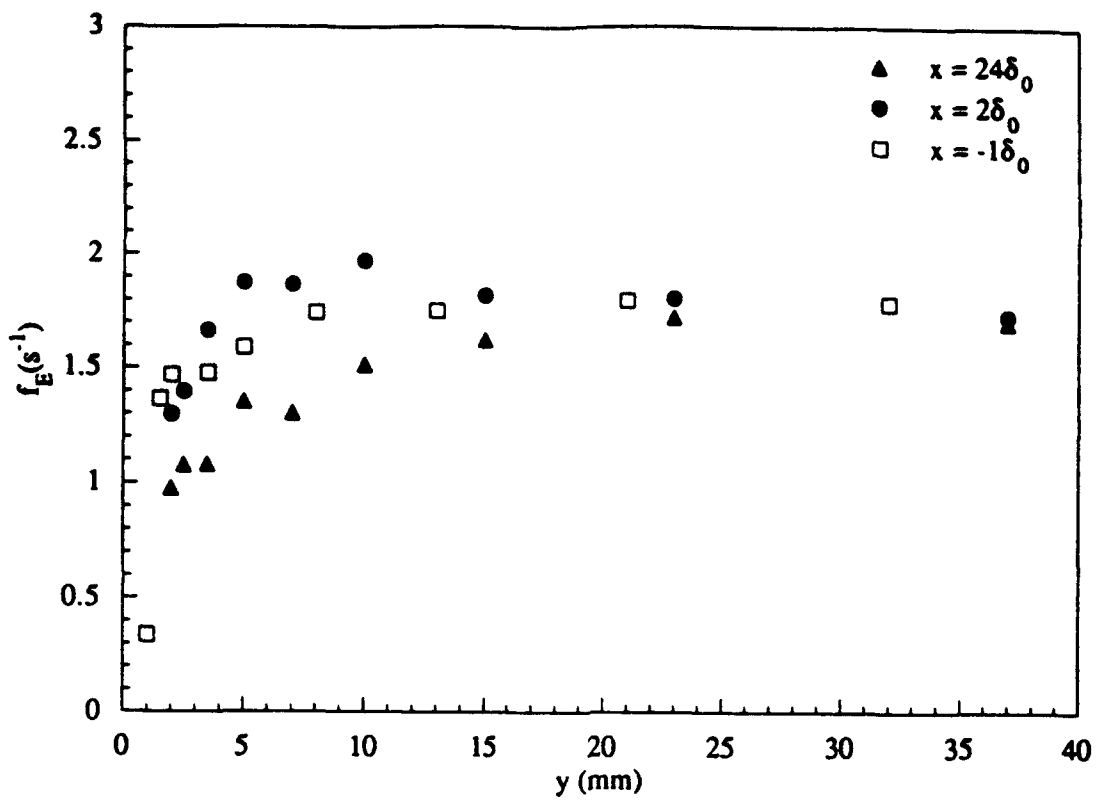
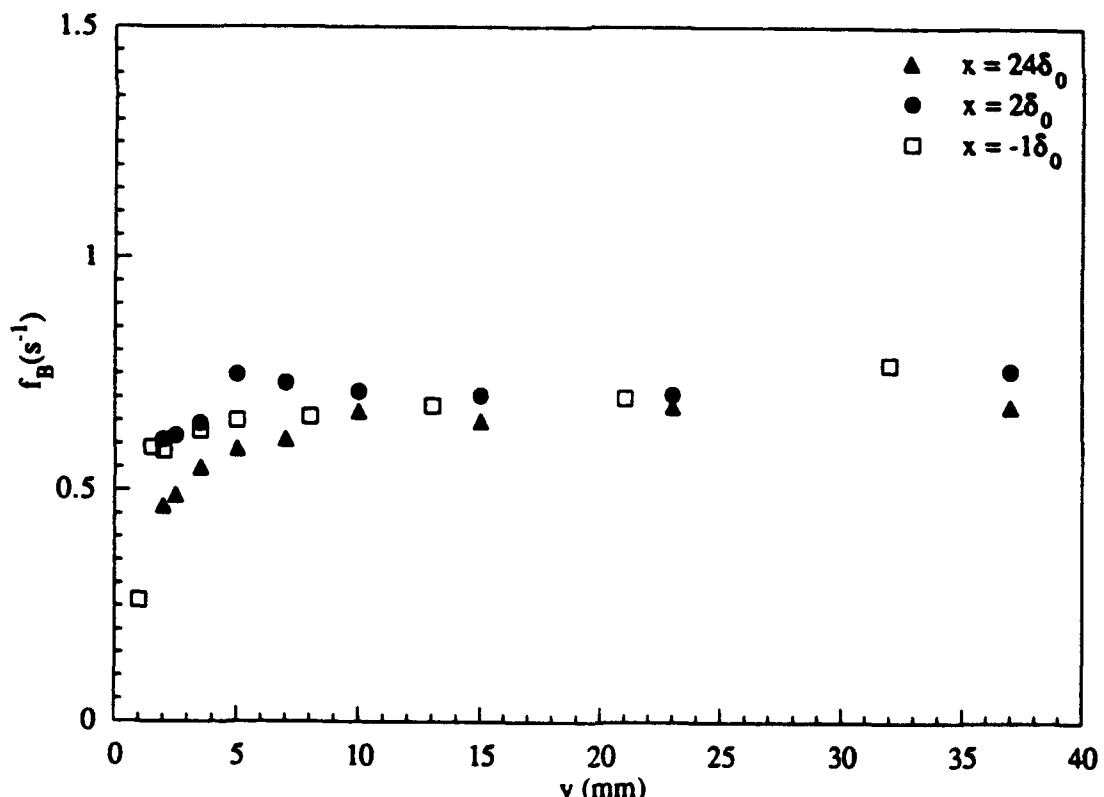


**Figure 20** Effect of position with respect to the roughness elements on the  $\bar{u}\bar{v}$  profiles for fully developed rough wall flow.

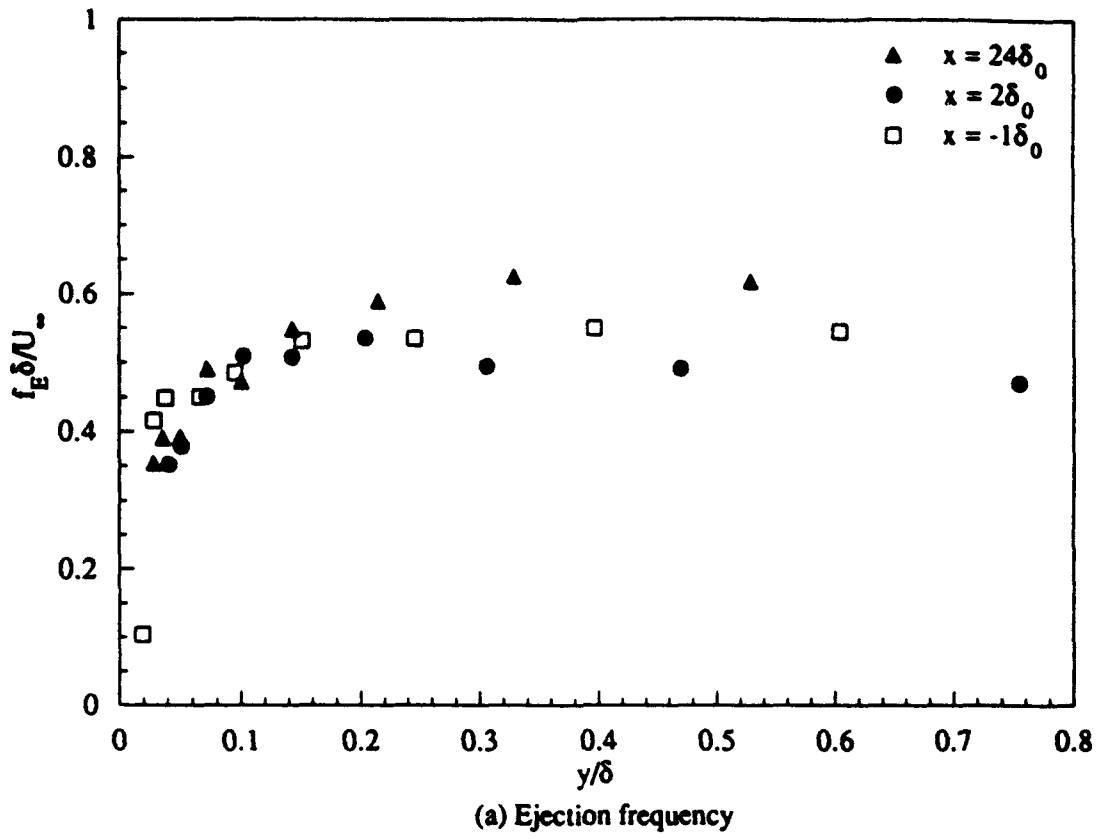


(a) Ejection frequency

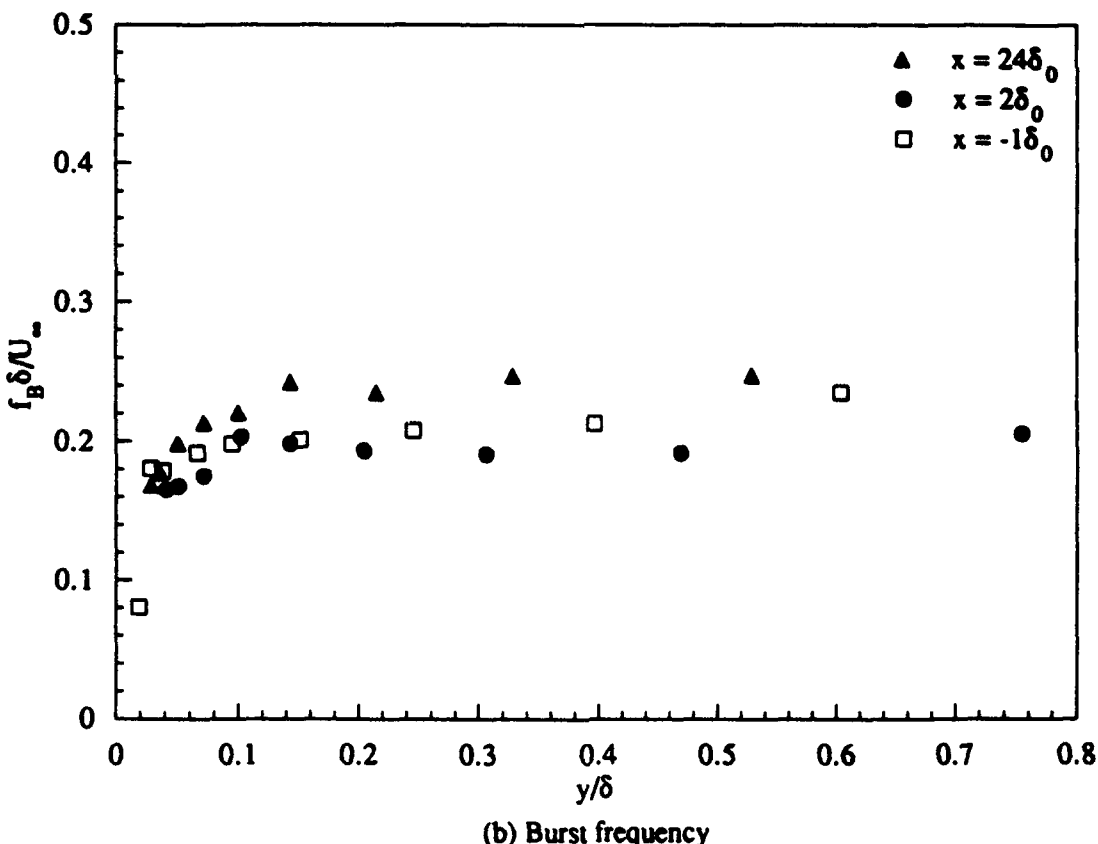


(b) Burst frequency

Figure 21 Effect of the rough surface on the (a) ejection and (b) burst frequencies.  
Quadrant detection with threshold  $H = 1.0 u'v'$ .



(a) Ejection frequency



(b) Burst frequency

Figure 22 Nondimensional (a) ejection and (b) burst frequencies for smooth and rough surfaces using outer variables. Quadrant detection with threshold  $H = 1.0 u'v'$ .

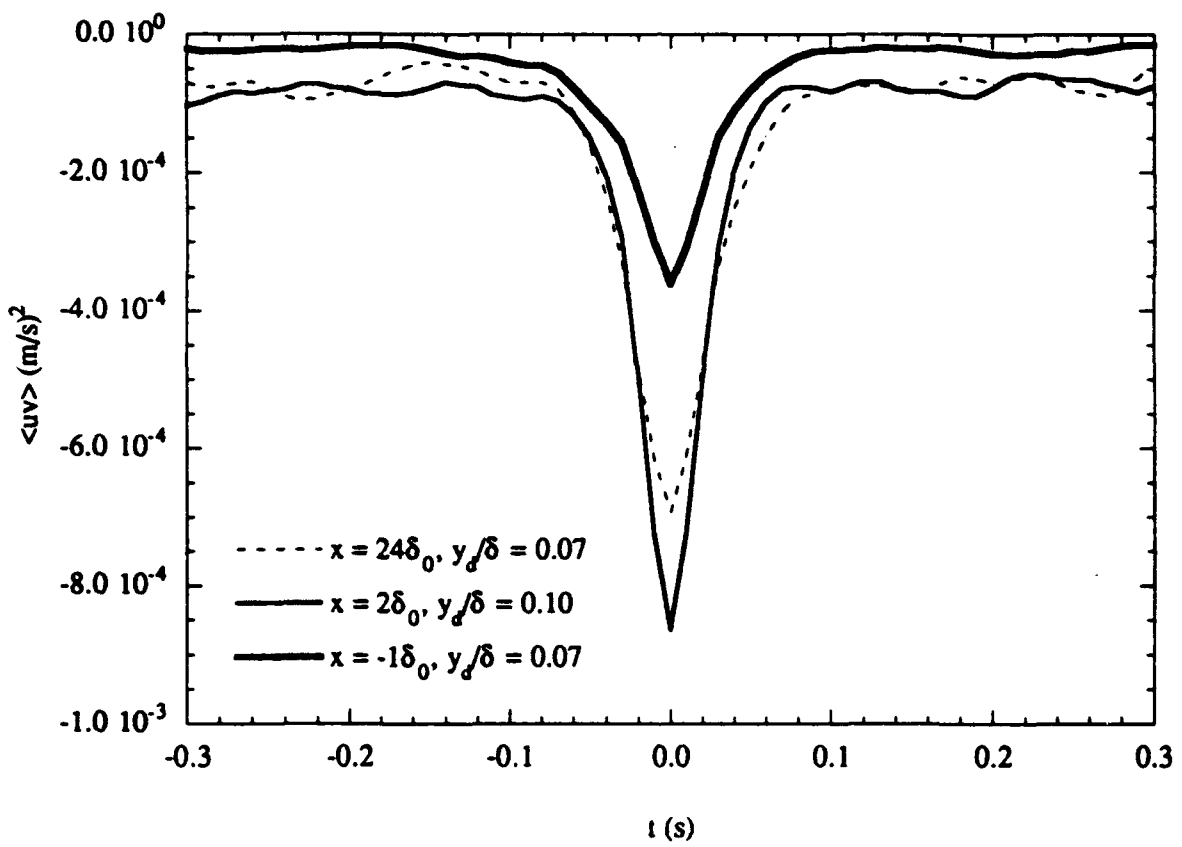


**Figure 23** Effect of the rough surface on the ensemble average of the conditionally sampled  $uv$  signal. Measurements and detection made with same probe located in the near wall constant stress layer. Quadrant detection with threshold  $H = 1.0 u'v'$ .

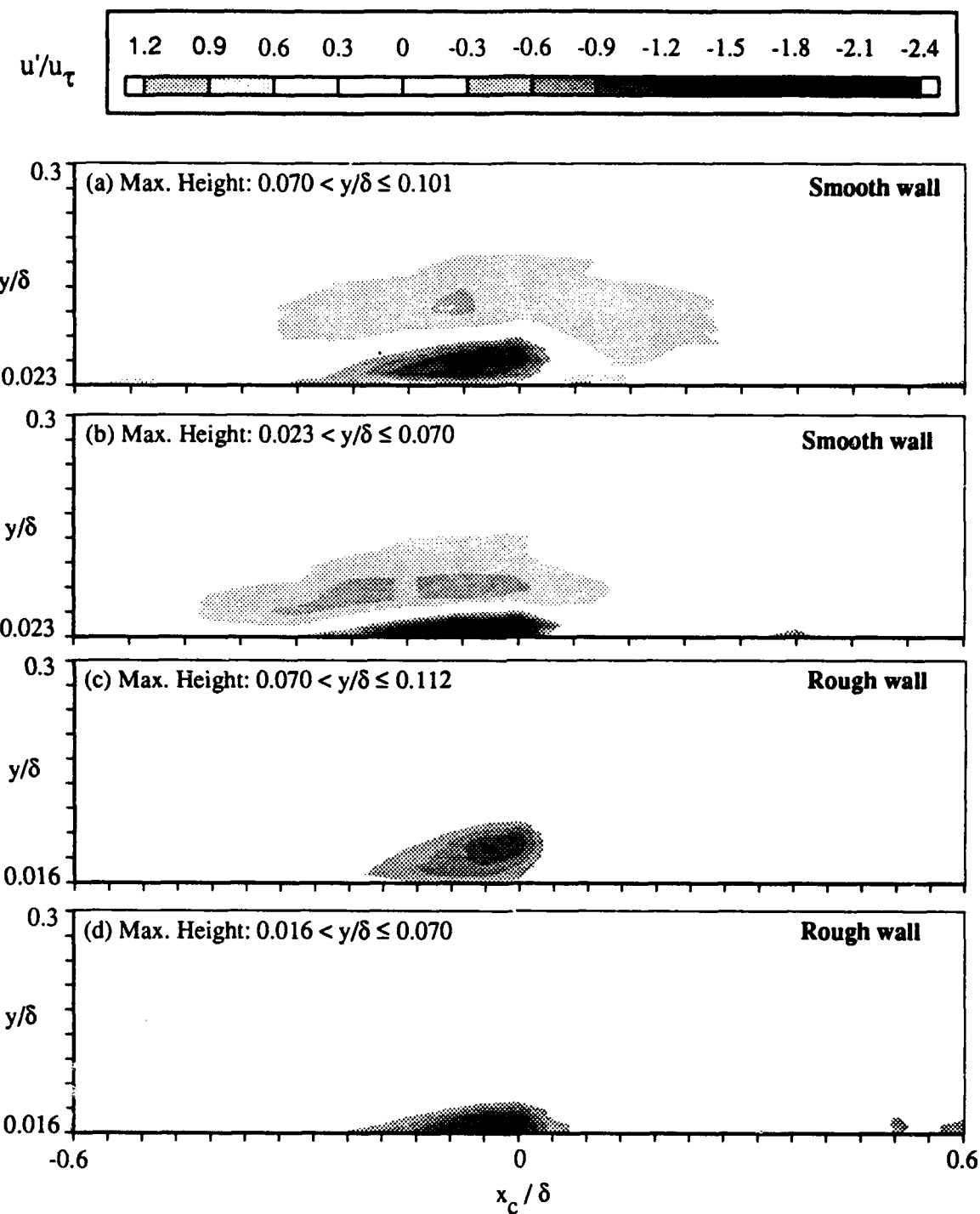
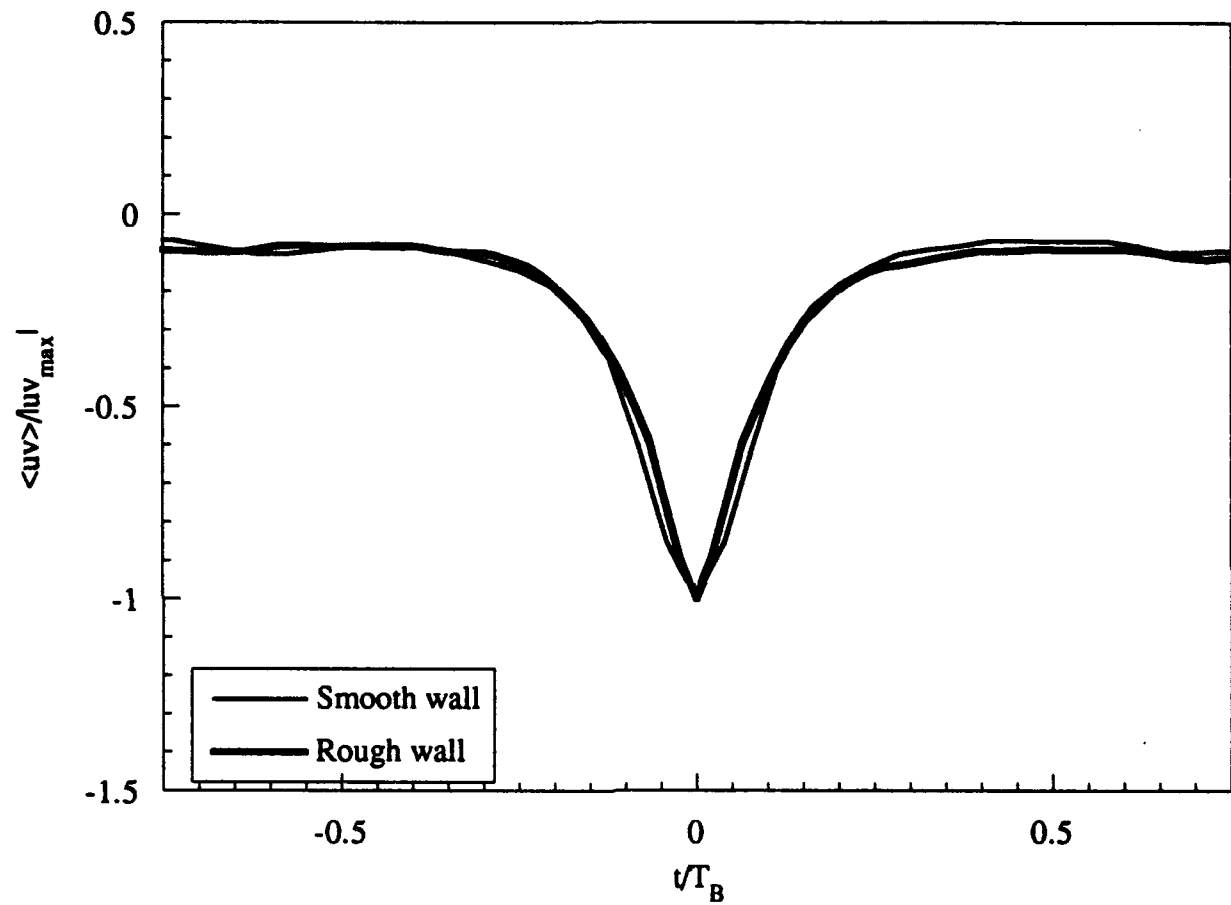


Figure 24 Low speed events over a rough and smooth wall. Conditional samples based on spatial detection. Indicated heights are a classification of events in terms of the maximum height of the event. Results are presented in terms of outer variables. An appropriate convection velocity was used to obtain  $x_c$  ( $x_c = t \cdot U_c$ ).



**Figure 25** Ensemble averaged conditional samples of smooth and rough wall bursts, with the time scale normalized by burst duration. Quadrant detection with threshold  $H = 1.0u'v'$ .

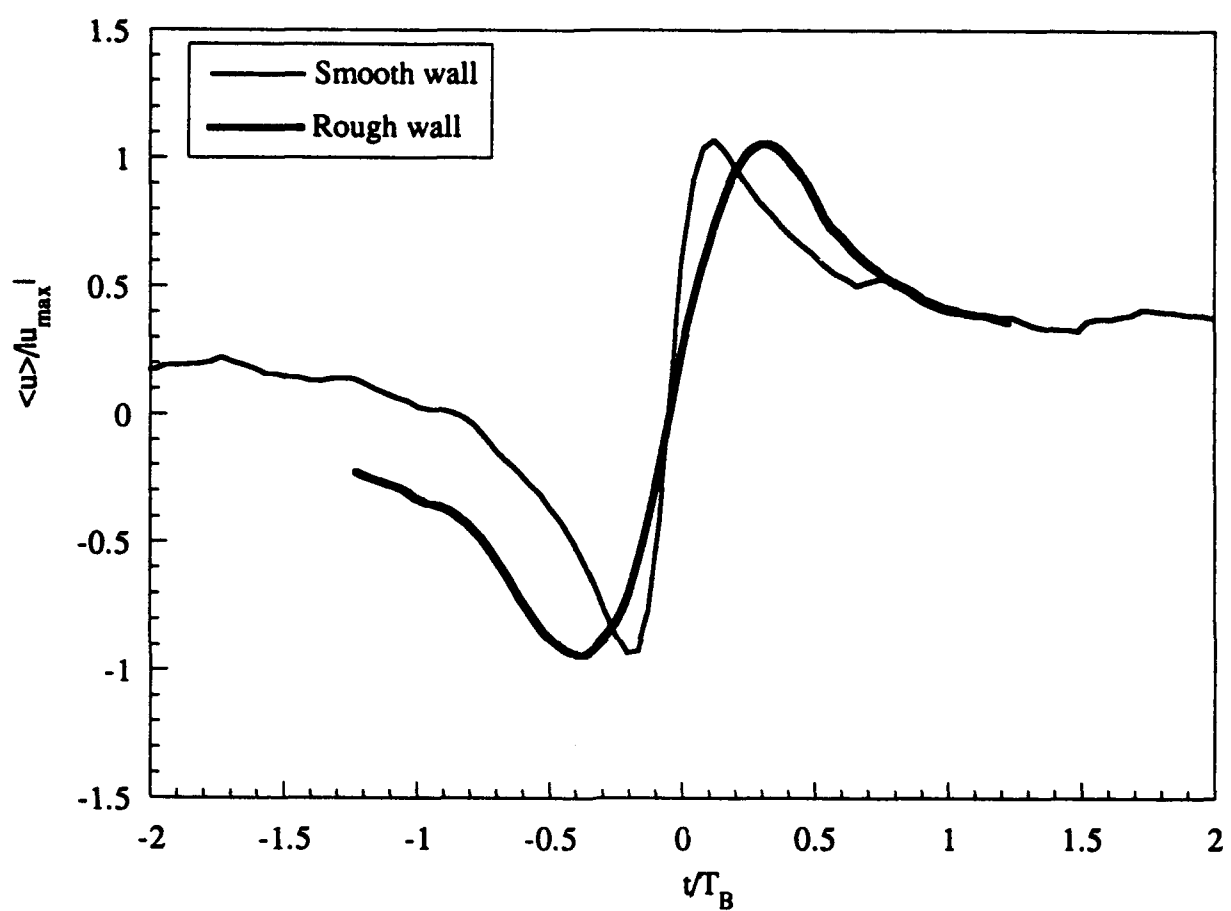
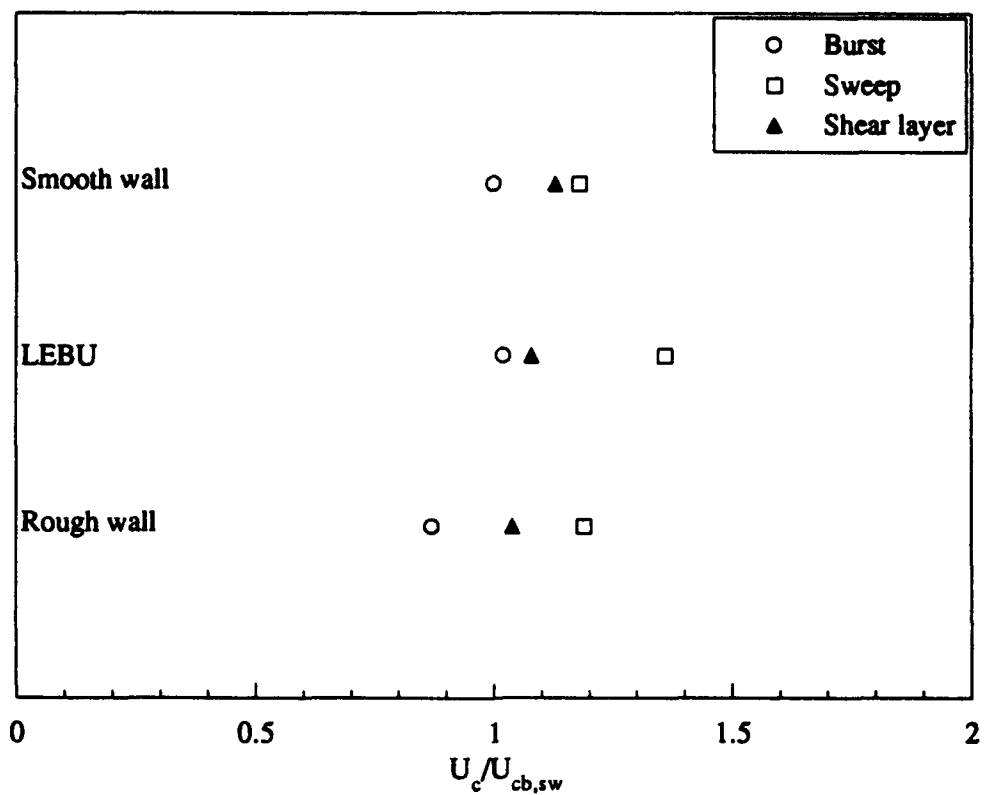


Figure 26 Ensemble averaged conditional samples of smooth and rough wall shear layer events with averaging time based on burst duration.  
VITA detection with positive slope criterion and threshold  $k = 1.0 u'$ .



**Figure 27** Convection velocities of the burst, sweep, and shear layer over the rough wall, and smooth wall with and without the LEBU device. Convection velocities relative to the convection velocity of the smooth wall burst without LEBU device.

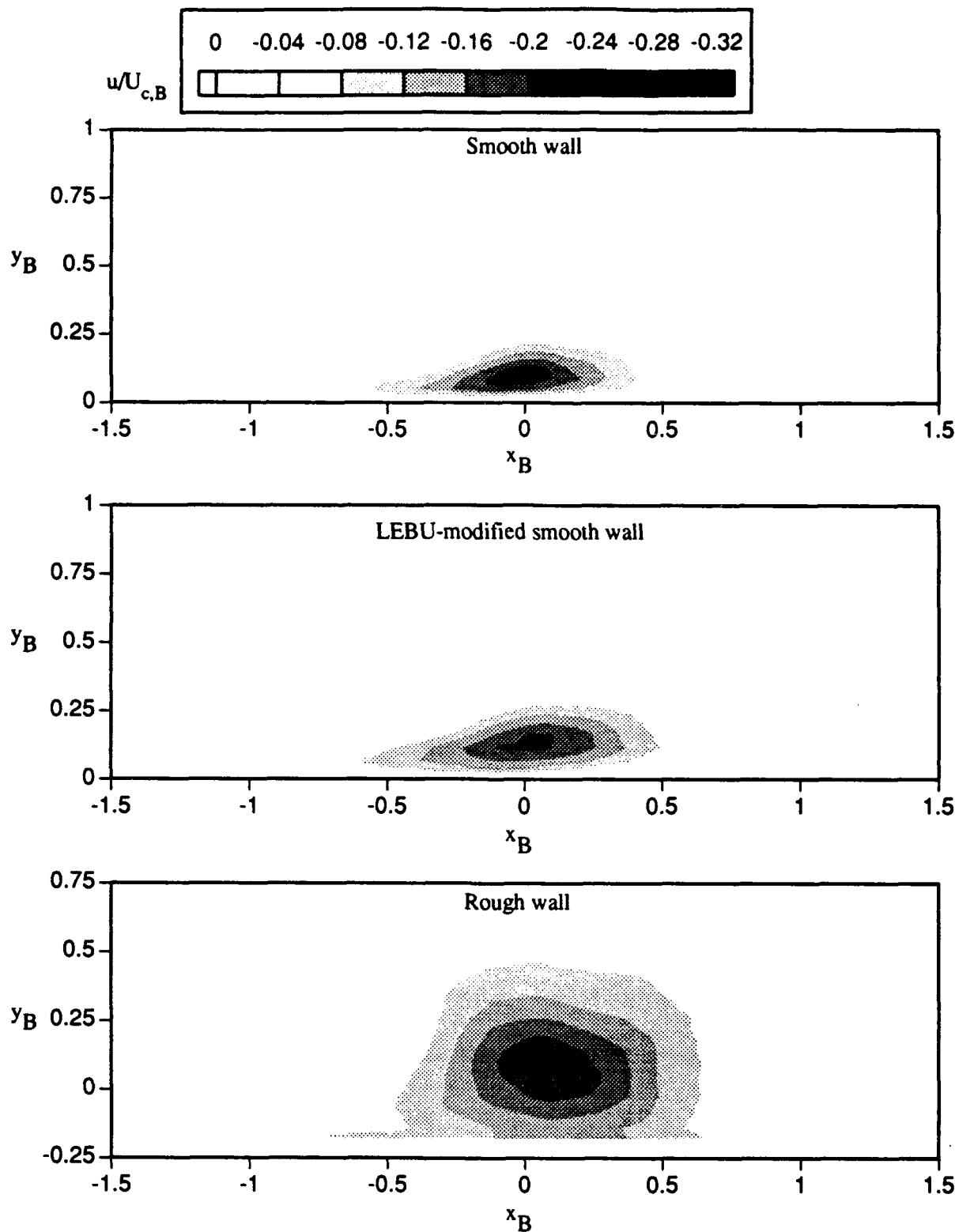


Figure 28 Ensemble averaged conditional samples of  $u$  velocity contours of the Quadrant burst over a smooth wall with and without the LEBU device, and over a rough wall. Length scales normalized by the length of the burst. Contour levels normalized by the burst convection velocity.

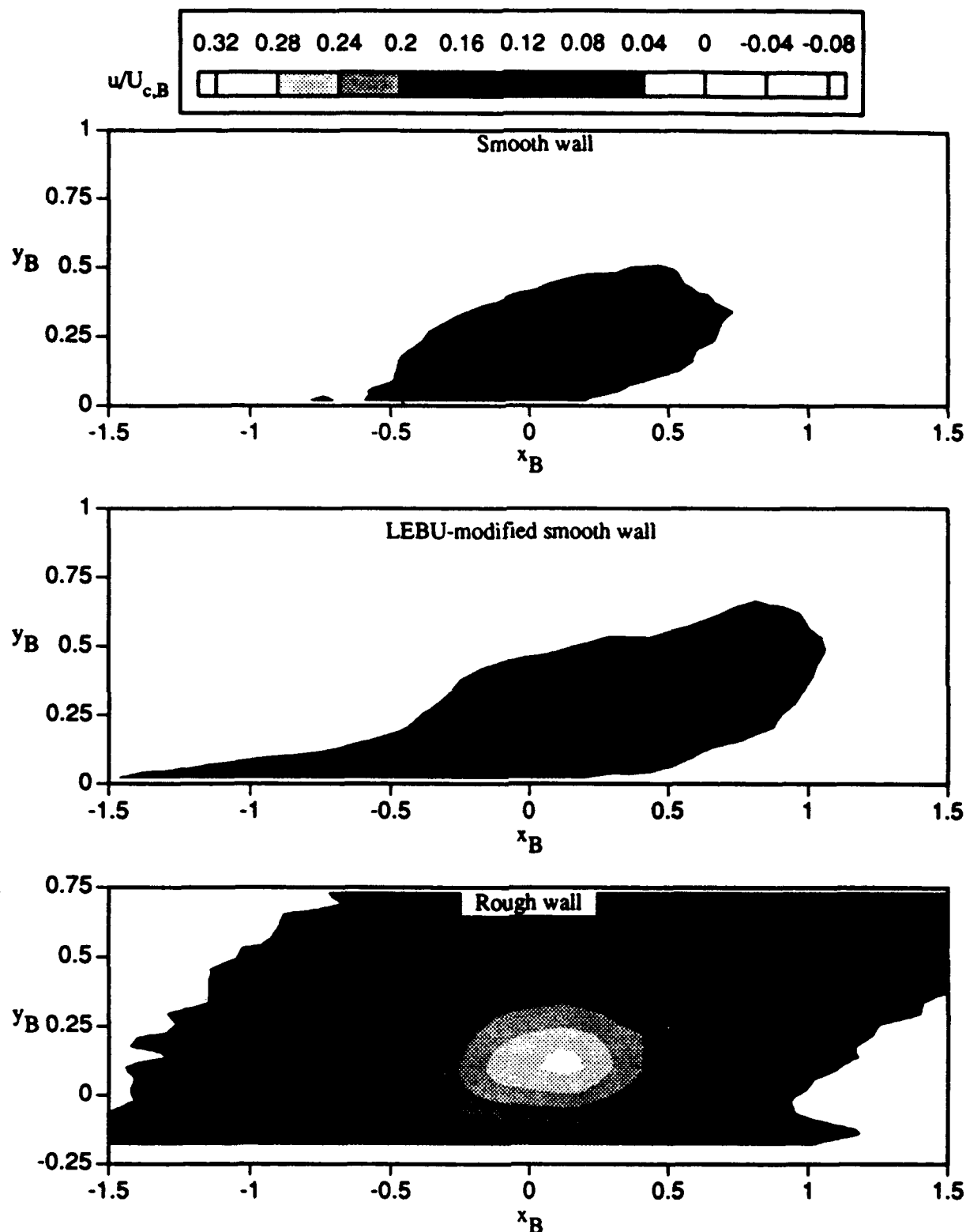


Figure 29 Ensemble averaged conditional samples of  $u$  velocity contours of the Quadrant sweep over a smooth wall with and without the LEBU device, and over a rough wall. Length scales normalized by the length of the burst. Contour levels normalized by the burst convection velocity.

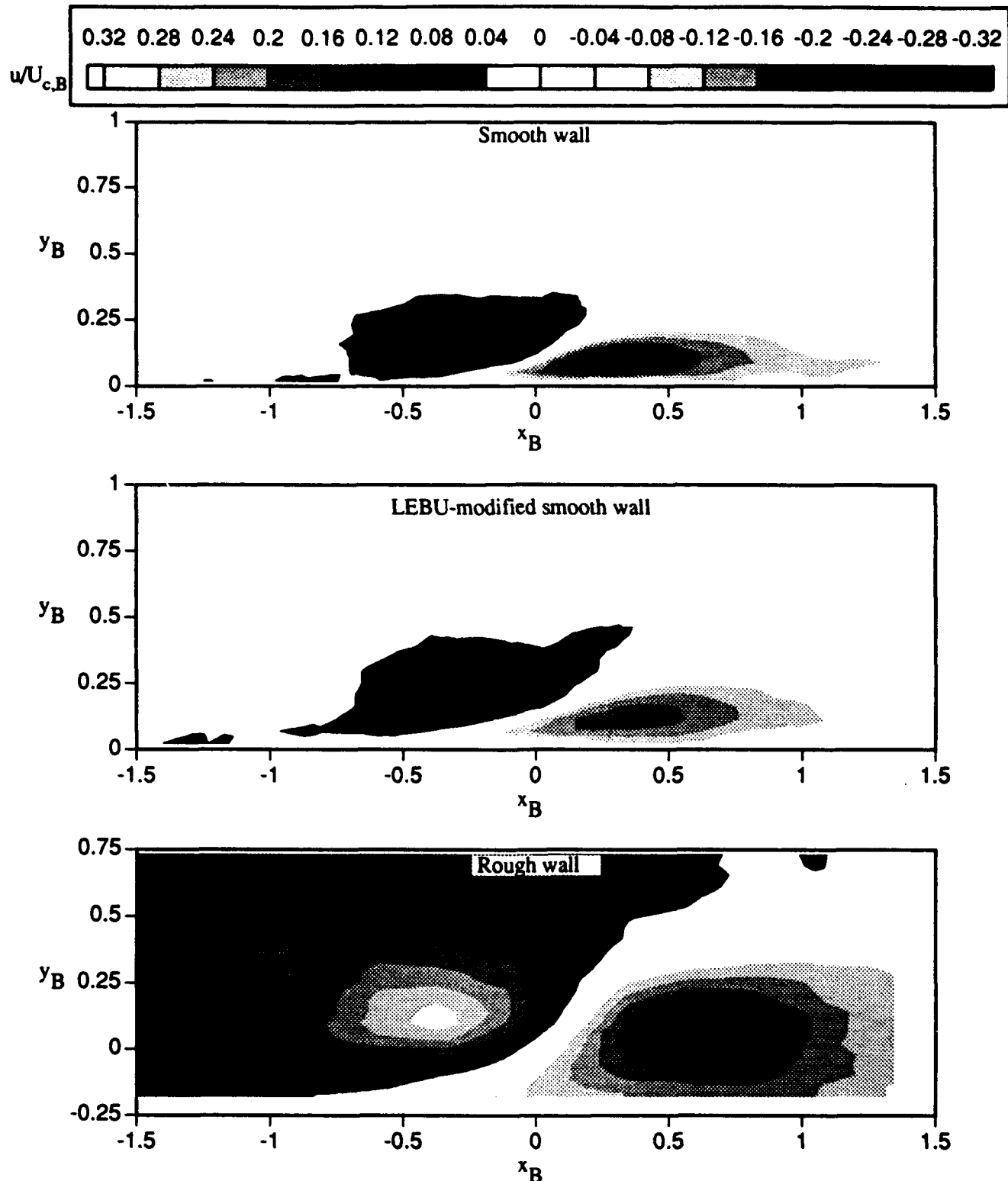
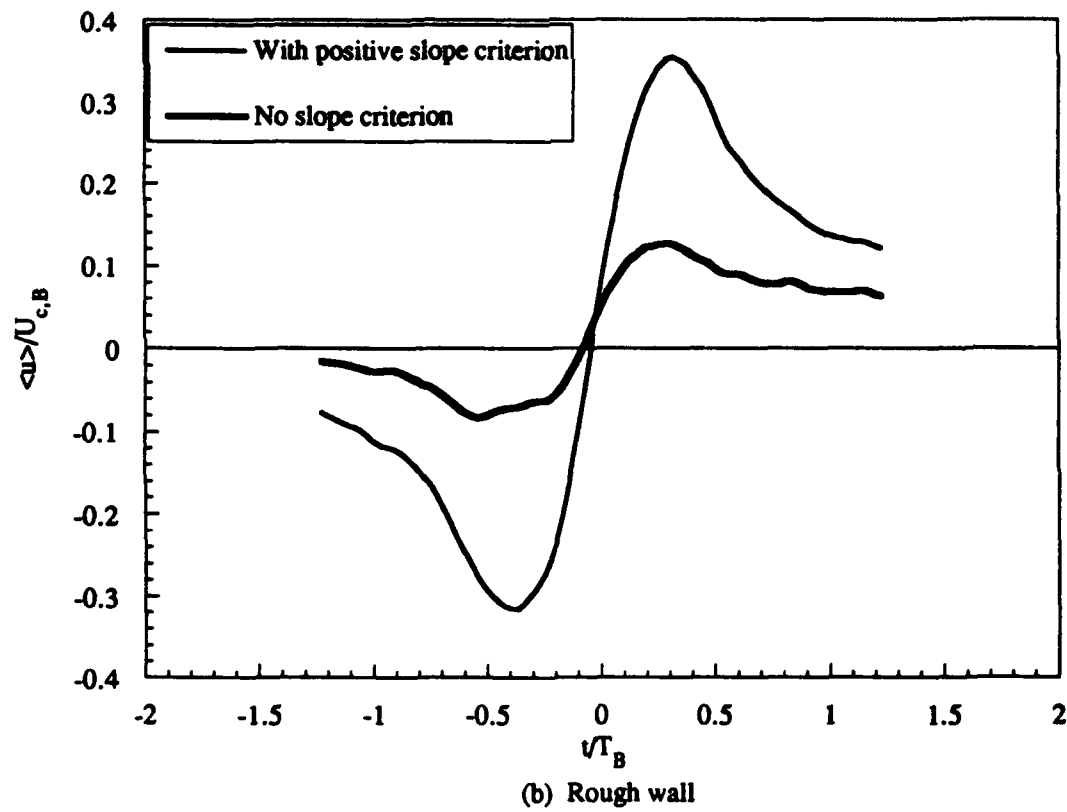
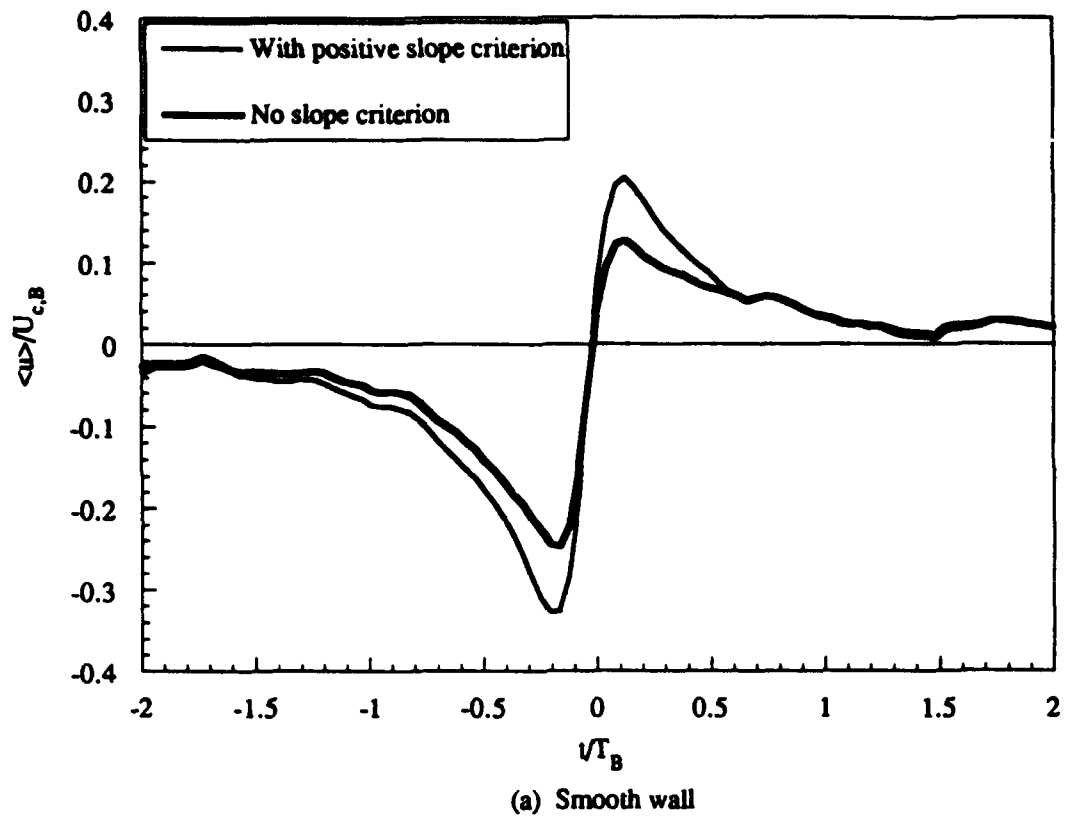


Figure 30 Ensemble averaged conditional samples of  $u$  velocity contours of the VITA shear layer over a smooth wall with and without the LEBU device, and over a rough wall. Length scales normalized by the length of the burst. Contour levels normalized by the burst convection velocity.



**Figure 31** Comparison of the ensemble averaged conditional samples of shear layer events for the (a) smooth wall and (b) rough wall, detected with and without a positive slope criterion.

## **Appendix A**

**Detection of Coherent Structures in Smooth and Rough Wall Turbulent  
Boundary Layer Flows Using a Scanning LDV System**

**DETECTION OF COHERENT STRUCTURES IN SMOOTH AND  
ROUGH WALL TURBULENT BOUNDARY LAYER FLOWS  
USING A SCANNING LDV SYSTEM**

**by**

**ATUL KOHLI, B.S.**

**THESIS**

**Presented to the Faculty of the Graduate School of  
The University of Texas at Austin  
in Partial Fulfillment  
of the Requirements  
for the Degree of**

**MASTER OF SCIENCE IN ENGINEERING**

**THE UNIVERSITY OF TEXAS AT AUSTIN**

**May 1992**

## ACKNOWLEDGEMENTS

I would like to thank Dr. David Bogard for his constant encouragement and guidance throughout this project. His helpful advice and support made this possible. I would also like to thank Dr. Kenneth Ball for his very prompt review and comments. This project was sponsored by the Office of Naval Research.

John Spurgeon of the M.E. Electronics shop deserves special mention for rescuing me every time I ran into problems with the instrumentation in the lab.

I would like to thank Choon Gan for writing the data acquisition program which made things much easier, and for helping me learn about LDV's. All the graduate students in the TTCRL lab: Don Schmidt, Karen Thole, Janine Whan-Tong, Scott Ellis, Choon Gan, Jason Blitz, Basav Sen, Sriram Neelakantan, and Tzong-Huei Chen, deserve a big thank you for maintaining a very warm and friendly work environment. They were always willing to help and it was fun working with them. I would like to thank Don Schmidt and Scott Ellis for their helpful comments during our lunch-time discussions. Finally, I would like to thank my family for their understanding and support.

Atul Kohli

May 1992

## ABSTRACT

### DETECTION OF COHERENT STRUCTURES IN SMOOTH AND ROUGH WALL TURBULENT BOUNDARY LAYER FLOWS USING A SCANNING LDV SYSTEM

by

ATUL KOHLI, B.S.

SUPERVISING PROFESSOR: DR. DAVID G. BOGARD

The goal of this study was to determine the spatial description of coherent structures, namely the bursts and sweeps, in smooth and rough wall turbulent boundary layer flows for improved understanding of their interaction. Single component velocity measurements were made in a water channel using a rapid scanning LDV system, which provides a sequence of essentially instantaneous velocity profiles. A conditional sampling analysis which involved grouping events based on size and distance from the wall was used to get a streamwise cross-section of the structures and the associated flow field. Compared to the smooth wall, low speed spatial events over the rough wall were bigger, and stronger events were present further away from the wall. Close to the smooth wall, high speed fluid was found on top and in front of the low speed spatial events, appearing below the low speed spatial events at higher heights. The high speed spatial events remained unaffected by the change in surface roughness and in both cases, showed low speed fluid underneath at heights closer to the wall.

## TABLE OF CONTENTS

<b>ACKNOWLEDGEMENTS</b>	<b>iv</b>
<b>ABSTRACT</b>	<b>v</b>
<b>LIST OF SYMBOLS</b>	<b>viii</b>
<b>LIST OF TABLES</b>	<b>x</b>
<b>LIST OF FIGURES</b>	<b>xi</b>
<b>CHAPTER 1. INTRODUCTION</b>	<b>1</b>
1.1 Coherent structures	1
1.2 Past research	3
1.3 Objectives	10
<b>CHAPTER 2. EXPERIMENTAL APPARATUS AND PROCEDURES</b>	<b>14</b>
2.1 Scanning LDV system	15
2.1.1 Alignment of scanner	15
2.1.2 LVDT phase lag	17
2.1.3 Operational parameters	19
2.2 Rough wall	20
2.2.1 Rough surface parameters	20
2.2.2 Friction velocity and apparent origin	21
2.3 Flow conditions	25
2.4 Data acquisition and processing	26
2.5 Spatial detection technique	27
2.5.1 Selection of threshold	29
2.5.2 Conditional sampling	31
<b>CHAPTER 3. VALIDATION OF DATA</b>	<b>44</b>
3.1 Smooth wall	44
3.1.1 Mean and rms profiles	45
3.1.2 Ejection and burst frequencies	45

3.2 Rough wall	46
3.2.1 Self preservation	46
3.2.2 Roughness regime	49
3.2.3 Mean and rms profiles	50
<b>CHAPTER 4. RESULTS AND DISCUSSION</b>	<b>61</b>
4.1 Single point detection	61
4.1.1 Single point detection for smooth wall	62
4.1.2 Single point detection for rough wall	63
4.1.3 Burst and ejection frequencies	63
4.2 Smooth wall spatial events	65
4.2.1 Low speed spatial events	66
4.2.2 High speed spatial events	68
4.3 Rough wall spatial events	70
4.3.1 Low speed spatial events	71
4.3.2 High speed spatial events	73
<b>CHAPTER 5. CONCLUSIONS</b>	<b>98</b>
5.1 Summary and conclusions	98
5.2 Recommendations for future work	101
<b>APPENDIX A. UNCERTAINTY ANALYSIS</b>	<b>103</b>
A.1 Contour levels	103
A.2 Instantaneous and mean velocity scanning measurements	103
A.3 Probe volume position	106
<b>APPENDIX B. METHOD OF GROUPING EJECTIONS INTO BURSTS</b>	<b>108</b>
<b>APPENDIX C. CALCULATION OF THE APPARENT ORIGIN</b>	<b>110</b>
<b>REFERENCES</b>	<b>112</b>
<b>VITA</b>	

## LIST OF SYMBOLS

$C_f$	Skin friction coefficient
$d$	Width of roughness element
$D$	Distance from nearest neighbour for roughness element
$e$	Apparent origin or error in origin
$H$	Shape factor
$k$	height of roughness element
LDV	Laser Doppler Velocimeter
$L_L$	Detection threshold for low speed spatial events
$L_H$	Detection threshold for high speed spatial events
LVDT	Linear Variable Differential Transformer
$Re_\theta$	Reynolds number based on momentum thickness
$Re_k$	Reynolds number based on $k$ , $u_\tau$
$T^+$	Time normalized by inner scales $v$ , $u_\tau$
$T_e$	Time between ejections
$U$	Absolute velocity in the streamwise direction
$U_b$	Convection velocity of the burst event
$U_s$	Convection velocity of the sweep event
$u$	Fluctuating velocity of $U$
$u_{rms}$	Root mean square velocity of $U$
$U_\infty$	Freestream velocity
$u_\tau$	Shear velocity

$u^+$	Fluctuating velocity normalized by inner scale $u_\tau$
$x, y, z$	Streamwise, wall-normal and spanwise coordinates
$x^+, y^+$	$x, y$ coordinates normalized by inner scales $v, u_\tau$

### Greek symbols

$\chi$	Distance from the leading edge of the rough wall
$\delta$	Boundary layer thickness ( $y$ distance where $U = 0.99 U_\infty$ )
$\delta_0$	Boundary layer thickness at leading edge of rough wall
$\delta^*$	Displacement thickness
$\kappa$	von Karman constant
$\lambda$	Roughness concentration
$\nu$	Kinematic viscosity
$\theta$	Momentum thickness
$\tau_{\max}$	Cut-off time for grouping ejections into bursts
$\xi$	Normalised distance from start of rough wall ( $\chi / \delta_0$ )

## LIST OF TABLES

2.1	Operational parameters	19
2.2	Flow conditions	26
4.1	Categories of low speed spatial events based on a range of maximum heights.	67
4.2	Categories of high speed spatial events based on a range of minimum heights.	69
4.3	Categories of low speed spatial events over rough wall based on a range of maximum heights.	71
4.4	Categories of high speed spatial events over rough wall based on a range of minimum heights.	74

## LIST OF FIGURES

1.1	'u' velocity contours of the shear layer obtained from a conditionally sampled 'mapping' probe based on a single point VITA detection at $y^+ = 15$ . (From Johansson, Alfredsson and Eckelmann, 1987.)	12
1.2	Sequence of instantaneous velocity profiles generated by image processing of hydrogen bubble flow visualization. (From Lu and Smith, 1985.)	12
1.3	Rough wall mean velocity profiles showing downward shift from the smooth wall profile with increasing roughness. (From Ligrani and Moffat, 1986.)	13
1.4	rms profiles for smooth, transitionally rough and fully rough turbulent boundary layers, normalized with $u_t$ . (From Ligrani and Moffat, 1986.)	13
2.1	Schematic diagram of the scanning LDV system.	33
2.2	Roughness geometry and parameters.	34
2.3	Schematic of water channel facility.	35
2.4	Quality of match between measured and calculated profiles.	36
2.5	Raw and bin averaged data from one instantaneous scan showing the bin averaged data following the flowfield.	37
2.6	Typical velocity scans from one dataset; time between scans is $T^+ = 2.9$ . Solid lines represent mean profile based on 26,500 scans.	38
2.7	Distribution of bin averaged data before and after interpolation at each bin height in the scan range for one data set.	39

2.8	Time records at individual bin heights from a data set, showing the ability of the scanner to resolve high frequency oscillations in the flow.	40
2.9	Variation in frequency of generation of spatial events with threshold over the rough and smooth wall.	41
2.10	Distribution of (a) low speed and (b) high speed spatial events with different threshold for the smooth wall.	42
4.3	Conditional samples of random events over the smooth and rough wall for determining the significant contour levels.	43
3.1	Comparison of H as a function of $Re_\theta$ .	52
3.2	Comparison of skin friction coefficients.	52
3.3	Scanning mean velocity profile compared to stationary measurements and Spalding's law.	53
3.4	Comparison of rms profiles.	53
3.5	Burst and ejection frequencies compared with single point measurements of Coughran (1988).	54
3.6	Defect velocity profiles at different stations to verify self preservation.	55
3.7	Streamwise development of integral parameters.	56
3.8	Comparison of skin friction results obtained by the profile matching method.	56
3.9	Half power plot of mean velocities showing the approximate location of the internal boundary layer from the knee point.	57

3.10	Variation of critical Reynolds number with the aspect ratio of roughness elements from Bandyopadhyay (1987).	58
3.11	Mean velocity profile over the rough wall from scanning measurements compared with stationary measurements over rough and smooth walls.	59
3.12	Scanning rms profile compared with stationary measurements, Grass (1971) and smooth wall profile.	60
4.1	Single point detection results at detection heights of $y^+ = 35$ and 65.	76
4.2	Single point detection at $y^+ = 66$ , from Bolton (1990) showing the presence of a significant high speed structure. Contours are in terms of fluctuating velocities normalized by the friction velocity.	77
4.3	Single point detection at $y^+ = 60$ , from Gan (1989) showing no high speed region. Contours are in terms of fluctuating velocities normalized by the friction velocity.	78
4.4	Single point detection over rough wall at $y^+ = 35$ and 65.	79
4.5	Burst and ejection frequencies over the smooth and rough wall.	80
4.6	Burst and ejection frequencies scaled with inner variables	80
4.7	Burst and ejection frequencies scaled with mixed variables	81
4.8	Burst and ejection frequencies scaled with outer variables	81
4.9	Conditional samples of low speed spatial events over the smooth wall at different height categories based on their maximum height from the wall. See Table 4.1 for details.	82

4.10	Conditional samples of high speed spatial events over the smooth wall at different height categories based on their minimum height from the wall. See Table 4.2 for details.	84
4.11	Conditional samples of low speed spatial events over the rough wall at different height categories based on their maximum height from the wall. See Table 4.3 for details.	87
4.12	Smooth and rough wall low speed spatial events at heights H2 and H3.	92
4.13	Conditional samples of high speed spatial events over the rough wall at different height categories based on their minimum height from the wall. See Table 4.4 for details.	93
B.1	Procedure of plotting time between ejections to get $\tau_{\max}$ , using the method by Barlow and Johnston (1985).	109
C.1	Plot used to determine the apparent origin by the method of Furuuya et al. (1976).	111

## **CHAPTER 1**

### **INTRODUCTION**

#### **1.1 Coherent structures**

Ever since researchers started studying the turbulent boundary layer, they have sought to understand the generation and dissipation of boundary layer turbulence at the expense of the mean motion. In the process of studying the internal structure of the boundary layer flows, the presence of quasi-periodic patterns of coherent motion or turbulence structure has been well established. These coherent motions move low speed fluid away from the wall region and high speed fluid towards the wall, leading to the enhanced transport of momentum and heat which is characteristic of the turbulent boundary layer. For this reason, the study of turbulence structure is of fundamental importance to the understanding of boundary layer dynamics.

According to Robinson (1991), a coherent motion is defined as "a three dimensional region of flow over which at least one fundamental flow variable exhibits significant correlation with itself or with another variable over a range of space and time that is significantly larger than the smallest local scales of flow." Many

coherent structures have been defined and studied by researchers. These include outward 'bursts' of low speed fluid ejecting away from the wall and in-rushing 'sweeps' carrying high speed fluid towards the wall. The majority of the Reynolds stress production in the entire boundary layer occurs in the buffer region, and is associated with these bursts and sweeps. Lu and Willmarth (1973) found that bursts accounted for 77% of the local Reynolds stress while the sweeps contributed 55%. The excess was attributed to contributions from other events. As they are important for turbulence production, bursts and sweeps are the focus of this study. Among other coherent structures reported in literature are low speed streaks, shear layers, and streamwise vortices found near the wall; and large scale turbulent bulges found in the outer region.

Although there is general agreement in turbulence literature concerning several of the kinematic issues of coherent motions, the dynamics, which includes issues of cause and effect, remain largely unsettled. This has led to experiments being conducted on non-canonical or perturbed boundary layers, with the idea that we can improve our physical understanding of the flat plate boundary layer by observing its response to different outside influences like surface roughness. Also the altered behavior of coherent structures for different perturbations will help solve the mystery about their interaction.

## 1.2 Past research

Flow visualization and single point measurements have been used extensively to study coherent structures, with numerical simulations gaining importance in recent years. Flow visualization studies give good qualitative results over a large area of the flow field, but require a lot of involved data analysis in order to get quantitative information.

Nychas, Hershey and Brodkey (1973) studied the flat plate boundary layer by suspending very small tracer particles in water and photographing their motion with a high speed camera moving with the flow. They found several discrete events: ejections, sweeps, transverse vortices, large scale accelerations and decelerations occurring randomly in space and time. They observed that typically ejections reach a height of about 100 wall units, though sometimes ejections were found at much greater heights.

Offen and Kline (1974) used a hydrogen bubble wire along with two dye injectors, one at the wall and another which could be placed anywhere in the flow, to study the relationship between the bursting of low speed streaks near the wall and the flow field farther away from the wall. They observed that most of the time a lift-up (ejection) was associated with a disturbance that moved towards the

wall (sweep). They conjectured that the disturbance was generated by the interaction of an earlier burst from further upstream with fluid motion in the logarithmic region.

Different detection techniques coupled with conditional sampling have been used by many researchers to study coherent structures. Bogard and Tiederman (1987) used simultaneous dye flow visualization and hot wire measurements to evaluate different detection schemes and found that the conditionally averaged signal always bears characteristics that can be related to the criteria used in the detection algorithm. They found that many characteristics of ejections from previous studies corresponded to different phases of the ejection event, implying that no single phase alignment method could give the overall characteristics of the event.

Blackwelder and Kaplan (1976) used conditional sampling of signals from a rake of ten hot wires covering the near-wall region up to  $y^+ = 100$ , to obtain qualitative data on the flow field associated with the shear-layer. Using a detector probe at  $y^+ = 15$ , they showed that the coherence of the detected structure extends out to about  $y^+ = 100$ . Johansson, Alfredsson and Eckelmann (1987) studied the evolution of shear-layer structures in the near-wall region, including their coherence, inclination angle, and propagation velocity. This was achieved by conditionally sampling signals, using the VITA (variable interval time averaging) detection

method, from two probes displaced in the streamwise and normal directions. The detector probe was placed at  $y^+ = 15$  and the mapping probe was traversed to various distances from the wall at different streamwise positions. Figure 1.1 shows the shear layer in terms of iso-velocity lines, normalized with the local rms level, in the x-y plane. They concluded that shear layers are formed through lift-up of low speed streaks and are confined to the near wall region.

Bolton (1990) developed a unique detection method, the spatial detection scheme, to investigate coherent structures in the near wall region using a scanning LDV. Using a convection velocity equal to the mean velocity at  $y^+ = 51$ , the velocity data was arranged such that it described the x-y plane. The detection scheme then grouped points over a significant region as an event if they satisfied the local U-level criteria. The events could be characterized by their size and maximum or minimum height. She found that conditional samples based on size and location of the low speed structures also showed significant high speed structures. A similar pattern was observed with the conditional sampling analysis of high speed structures. From the velocity contours of the spatially detected low speed event, Bolton concluded that the movement of the low speed structure away from the wall corresponded with the movement of a high speed structure towards the wall.

The above study proved that, compared to single point detection schemes, the spatial detection scheme gave a more realistic description of the relationship between high and low speed structures. A major drawback of the single point detection scheme is that it can not differentiate between events occurring at different heights. Therefore events at the detection height and parts of big events at other heights get grouped together in the ensemble average resulting in loss of resolution of the surrounding flow field. The spatial detection scheme, on the other hand, restricts events in the ensemble average to those detected at the same height, thus information about the surrounding flow field is not lost. The conditionally averaged events from single point detection schemes are always centered around the detection height, but the spatial detection scheme does not have this centering effect.

Lu and Smith (1985) used image processing of hydrogen bubble time lines to get time averaged turbulence properties. Figure 1.2 shows a sequence of instantaneous velocity profiles from their experiment. The digitizer they used had a resolution of about one wall unit. At each height they found the local velocity using time-of-flight techniques. By finding the short time variance from the fluctuating velocity data, normalized by the turbulence intensity, they reported 'bursting' activity well away from the wall. The above results were obtained by applying single point detection

schemes at various heights in the flow field. As the bubble lines gave a sequence of instantaneous velocity profiles separated by  $t^+ = 2$ , a spatial detection scheme could have been applied to the same data.

Numerical studies are limited to either Large Eddy Simulations (LES) or Direct Numerical Simulations (DNS). LES have inadequate spatial resolution of near wall features. DNS has the capability to resolve all the relevant scales but requires a lot of computer resources and is limited to low Reynolds number flows in simple geometries. Numerical results like those obtained by Spalart (1988) for low Reynolds number over a flat plate have been used to identify coherent structures that are known to exist in the laboratory boundary layers. A complete cause and effect analysis is limited at present but this should change with the advent of better analysis methods and faster computers.

There are far fewer studies of boundary layer turbulence structure over rough surfaces. Ligrani and Moffat (1986) studied structural characteristics of transitionally rough and fully rough turbulent boundary layers at different roughness Reynolds numbers over uniform spheres roughness. They found that the mean velocity profiles had well defined log regions and were shifted below the curve for the smooth wall when plotted in terms of wall units, with the shift increasing with roughness, as shown in

Figure 1.3. The turbulent intensity profiles, shown in Figure 1.4, consisted of a broad flat 'hump' rather than a sharp peak as for the smooth wall. According to them, such humps are regions where production of longitudinal turbulence energy is important. They conclude that since entrainment near a rough surface is more violent than near a smooth surface, larger amounts of low speed fluid may be pushed farther away from the wall to collide with in-rushing high speed fluid. As a result, the region of greatest mixing is moved further away from the wall and spread over a greater portion of the boundary layer.

Grass (1971) used the hydrogen bubble technique to visualize open-channel turbulent flow over smooth, transitional and rough surfaces. He found that fluid ejections and sweeps both make strong, intermittent contributions to the Reynolds stress and turbulence production, irrespective of the differences in the ejection-sweep cycle observed due to change in surface roughness. Long twisting streamwise vortices, very apparent close to the smooth boundary, were less conspicuous in the transitional and rough boundary flow where ejected fluid was seen to rise almost vertically from between the interstices of the roughness elements. The high speed inrush fluid decelerates more slowly over the smooth wall, as it is impeded mainly by viscous shear, than in the case of a rough surface, where the form drag from the roughness

elements acts as a much more effective arrest mechanism. His observations suggested that the sweep phase is significant only near the wall, whereas the ejection phase is influential through most of the boundary layer.

Nakagawa and Nezu (1977) did conditionally sampled measurements in an open-channel flow which showed that sweeps are more important than ejections in maintaining the Reynolds stress close to the rough surface. This was supported by Raupach (1981), who did quadrant analysis to investigate the events contributing to the Reynolds shear stress over regularly arrayed rough surfaces of different densities, and over a smooth surface. He found that sweeps accounted for most of the Reynolds stress close to the rough surfaces, and that the relative magnitude of the sweep component increases both with surface roughness and with proximity to the surface.

Sabot, Saleh and Comte-Bellot (1977) studied the effects of roughness on intermittent maintenance of shear stress in pipe flow. They indicate that the mean shear stress is maintained primarily by ejection events. They found that compared with smooth wall flows, ejections in rough wall pipe flows had larger mean periods of occurrence, larger mean time duration and length scale, and larger negative instantaneous shear stress peaks.

In summary, most of the studies have used either multi-probe single point measurements or flow visualization techniques to investigate bursts and sweeps. These techniques have provided information about the kinematic aspects of bursts and sweeps, but have not been able to resolve issues of interaction or cause and effect between the two. This is mainly due to loss of information about the flow field associated with the detected events which necessarily occurs with single point measurements. With numerical studies being limited to low Reynolds number flows, there is a need for an experimental technique which can preserve information about the flow field associated with the detected event. The scanning LDV measurements, along with the spatial detection scheme are expected to provide a more realistic description of these structures and their associated flow field.

### 1.3 Objectives

One of the objectives of this study was to improve the scanning LDV system to make measurements very close to the wall and reduce the uncertainty in determining the position of the probe volume while scanning. This was necessary to study bursts and sweeps which occur in the near wall region. The smooth wall boundary layer was perturbed by adding surface roughness.

Another objective was to investigate the spatial characteristics of bursts and sweeps, for the two different types of surfaces. The identifying changes in the spatial characteristics of bursts and sweeps which occur over the rough surface were expected to provide an improved understanding of the physical mechanisms which cause them. The spatial characteristics were also expected to help address the question of interaction between bursts and sweeps. This would lead to a better understanding, modelling, and control of the turbulent boundary layer.

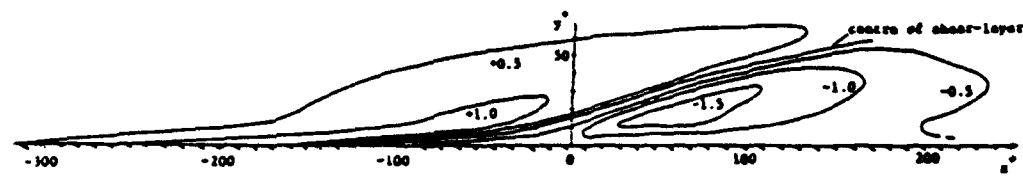


**Figure 1.1** 'u' velocity contours of the shear layer obtained from a conditionally sampled 'mapping' probe based on a single point VITA detection at  $y^+ = 15$ .  
 (From Johansson, Alfredsson and Eckelmann, 1987.)

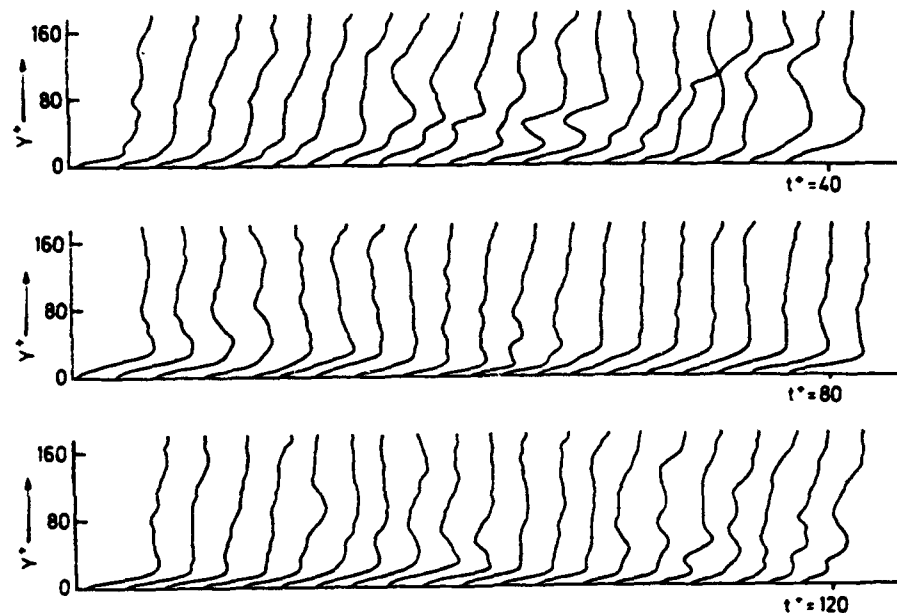


**Figure 1.2** Sequence of instantaneous velocity profiles generated by image processed hydrogen bubble flow visualization.  
 (From Lu and Smith, 1985.)

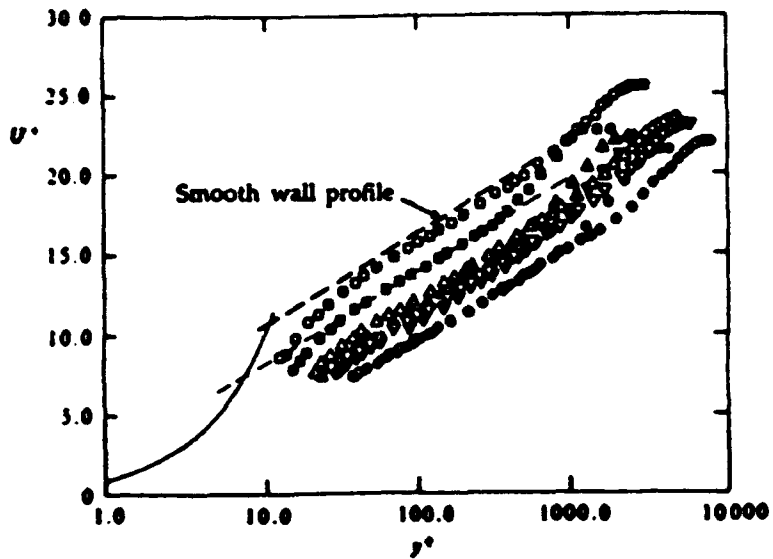


Figure 1.3 Rough wall mean velocity profiles showing downward shift from the smooth wall profile with increasing roughness. (From Ligrani and Moffat, 1986.)

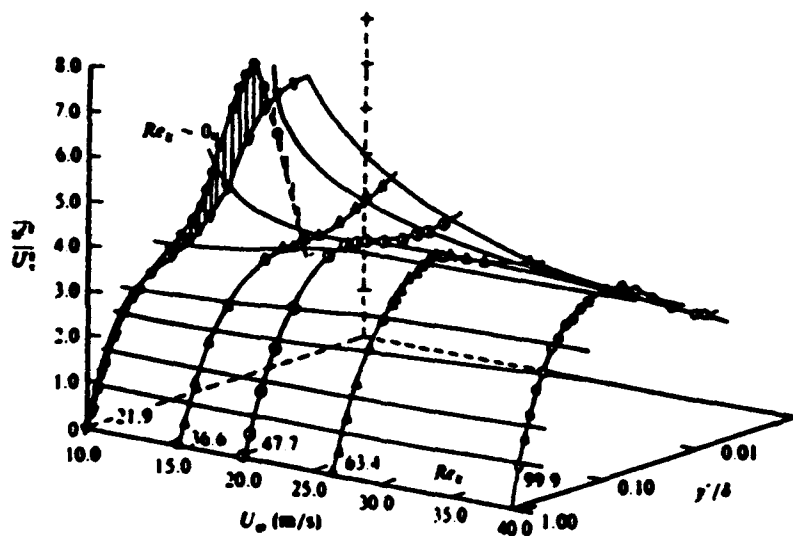


Figure 1.4 rms profiles for smooth, transitionally rough and fully rough turbulent boundary layers, normalized with  $u_\tau$ . (From Ligrani and Moffat, 1986.)

## **CHAPTER 2**

### **EXPERIMENTAL APPARATUS AND PROCEDURES**

The single component scanner used in this study was originally developed and described by Ciancarelli (1988) and Ciancarelli et al. (1988). Modifications which were made to the scanning system, in terms of a probe volume position encoder and alignment procedures, are outlined in Bolton (1990).

This chapter includes a description of the scanning LDV system, its alignment, operational parameters, and flow conditions. A description of how the phase lag between the LVDT voltage and position was reduced and accounted for to determine the position of the probe volume is presented in this chapter. Problems associated with making measurements close to the wall and their remedies are also included. The rough surface characteristics and the method of determining the friction velocity and apparent origin for the rough wall are described. The hardware for data acquisition and the procedures in data processing are outlined. The last section presents the spatial detection technique originally developed by Bolton (1990), the method of threshold selection, and conditional sampling procedures.

## 2.1 Scanning LDV system

A standard three component, back scatter LDV system, TSI model 9100-10, was modified for scanning measurements. The LDV system used a 2W argon ion laser, frequency shifter, a 3.75X beam expander, a 450 mm focussing lens and a TSI 1990 counter signal processor. A stationary mirror at 45° coupled with an oscillating mirror were added to the system. The movement of the oscillating mirror was controlled by a stepper motor, Compumotor M106-178 with a PC-21 indexer and an IBM AT computer host. The oscillating mirror traversed the probe volume rapidly in a shallow arc. A schematic diagram of the system is shown in Figure 2.1.

### 2.1.1 Alignment of scanner

For the scanner to give precise velocity measurements the axis of rotation of the oscillating mirror has to be in the plane of the laser beams. As moving the oscillating mirror was difficult, correct alignment was achieved by translating and rotating the stationary mirror with the help of two micrometers. Alignment was verified by looking at velocity distribution histograms recorded in low turbulence free stream flow. If the scanner is not aligned properly then a component of the scan velocity biases the actual velocity on

the upward scan, with an opposite bias on the downward scan. This bias shows up as two peaks in the velocity distribution histogram. As the alignment is improved, the two peaks move closer to each other and finally merge together to give one peak.

The above procedure, used by Bolton (1990), did not work very well near the wall as the velocity distributions had more spread due to high turbulence levels, making it difficult to identify distinct peaks. To look more closely at the misalignment, a long time record was taken and the data was put into bins of interval  $\Delta y = 1$  mm, covering the entire scan range. The mean velocity was calculated for each bin, separately for the upward and downward scans. The difference in the two mean velocities at each bin was a measure of the misalignment. Even though the scanner was misaligned it would give precise mean velocities as the bias would cancel out while averaging, but the turbulence intensity would be very high because of two distinctly different mean velocities for the upward and downward scans. The micrometers were used to move the stationary mirror until this difference was minimal.

After the scanner was aligned correctly, the next step was to get measurements as close to the wall as possible. The bottom wall was painted with flat black paint to reduce glare from reflections. Black tape was used to block the beams at the edges of the scan range, forming a scan window within which measurements were

made. If the two beams crossed at the bottom wall during scanning, the photo-multiplier tube was saturated, resulting in a low data rate. The signal on the oscilloscope, triggered using the LVDT voltage output, became distorted due to high noise levels when this happened. The scan window was adjusted so that the beams did not cross at the bottom wall by monitoring the signal on the scope and the data rate.

The uncertainty associated with velocity measurements was determined by scanning the free stream. The scanner measured a turbulence intensity of 1.6%, which was higher than the actual value of 0.5% determined by Coughran (1988). This high value was a result of both scanning and signal processing uncertainties. Pythagorean summation was used to calculate the uncertainty due to scanning, resulting in an uncertainty of 3% for the velocity measurements. Details of this calculation are given in Appendix A.

### 2.1.2 LVDT phase lag

The LVDT, Schaevitz Model 500HR, used as a position encoder, gave an output voltage which was proportional to the displacement of its primary coil within the core. An amplifier, Schaevitz ATA-101, was used along with the LVDT to amplify and rectify the alternating voltage for a steady output. The rectification

circuit was comprised of a bank of capacitors which caused a phase lag between the position of the primary coil and its corresponding voltage output, because of the high frequency at which the primary coil was oscillated. As a result of this, the voltage measured at the same height while stationary was different from that measured while scanning.

The excitation frequency for the LVDT, as shipped from the factory, was set at 2.5 kHz. A 10 kHz frequency plug-in module, supplied by the manufacturer, was used in its place. This should reduce the phase lag because the impedance of the capacitors in the circuit decreases at the higher excitation frequency. This was verified by measuring the phase lag with both frequency modules. It was found that the phase lag for the 10 kHz module was reduced to a third of what it was with the 2.5 kHz module.

The phase lag, though smaller now, still caused large errors in the positioning of the probe volume ( $5 - 10 y^+$ ). To incorporate the phase lag into the measurements, it was necessary to do a dynamic calibration for the LVDT. This was done by placing a hot wire in the path of the probe volume at various heights and recording the output for the upward and downward scans. Straight lines were then fitted to the points for the upward and downward scans, giving a conversion equation for converting voltage to height for each case. The uncertainty involved in positioning the probe

volume was estimated to be  $\pm 0.2$  mm. The procedure is outlined in Appendix A.

### 2.1.3 Operational parameters

To get good spatial resolution from the scanner it was required to scan at a very fast rate to give essentially an instantaneous profile. The scans have to be over a range large enough to follow the development of the structures with the data rate high enough to give good resolution. The operational parameters for both the smooth wall and the rough wall experiments are shown in Table 2.1.

Table 2.1 Operational parameters

<u>Parameter</u>	<u>Smooth wall</u>	<u>Rough wall</u>
Scan velocity	1.5 m/s (7.8 $U_\infty$ )	1.5 m/s
Scan frequency	28 scans/s	28 scans/s
Scan range	2.3 cm (230 $y^+$ )	2.7 cm (370 $y^+$ )
Time for one scan	17 msec (1.3 $T^+$ )	20 msec (3.6 $T^+$ )
Time between scans	37 msec (2.9 $T^+$ )	37 msec (6.5 $T^+$ )
Average data rate	40 points/scan	50 points/scan
Velocity uncertainty	$\pm 3\%$	$\pm 3\%$
Total data acquired	26,500 scans	25,000 scans
Total time	950 seconds	915 seconds

## 2.2 Rough wall

The aim of this study was to find out how a significant change in surface roughness changed the spatial character of bursts and sweeps. The roughness used in this study was expected to give a twofold increase in  $C_f$  compared to that of the smooth wall. The three dimensional roughness geometry used in this study is an example of the k-type of roughness. This implies that the streamwise separation between roughness elements is greater than the height of roughness elements. The d-type of roughness has a height greater than the streamwise separation.

### 2.2.1 Rough surface parameters

The rough surface consisted of cylinders, 4.5 mm high with a diameter of 9 mm and separated by 16 mm, arranged in a square array. Figure 2.2 shows dimensions of the roughness elements and defines the parameters k, d and D. This particular roughness geometry had a concentration of 0.14, the concentration being defined as:

$$\text{Concentration } (\lambda) = \frac{\text{frontal area}}{(\text{separation distance})^2}$$

which for cylinders is the same as

$$\lambda = \frac{kd}{D^2}$$

The rough wall section was placed on the water channel floor using double sided tape. The total length of the rough wall was 150 cm, and measurements were taken 145 cm from its leading edge. Upstream of the rough wall, over the smooth section, the flow was fully turbulent. The position of the trip rod, length of smooth section before the rough wall, measurement location and the length of rough wall are shown in Figure 2.3.

### 2.2.2 Friction velocity and apparent origin

Finding the friction velocity for a rough wall was difficult compared to the smooth wall. For the smooth wall, the slope of the logarithmic region of the mean velocity profile is directly proportional to the friction velocity. For a rough wall, it is not possible to do this directly as the apparent origin for the velocity profile is not known.

Researchers have used different methods for calculation of the friction velocity over rough walls. The form drag method involves using pressure taps and is possible only with large roughness elements. The drag balance method requires a lot of

development to minimize or account for leakage and is more suitable for wind tunnel experiments. The momentum integral method is highly sensitive to any three dimensionality of the flow and the determination of derivatives is highly inaccurate. Another method involves measuring the Reynolds shear stress across the boundary layer and assuming that  $u_\tau^2 = -\bar{u}\bar{v}$  in the constant stress region. Reliable measurements of  $-\bar{u}\bar{v}$  are required for this method to work and this is difficult to do in regions of very high turbulence intensity near the rough wall.

In this study the friction velocity and the apparent origin were calculated using the profile matching technique. This method assumes that if the flow is fully developed then the velocity defect law describes the profile, making it applicable to both smooth and rough surfaces. Clauser (1954) described the velocity profile in the logarithmic region as

$$\frac{U_\infty - U}{U_\tau} = - \left( 5.6 \log \frac{y U_\tau}{\delta^* U_\infty} + 0.6 \right) \quad (2.1)$$

applicable in the inner region  $y^+ \geq 32.5$  and  $y u_\tau / \delta^* U_\infty \leq 0.045$ . He obtained the logarithmic form of the equation from the fact that the defect profile and the log law have a common region where they overlap. The constants were determined by fitting a curve through

experimental data. Hama (1954) described the profile in the outer layer by the empirical relationship

$$\frac{U_\infty - U}{U_\tau} = 9.6 \left( 1 - \frac{y}{0.30\delta^* U_\infty / U_\tau} \right)^2 \quad (2.2)$$

which applies in the region  $0.15 \leq y/\delta \leq 1$  for zero pressure gradient and low free stream turbulence flows.

These two equations describe the velocity profile no matter whether the wall is smooth or rough. This was verified by Bandyopadhyay (1987), who compared the drag obtained from the above equations to drag-balance measurements over both smooth and rough walls, and found good agreement. He also calculated drag using  $C_f$  from the momentum integral equation and found poor agreement with the direct drag measurements. He attributed this to the three-dimensionality in the flow field caused by the roughness elements.

Perry et al. (1987) found that the  $C_f$  predicted by the velocity-defect-law and the momentum integral method was much higher than that predicted by the measurement of  $-\bar{u}\bar{v}$ . They concluded that their X-wire measurements of  $\bar{u}\bar{v}$  were in error due to the high turbulence intensities encountered near the wall. These large errors were due to the large angles made by the velocity vectors as they approached the X-wire. By increasing the included angle of the X-wire and by using a flying hot wire, the measured  $-\bar{u}\bar{v}$  increased and

the  $C_f$  approached a value closer to that obtained from the velocity-defect-law and the momentum integral method.

In order to determine the friction velocity, the apparent origin was assumed to be at  $k/2$ , as a first estimate. The calculated velocity profiles from equations (2.1) and (2.2) which had the best fit with the measured profile determined  $u_\tau$ . The final value of the apparent origin ( $e$ ) was then obtained by a procedure outlined by Furuya et al. (1976), presented in Appendix C, using the just calculated  $u_\tau$ . The final  $u_\tau$  was calculated using the new value of ' $e$ '. Figure 2.4 shows the quality of match between the measured and calculated profiles using the profile matching method.

The value of  $u_\tau$  obtained by the above method resulted in  $C_f = 0.00796$ , and  $e = 2.35$  mm. This value of  $C_f$  was twice as much as that over the smooth wall, at the same streamwise location and free stream velocity. This twofold increase in skin friction over the rough wall confirmed the prediction based on the height of the roughness elements. The  $\bar{u}\bar{v}$  method gave a value of  $C_f = 0.0063$ , which is 20% lower than that obtained from the profile matching method. This was because of poor  $\bar{u}\bar{v}$  measurements near the wall.

The roughness Reynolds number defined as:

$$Re_k = \frac{ku_\tau}{\nu}$$

was calculated to be 65, which means the flow is in the fully rough regime as explained later in 3.2.2.

### 2.3 Flow conditions

The experiments were carried out in an open water channel facility designed to study coherent structures in a turbulent boundary layer. Design and construction of the water channel are described in Coughran (1988). The channel, which was 0.5 m wide and 5 m long, was operated at a water level of 20 cm. The boundary flow was tripped using a 3 mm cylindrical rod, 0.5 m from the contraction. For the LDV measurements the water was seeded with 1.5  $\mu\text{m}$  mean diameter silicon carbide particles. Constant temperature ( $\pm 0.1^\circ\text{C}$ ) was maintained by running cooling water through coils located in the downstream stilling tank.

For the rough wall, measurements were made at the center of the square area defined by four adjacent roughness elements. This ensured that the measurements were not dominated by one single roughness element. This measurement location allowed an unobstructed path for the beams while scanning below the height of the roughness elements. Also the glare associated with reflections from beams hitting other roughness elements while scanning was minimal at this location. Measurements were made to check that the profile did not depend on the position with respect to the roughness elements. Parameters describing the flow conditions for the smooth and rough wall are in Table 2.2.

**Table 2.2 Flow conditions**

<u>Parameter</u>	<u>Smooth wall</u>	<u>Rough wall</u>
$U_\infty$	0.192 m/s	0.196 m/s
x	3.0 m	3.0 m
$Re_\theta$	$1718 (U_\infty \theta / v)$	$2229 (U_\infty \theta / v)$
v	$0.825 \times 10^{-6} \text{ m}^2/\text{s}$	$0.8639 \times 10^{-6} \text{ m}^2/\text{s}$
$\theta$	0.738 cm	0.98 cm
$u_t$	0.842 cm/s	1.24 cm/s
$C_f$	0.00385	0.00796

#### 2.4 Data acquisition and processing

Synchronous velocity and position data were acquired using a Macintosh II computer. The velocity data were acquired using a digital input board, National Instruments model NB-DIO-32F. The position data, in the form of a voltage output from the LVDT, were acquired by a analog-to-digital board, National Instruments model NB-MIO-16X. The analog-to-digital board and the digital board were synchronized to within 100  $\mu\text{s}$  of each other. Data acquisition was triggered by a data ready pulse from the TSI counter whenever valid Doppler bursts were measured.

Data was acquired in files which had velocity and position information for 73,728 measurements, each file corresponding to a

time record of about 60 seconds. The raw data, being randomly distributed was grouped into bins with  $\Delta y^+ = 10$ . Multiple measurements in a bin were averaged and linear interpolation was done to get data in bins where there was no data, if adjacent data was available. Figure 2.5 shows both the raw and the bin averaged data from a typical scan before interpolation for the smooth wall.

Further data analysis and conditional sampling was done using the bin averaged data. Figure 2.6 shows twenty typical bin averaged scans along with the mean velocity profile based on about 26,500 scans over the smooth wall. Linear interpolation between bins improved the availability of data in the scan range as shown in Figure 2.7, where data is available almost always for  $y^+ > 35$ . The scanner was able to resolve the high frequency variations in the velocity as is clear from the time record at each bin location from a data set, shown in Figure 2.8. This is essential for a good spatial description of the structures in the flow. The resolution was not good at the first two bin heights because of the low data rate.

## 2.5 Spatial detection technique

In the present study, the spatial detection scheme developed by Bolton (1990) was used to detect bursts and sweeps. The spatial detection is unique because it derives information from an area of

the flow as opposed to previous studies which are point measurements. Since bursts and sweeps are regions of low and high speed fluid, this method is well suited for their detection. The detection criteria has some similarity to the U-level technique used with single point measurements by Bogard and Tiederman (1986). The U-level technique is based on the magnitude of the streamwise velocity at a given point being below or above a set threshold, in the case of bursts or sweeps, respectively. In the spatial detection scheme, a detection is said to occur when this happens over a significant region.

The scanning data was arranged in terms of velocity at bins with incremental heights of  $\Delta y^+ = 10$  for each scan, thus giving a description of the  $y$ - $t$  plane. The U-level technique was then applied simultaneously at each point, resulting in either a detection or no detection. Intrinsic to the spatial detection technique was combining these points into 'groups'. These groups then represented distinct coherent events. An algorithm combined discrete points into groups using the following criteria:

- 1) A discrete detection must be located within 2 bins of another detection in the same scan.
- 2) A discrete detection must be located within an adjacent scan at the same bin height.

Groups with just one point below or above the threshold were considered to be noise or insignificant.

### 2.5.1 Selection of threshold

A very important step in any detection scheme is the selection of threshold. As outlined in Bolton (1990), the appropriate detection threshold was found by looking at the variation of frequency of the spatial events over a range of thresholds. Figures 2.9 (a) and (b) show how the frequency of low and high speed spatial events, respectively, vary with threshold over the smooth and rough wall. The frequency increases, passes through a relatively flat peak and then decreases. Bolton observed a similar variation of frequency with threshold, but had a lower frequency of events. This was due to the fact that the algorithm used by Bolton could not recognize a small event if it was close to a very big event and grouped them together. The algorithm was modified and tested to verify that it did the grouping correctly.

The variation of frequency with threshold has a plateau region where the frequency of events is relatively constant. The value of threshold at the middle of the plateau region was selected to be the detection threshold. A slightly higher or lower threshold would have caused a small change in the frequency of events. This

region of relatively constant frequency of events is an advantage the spatial detection scheme has over single point detection schemes. In single point detection schemes the frequency of events decreases monotonically with increasing threshold, making the selection of the detection threshold quite arbitrary.

For each spatial event, the number of points satisfying the detection criteria determined the size of that event. Figures 2.10 (a) and (b) show how low and high speed events of different sizes are distributed over a range of thresholds, for the smooth wall case. The events are arranged in size categories with exponentially increasing number of points in them; 2, 4, 8, 16 etc. The number of events with a size ranging from 2 to 16 points increase with increasing threshold, ones with a size of more than 64 points decrease, while the ones with 16 to 64 points are relatively unaffected by the threshold. The opposite behavior of the number of small and very big events with increasing threshold is responsible for the plateau region in frequency distribution. At any given threshold, the number of events decreased monotonically with increasing size. Similar trends were observed for the rough wall.

Bolton saw a similar trend at high thresholds, but at lower thresholds she found a greater number of very big events than medium size events. This was also due to the limitation of her

algorithm as described earlier. At the higher thresholds, her results show the same monotonic decrease because there are very few big events.

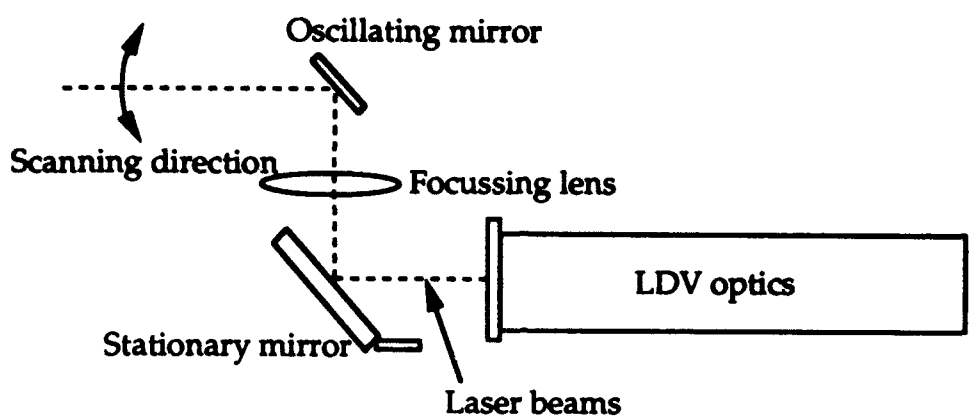
### 2.5.2 Conditional sampling

While the grouping of events was done on the y-t plane, the size, top, bottom, start, and end for each group was recorded. This allowed conditional sampling based on the size of the event and the minimum or maximum height of the event. As the bursts are known to move away from the wall, conditional sampling for low speed events was based on their maximum height. The conditional sampling for the high speed events was based on their minimum height. Ensemble averaging was done on events with maximum or minimum heights within a certain  $y^+$  range, forming a 'category'. Several such categories were formed at increasing heights from the wall. As each category was restricted to events at the same height, categories at increasing heights showed how the event changed with distance from the wall. In all the conditional sampling analyses done in this study the events were phase aligned on the leading edge.

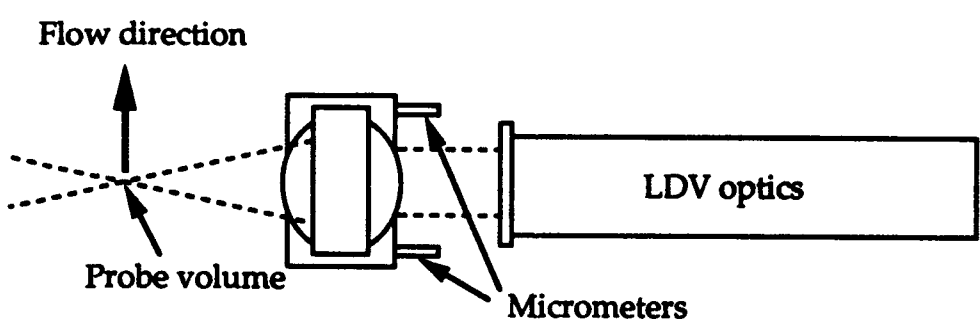
As the data available was in the y-t plane, to look at it in a spatial sense required converting it to the x-y plane. This

conversion was done using an appropriate convection velocity. Gan and Bogard (1991) found that bursts and sweeps have distinctly different convection velocities, but these are constant over a wide range ( $35 < y^+ < 100$ ). They found that the convection velocity for the bursts,  $U_b^+$ , was  $U_b^+ = 14$  and that for the sweeps,  $U_s^+$ , was  $U_s^+ = 16$ . An average value of 15 was used for both bursts and sweeps in this study, as using different convection velocities for each had little effect on the structures and their relative position. This convection velocity is equal to the local mean at  $y^+ = 60$  for a smooth wall. Over the rough wall, the mean velocity at the same height was used for the convection velocity.

Conditionally sampled results are presented in terms of the normalized fluctuating velocity, i.e.  $u/u_\tau$ , in the x-y plane. In order to determine the significant contour levels in the resulting distribution, ensemble averages were taken of random events. Figure 2.11 shows three such cases for the smooth and rough wall. Approximately the same number of events were used in these averages as in the different categories. There are no significant structures, i.e. structures where  $|u/u_\tau| > 0.3$ ; therefore, any contour level greater than  $|0.3|$  would be significant. All results are presented in this study are in terms of contour levels greater than  $|0.3|$  and in intervals of 0.3, except the single point results which are in intervals of 0.6.

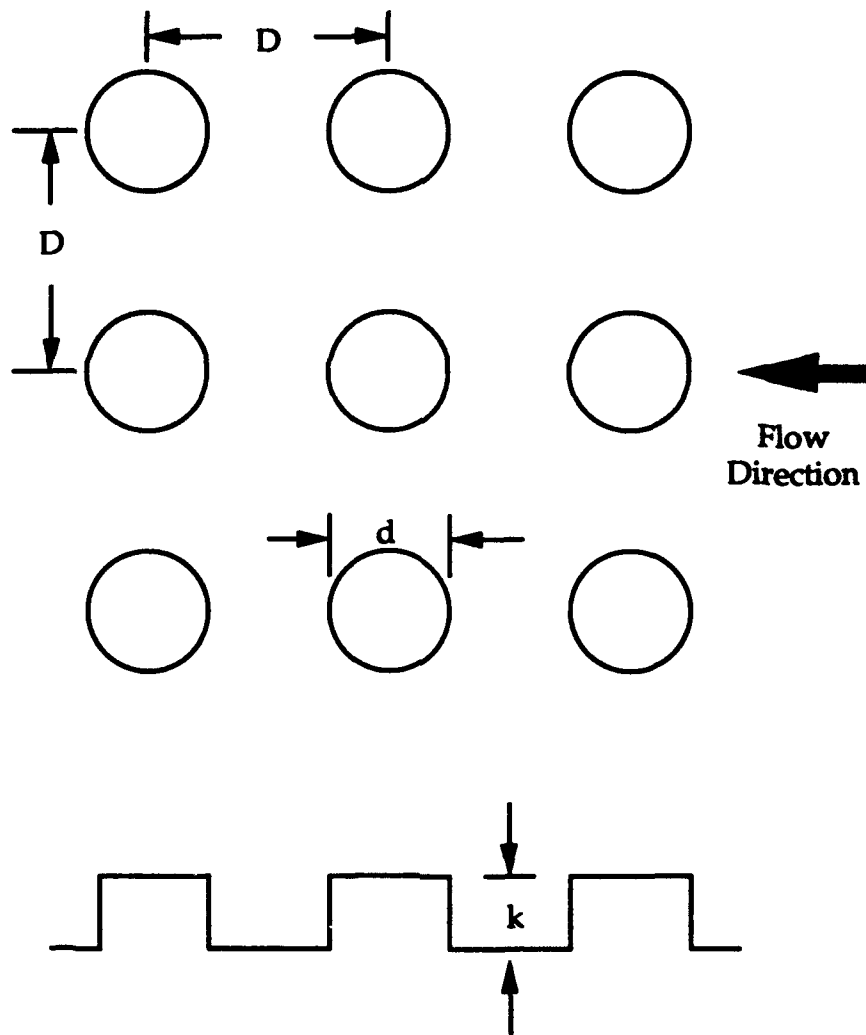


SIDE VIEW



TOP VIEW

Figure 2.1 Schematic diagram of the scanning LDV system



Height of roughness element,  $k = 4.5 \text{ mm}$   
Diameter of roughness element,  $d = 9 \text{ mm}$   
Distance from nearest neighbour,  $D = 16 \text{ mm}$

Figure 2.2 Roughness geometry and parameters

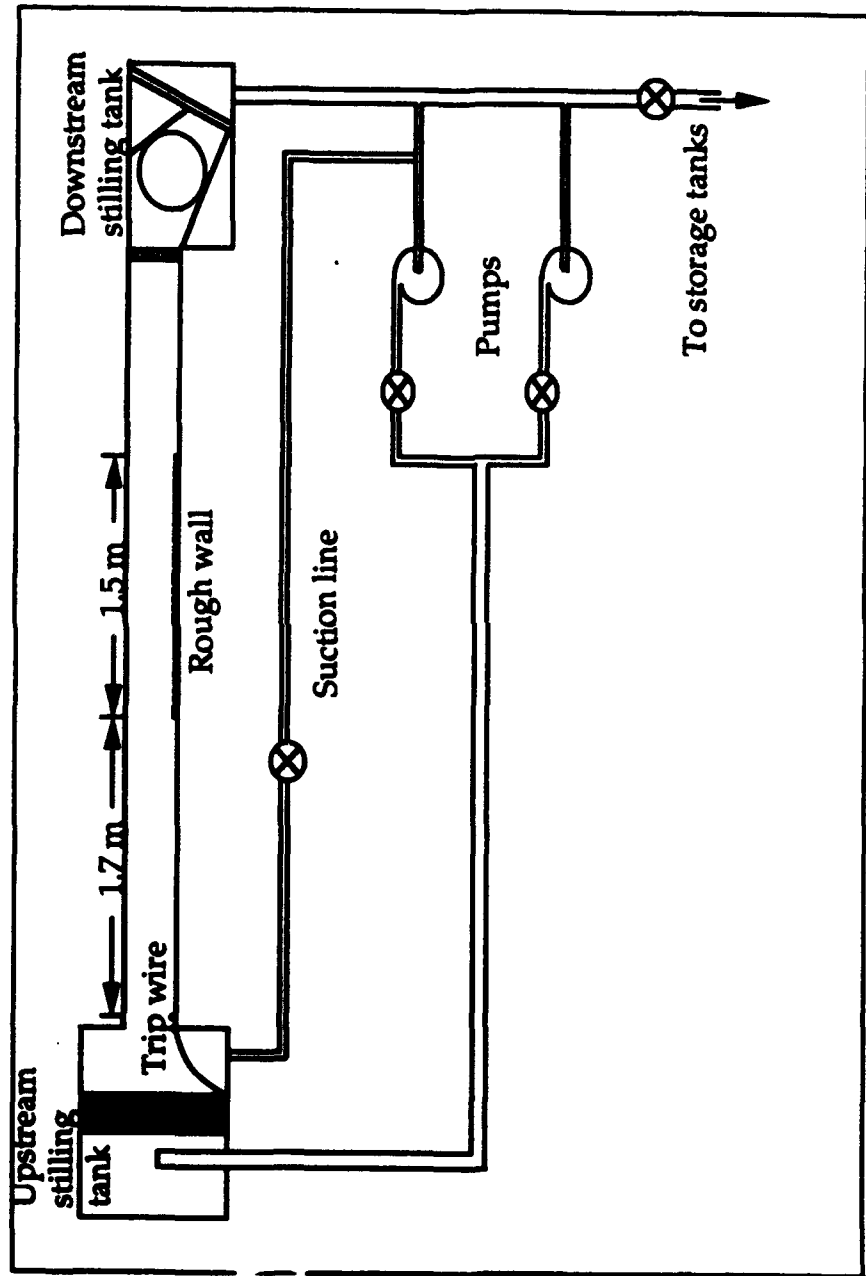


Figure 2.3 Schematic of water channel facility

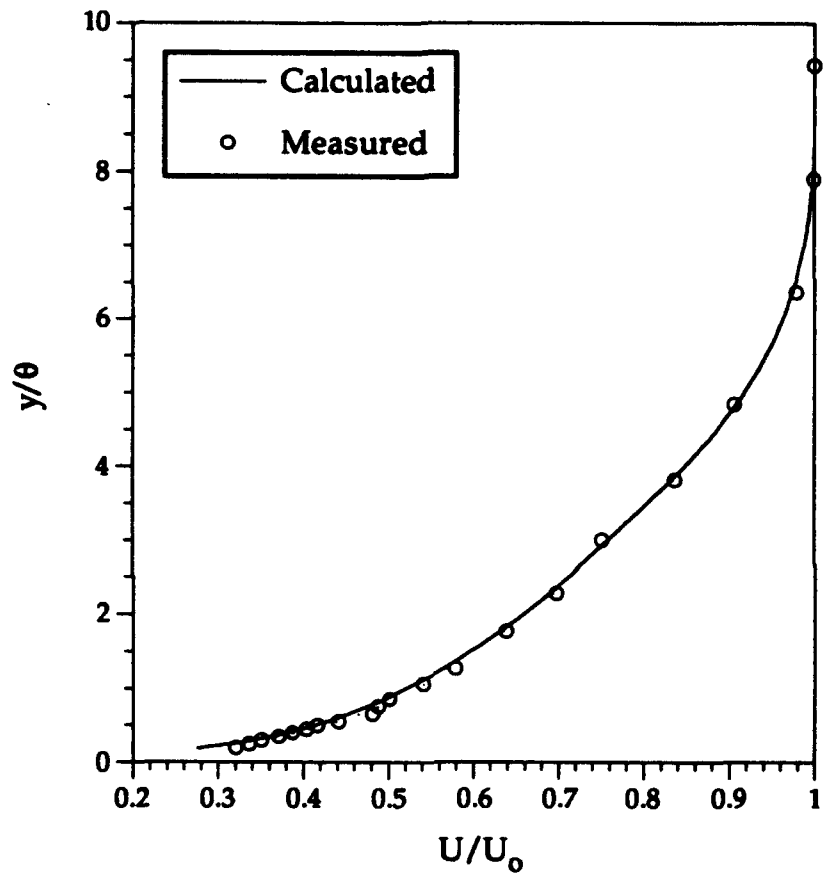


Figure 2.4 Quality of match between measured and calculated profiles

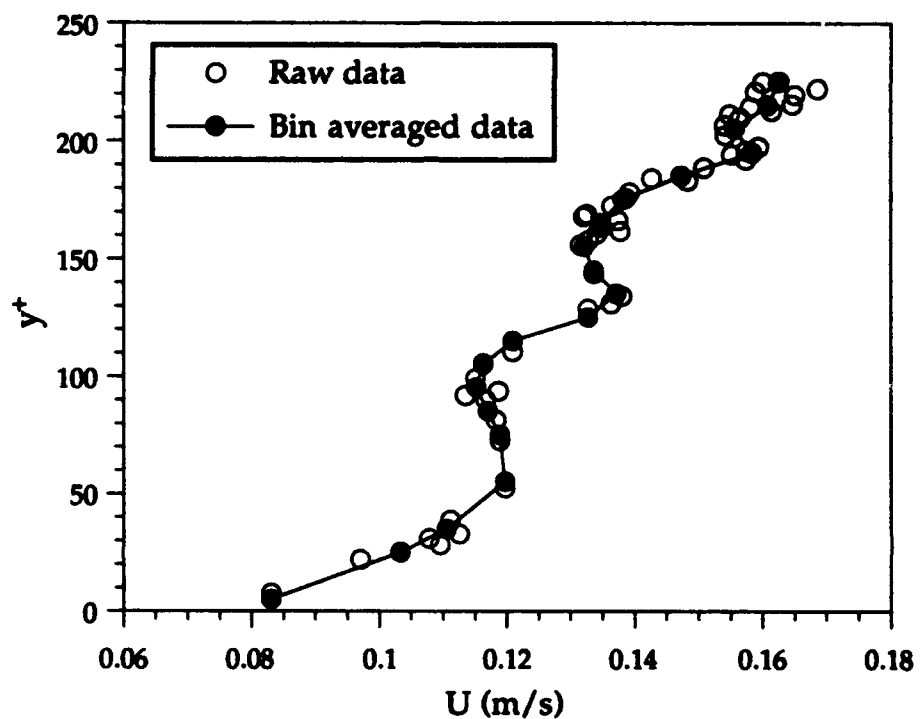


Figure 2.5 Raw and bin averaged data from one instantaneous scan showing the bin averaged data following the flow field.

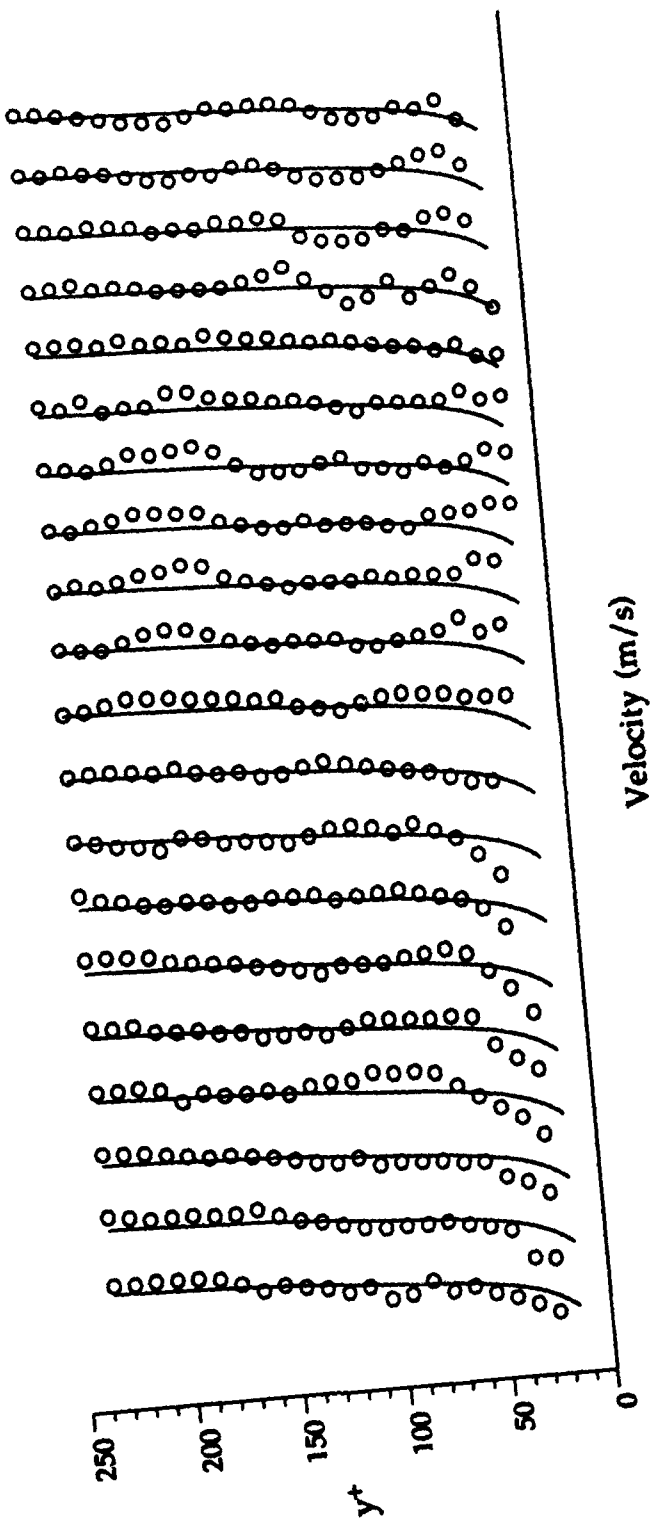


Figure 2.6 Typical velocity scans from one data set; time between scans is  $T^+ = 2.9$ .  
Solid lines represent mean profile based on 26,500 scans.

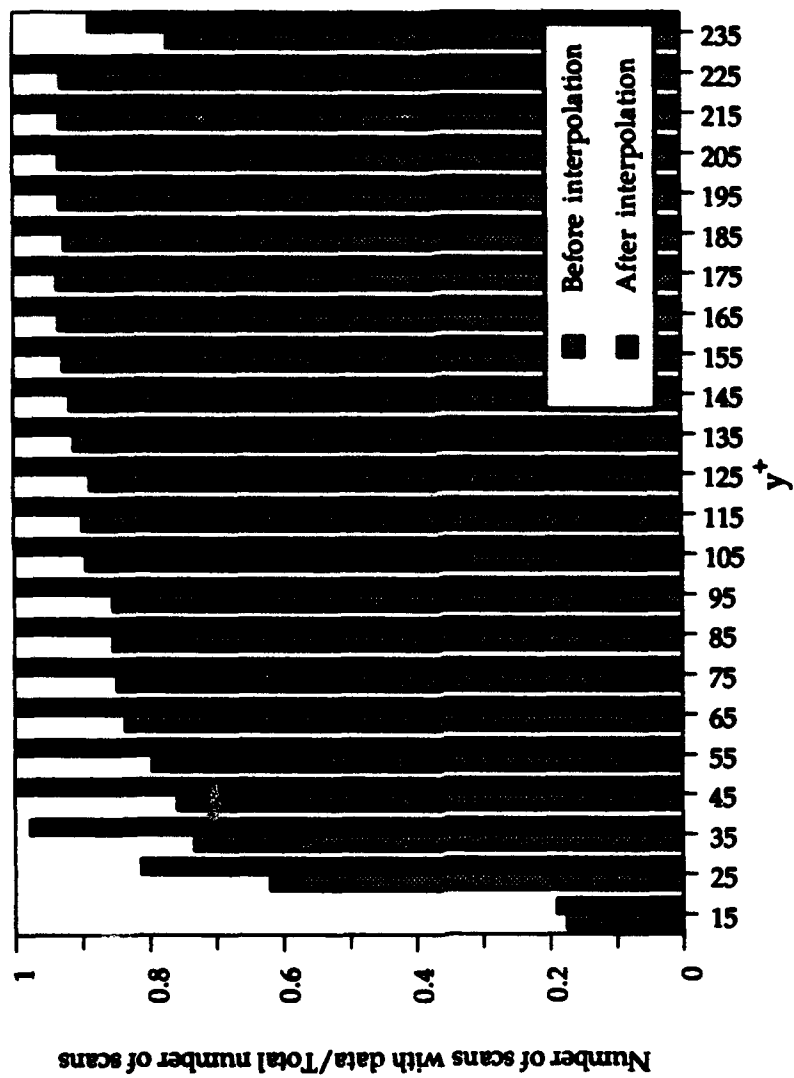
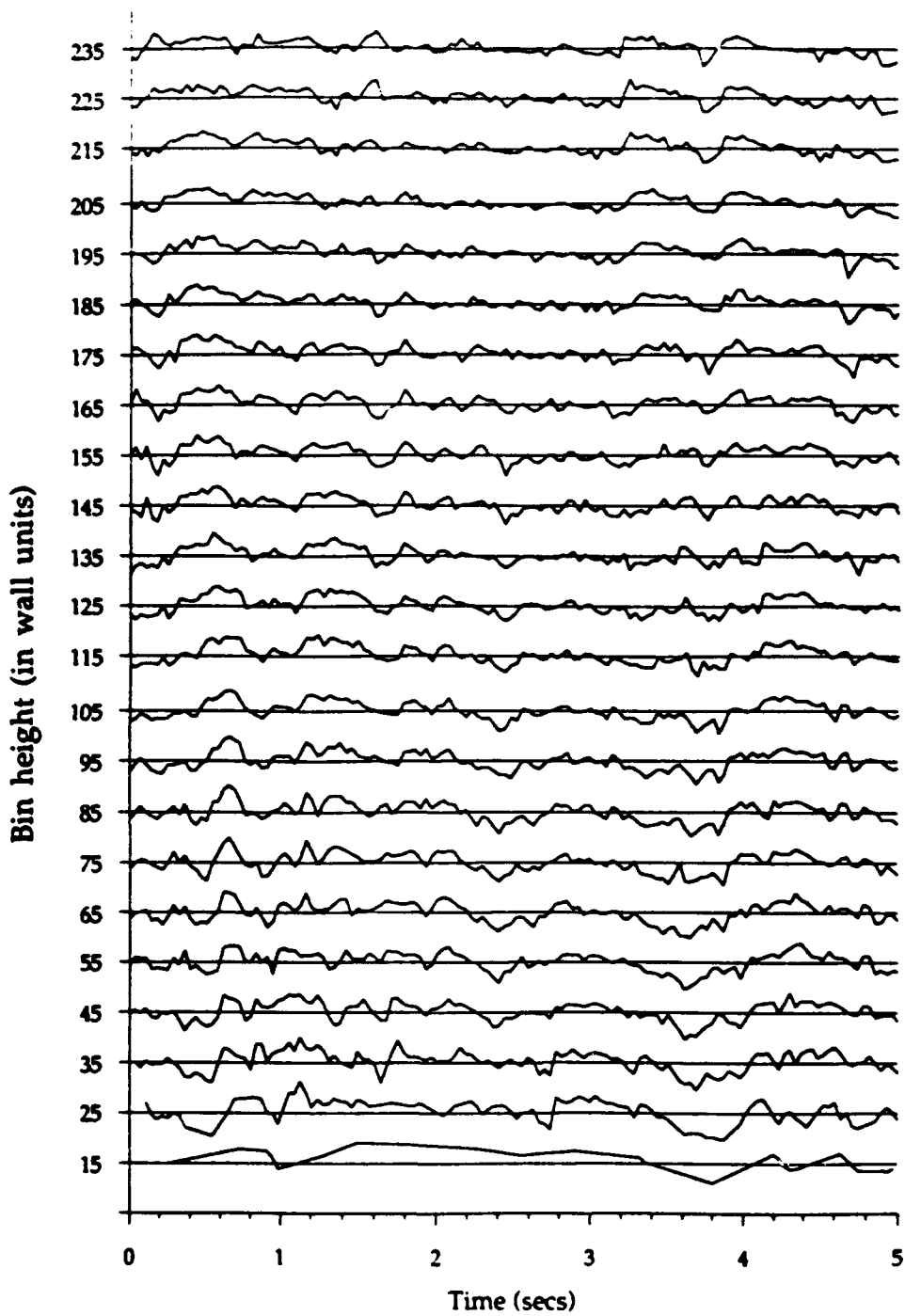
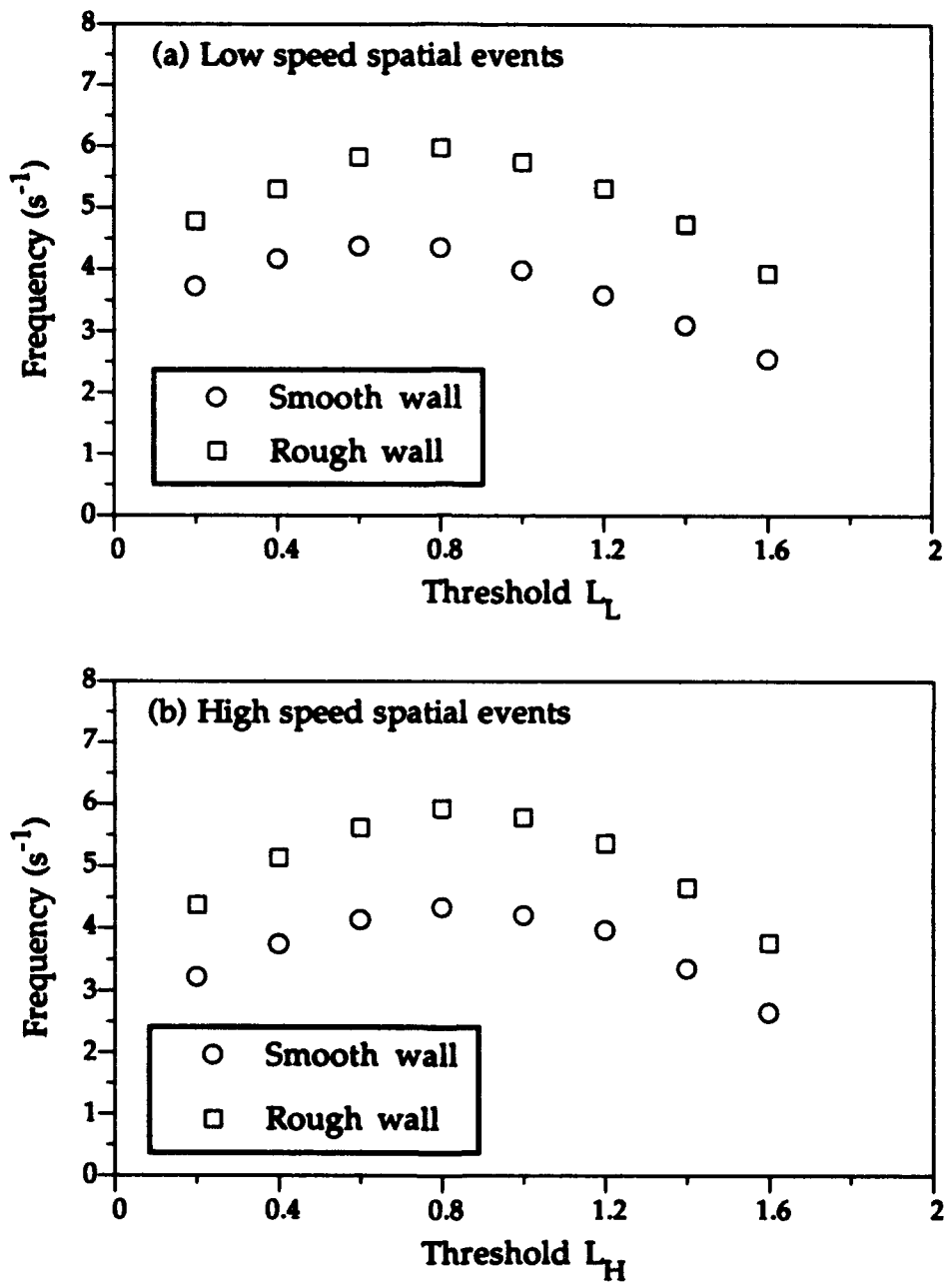


Figure 2.7 Distribution of bin averaged data before and after interpolation at each bin height in the scan range for one dataset.



**Figure 2.8** Time records at individual bin heights from a data set, showing the ability of the scanner to resolve high frequency oscillations in the flow.



**Figure 2.9** Variation in frequency of generation of spatial events with threshold over the rough and smooth wall.

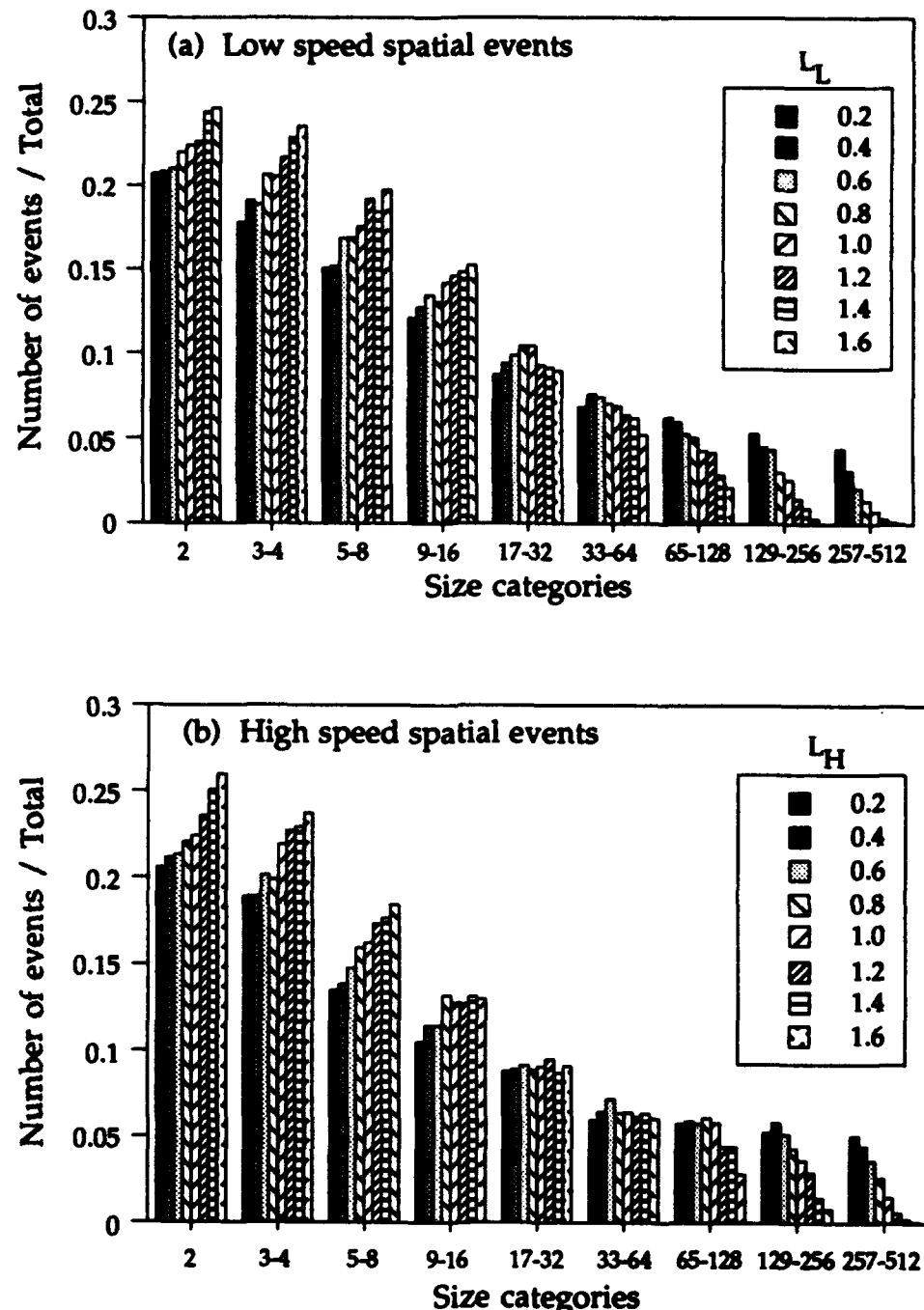


Figure 2.10 Distribution of (a) low speed and (b) high speed spatial events with different threshold for the smooth wall.

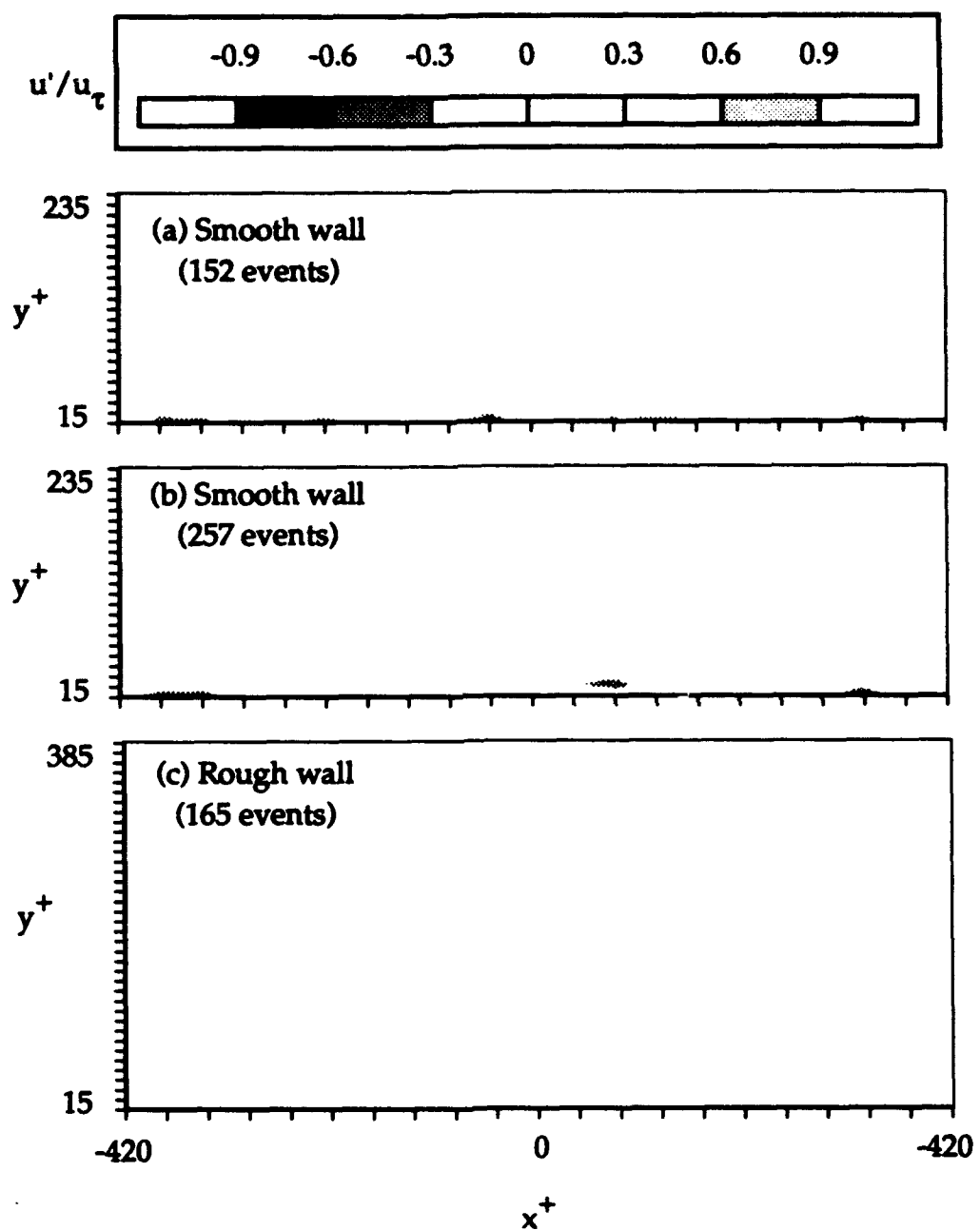


Figure 2.11 Conditional samples of random events over the smooth and rough wall for determining the significant contour levels.

## CHAPTER 3

### VALIDATION OF DATA

Stationary measurements were made to verify the existence of a standard turbulent boundary layer. Scanning data were then compared with stationary measurements and results in the literature, in terms of mean velocity, turbulence intensity profiles, burst and ejection frequencies, and skin friction coefficient. For the rough wall, stationary measurements were made to verify self preservation of the mean velocity field.

#### 3.1 Smooth wall

Stationary measurements of the mean velocity profile were made to verify the existence of a standard turbulent boundary layer. A Clauser fit was done to obtain  $u_\tau$  from the log law:

$$\frac{u}{u_\tau} = \frac{1}{\kappa} \ln \frac{yu_\tau}{v} + \beta \quad (3.1)$$

where  $\kappa = 0.41$  and  $\beta = 5.0$ . The shape factor,  $H$  calculated from the mean profile agreed well with Coles and Hirst (1969), as shown in Figure 3.1. The  $C_f$  and  $Re_0$  obtained from the profile also agreed well with the prediction given in Coles and Hirst (1969), as shown

in Figure 3.2. The figure also shows data for experiments carried out earlier in the same water channel facility by Coughran (1988), Gan (1989), and Bolton (1990).

### 3.1.1 Mean and rms profiles

The scanning mean velocity profile was compared with stationary measurements and Spalding's law of the wall which is given as:

$$y^+ = u^+ + e^{-\kappa \beta} \left[ e^{\kappa u^+} - 1 - \kappa u^+ - \frac{(\kappa u^+)^2}{2} - \frac{(\kappa u^+)^3}{6} \right] \quad (3.2)$$

with  $\kappa = 0.41$  and  $\beta = 5.0$ . The scanning mean velocity profile agreed well with both the stationary and Spalding's law as shown in Figure 3.3. The rms profile shown in Figure 3.4 agreed well with the data from Gan (1989) and Purtell et al. (1981) at similar Re.

### 3.1.2 Ejection and burst frequencies

Burst and ejection frequencies were determined at each bin height across the scan range and compared to the single point measurements made by Coughran (1988) in the same water channel facility as shown in Figure 3.5. A threshold of  $1.3 * u_{rms}$  was used in

the U-level detection scheme to be consistent with the Coughran (1988) study. Ejections were grouped into bursts using the procedure of Barlow and Johnston (1985), which is outlined in Appendix B. The ejection frequencies were slightly lower than those obtained by Coughran (1988), but showed the same trend. The burst frequencies agreed well with the previous results and were about a factor of two less than the corresponding ejection frequencies. This results in approximately two ejections per burst as found by other researchers. For  $y^+ < 35$ , the frequencies are much less than expected due to the low data density in this range.

### **3.2 Rough wall**

Stationary measurements were made at various locations on the roughness strip upstream of the final measurement location to verify self preservation of the velocity field. The velocity defect parameter (G), the shape factor (H) and the skin friction are compared with literature in this section.

#### **3.2.1 Self preservation**

Antonia and Luxton (1971) found that over a rough-to-smooth step, the skin friction appears to adjust rapidly, within 3 or 4

boundary layer thicknesses, to the new rough wall boundary condition. According to Smits and Wood (1985), self preservation is established within 20 boundary layer thicknesses. Based on this prediction the measurement location was far enough downstream for self preservation. For experimental verification, six velocity profiles were taken on the rough strip upstream of the final measurement location to study the development of the flow.

Mean velocity defect profiles are plotted as in Figure 3.6 in the form  $(U_\infty - U)/u_\tau$  as a function of  $(y+e)/\Delta$ , where  $\Delta = (\delta^* U_\infty)/u_\tau$  and  $e$ , the apparent origin, is assumed to be the same for all profiles. The variable  $\xi$  in the figure is defined as:

$$\xi = \chi / \delta_0$$

where  $\chi$  is the distance from the leading edge of the rough wall and  $\delta_0$  is the boundary layer thickness at the leading edge of the rough wall. That the flow has not reached a self-preserving state at  $\xi = 3$  is clear by looking at the departure from the defect law obtained from equations (2.1) and (2.2). Since the mean velocity at  $\xi = 18$  exhibits only a slight departure from this curve, it is reasonable to assume that self-preservation of the mean flow field is attained by  $\xi = 23$ .

The profile defect parameter,

$$G = \int_0^\infty \left( \frac{U_\infty - U}{u_\tau} \right)^2 d\left( \frac{y+e}{\Delta} \right) \quad (3.3)$$

was found to be equal to 6.52 for the mean velocity profile at  $\xi = 33$ , i.e. at the location of the scanning measurement. This is in agreement with the values of  $G$  reported in literature for the universal velocity profile on a smooth or rough wall in a zero pressure gradient, which lie between  $G = 6$  and 7. This gave further proof of the existence of a standard rough wall boundary layer.

Integral quantities for the profiles, namely, the displacement thickness ( $\delta^*$ ), the momentum thickness ( $\theta$ ), and the shape factor ( $H$ ) were calculated and are shown in Figure 3.7. Both  $\delta^*$  and  $\theta$  increase linearly with streamwise distance, while  $H$  reaches a constant value. From the above definition of  $G$ , the relation between  $H$  and  $G$  can be written as:

$$H = [1 - G(C_f/2)^{1/2}]^{-1} \quad (3.4)$$

Using the  $C_f$  obtained from the profile matching technique, and the calculated  $G$  for the last station, gives a value of  $H=1.7$ . This is in good agreement with the experimentally determined values of  $H$  as shown in Figure 3.7. This also provided an indirect check on the skin friction coefficient calculation as shown in Figure 3.8 which shows good agreement between the experimentally measured quantities and the prediction based on equation (3.4).

The flow is subjected to a step change in surface roughness when it comes to the start of the rough strip. The initial disturbance is located at the wall, and the outward propagation of the

disturbance is characterized by the formation of the internal layer. The height of this layer,  $\delta_i$ , marks the outward extent of the flow which is influenced by the new boundary condition. The approximate position of the edge of the internal layer can be estimated by the position of the 'knee' point on a half power plot as shown in Figure 3.9. It is clear that by the time the flow reaches  $\xi = 23$ , the internal boundary layer has merged with the outer boundary layer.

### 3.2.2 Roughness regime

Flow over rough surfaces can be categorized as either smooth, transitionally rough or fully rough. If the wall roughness is such that it does not affect the viscous stress region, then the viscous sublayer is undisturbed and the flow is classified as smooth. When the height of roughness elements is much greater than the viscous sublayer, the flow is said to be fully rough. When the viscous sublayer is only partially altered by the presence of roughness, both bluff-body form-drag and viscosity influence the near-wall flow, and the flow is said to be transitionally rough. Each of these flow regimes are defined by the roughness Reynolds number and the aspect ratio of roughness elements as shown in Figure 3.10.

Once self preservation was established, the next step was to find out whether the flow was smooth, transitionally rough or fully rough. This was done by calculating the roughness Reynolds number for the flow, defined as  $k^+ = k u_\tau / v$ . Different values of Reynolds numbers are quoted in literature for defining the roughness regimes, most of these are from studies of sand grain roughness, which has a spanwise aspect ratio ( $l/k$ ) of about one. Bandyopadhyay (1987) studied the effect of aspect ratio on the upper and lower critical transition Reynolds numbers over grooved roughness. He found that the aspect ratio of the roughness elements greatly affects transition as shown in Figure 3.10. In the present experiment, the spanwise aspect ratio was 2 and  $k^+ = 65$ . This puts the flow in the fully rough regime.

### **3.2.3 Mean and rms profiles**

As on the smooth wall, both scanning and stationary measurements were taken on the rough wall. Figure 3.11 shows the results along with the smooth wall mean velocity profile. There is very good agreement between the scanning and stationary measurements. The mean velocity profile over the rough wall has a well defined log region and is shifted below that of the smooth

wall profile. This trend is similar to that reported in Grass (1971) and Ligrani and Moffat (1986) among others.

The rms profile over the rough wall is shown in Figure 3.12. Results from the smooth wall case and Grass (1971), who studied pebble roughness with about the same roughness Reynolds number ( $k^+ = 85$ ) as this study, are also shown in the same figure. It is clear that the profile is much flatter over the rough wall and doesn't have the sharp peak as found over the smooth wall. Also as one moves further away from the wall, there seems to be very little difference between the smooth and rough profiles.

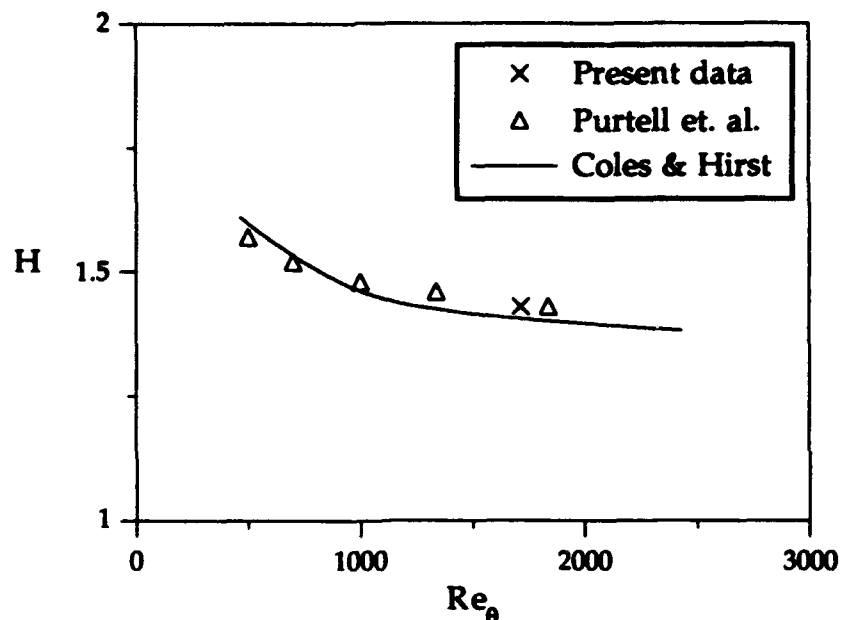


Figure 3.1 Comparison of  $H$  as a function of  $Re_\theta$

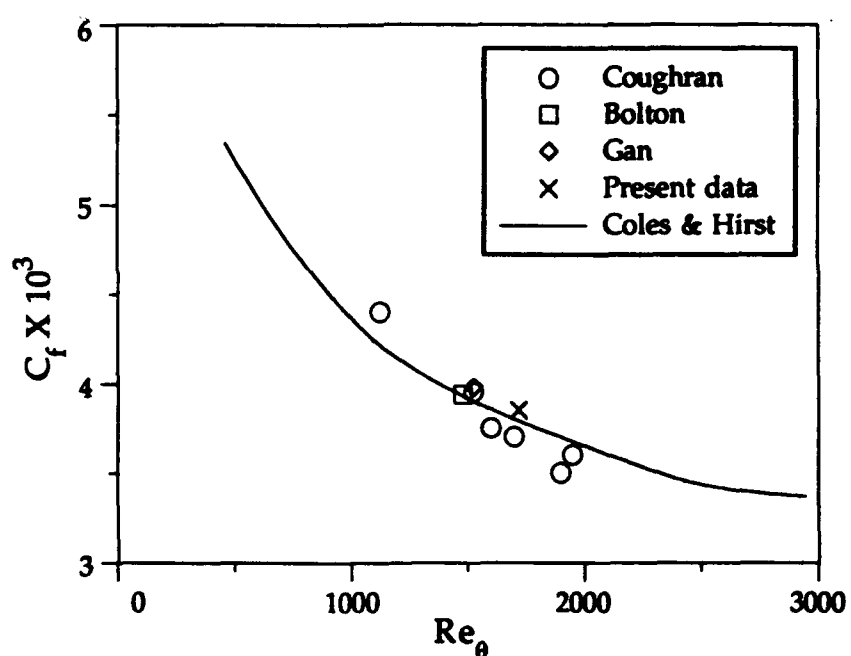


Figure 3.2 Comparison of skin friction coefficients

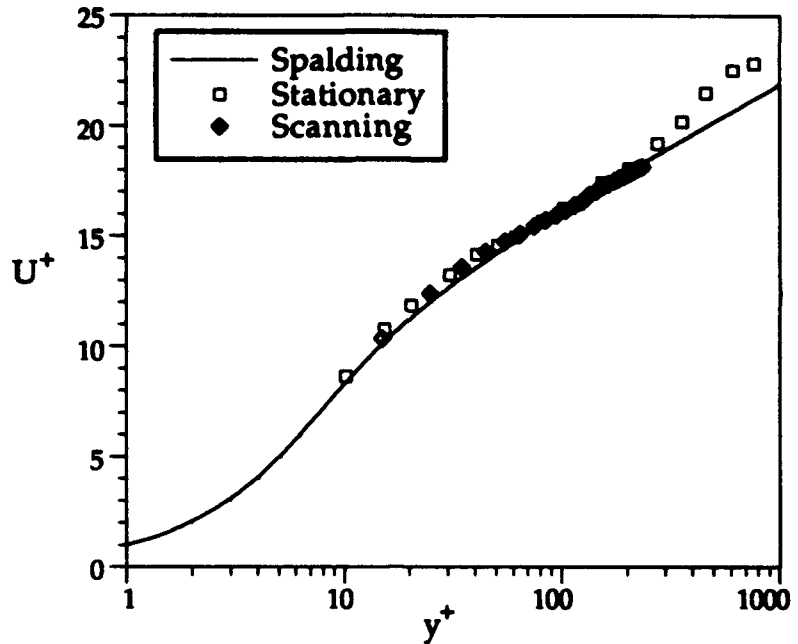


Figure 3.3 Scanning mean velocity profile compared to stationary measurements and Spalding's law

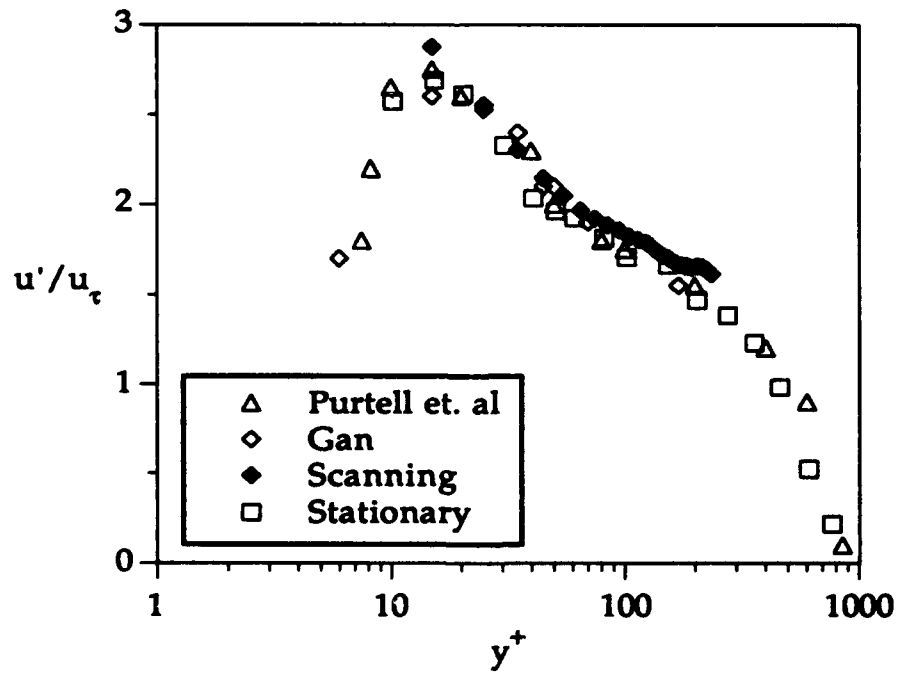


Figure 3.4 Comparison of rms profiles

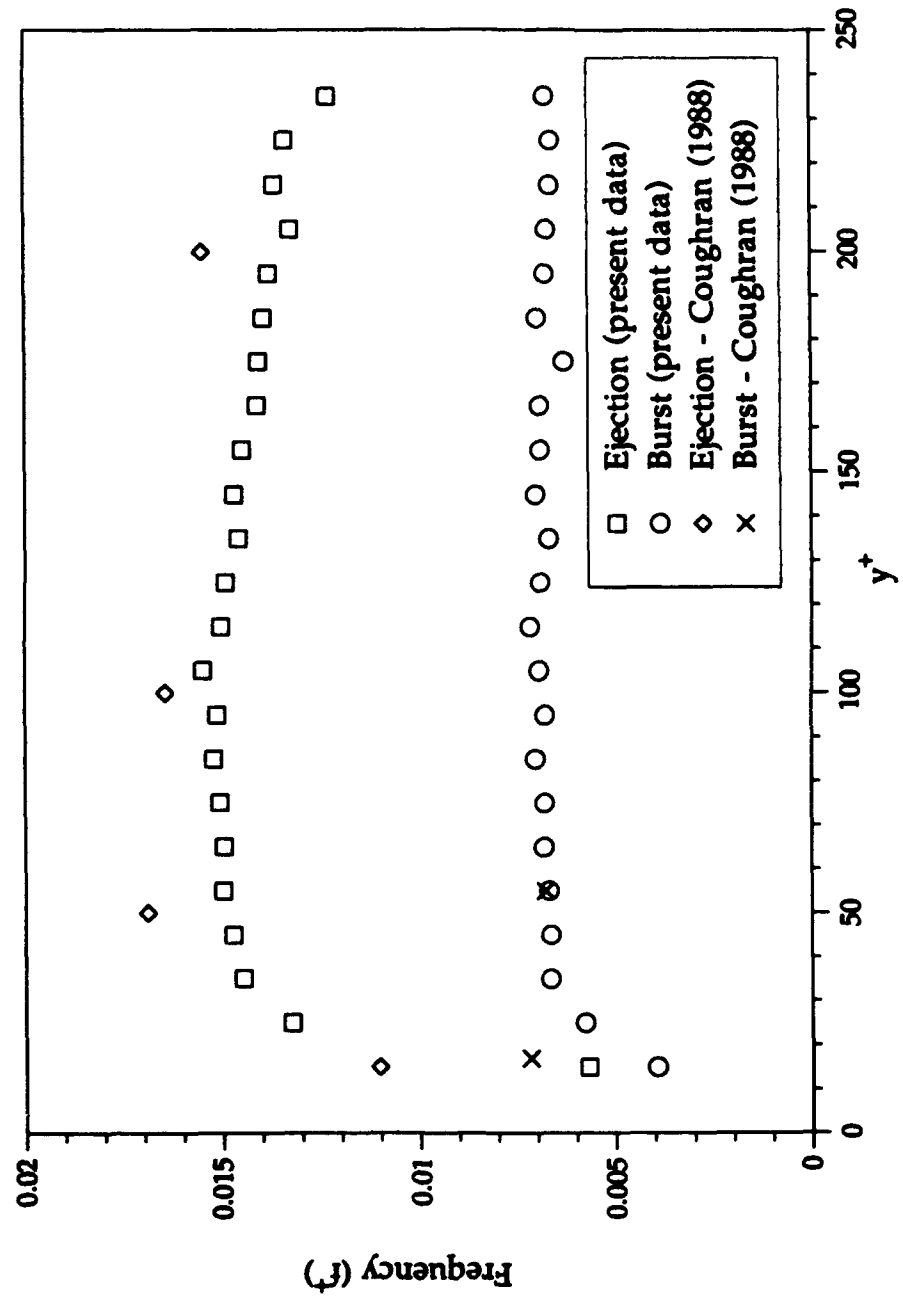


Figure 3.5 Burst and ejection frequencies compared with single point measurements of Coughran (1988)

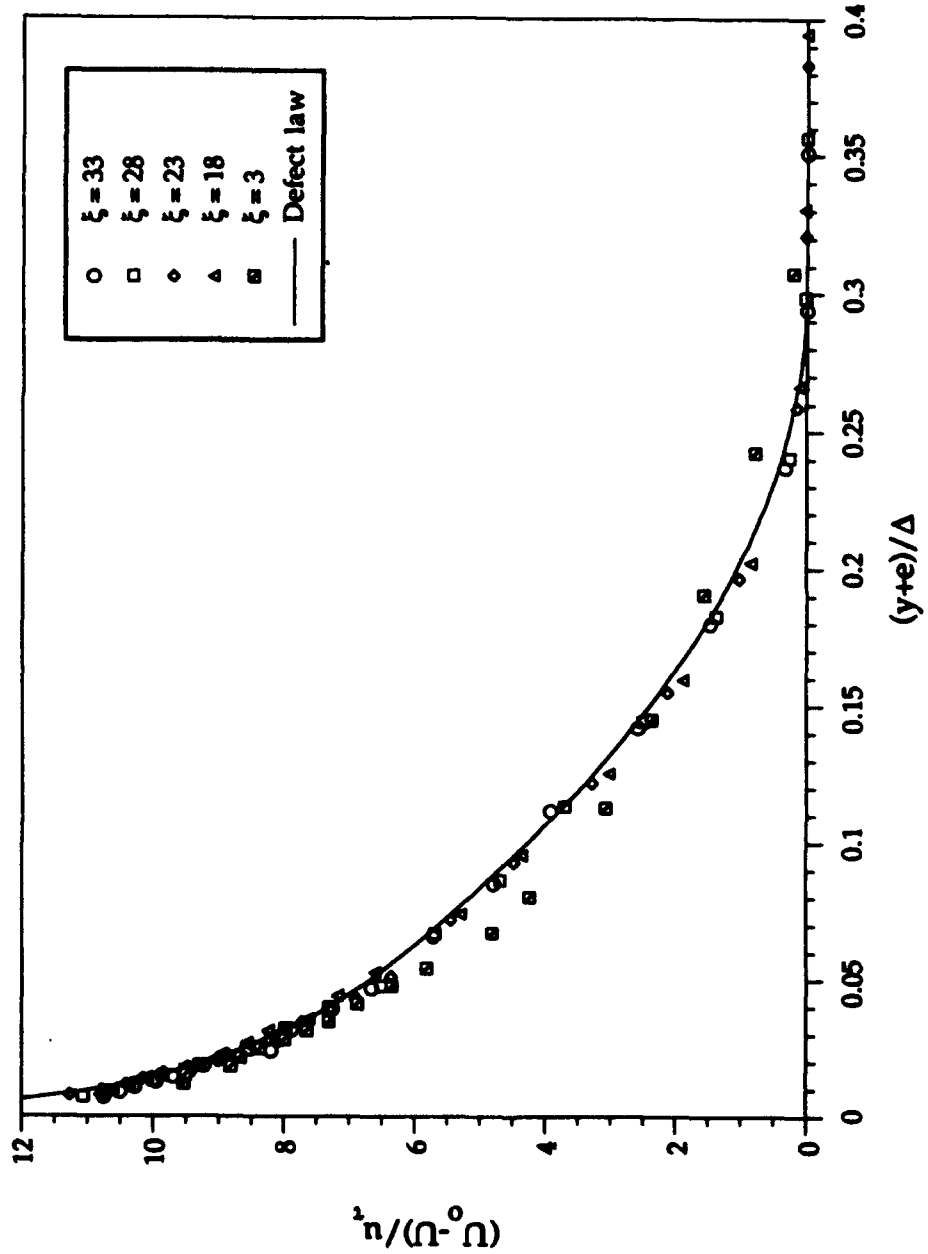


Figure 3.6 Defect velocity profiles at different stations to verify self preservation

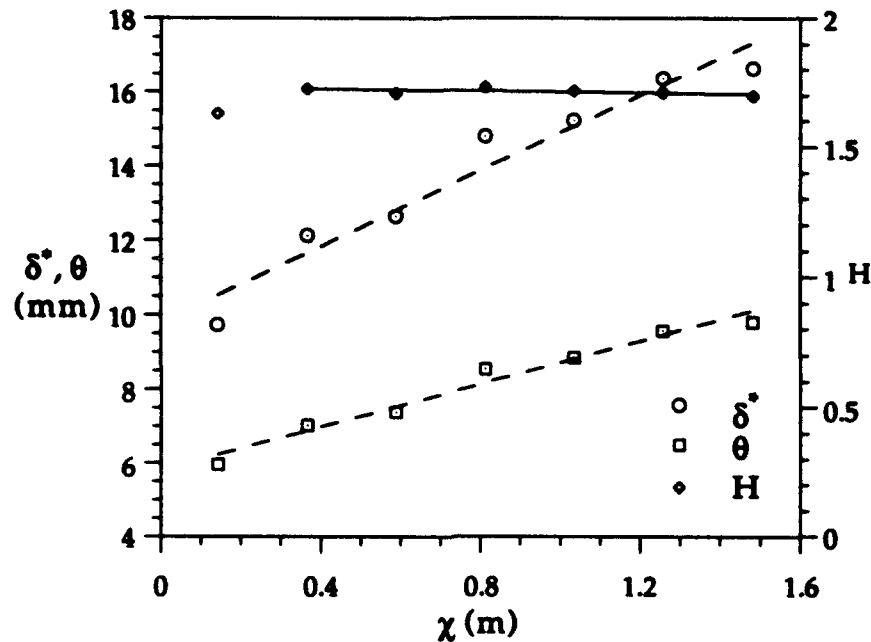


Figure 3.7 Streamwise development of integral parameters

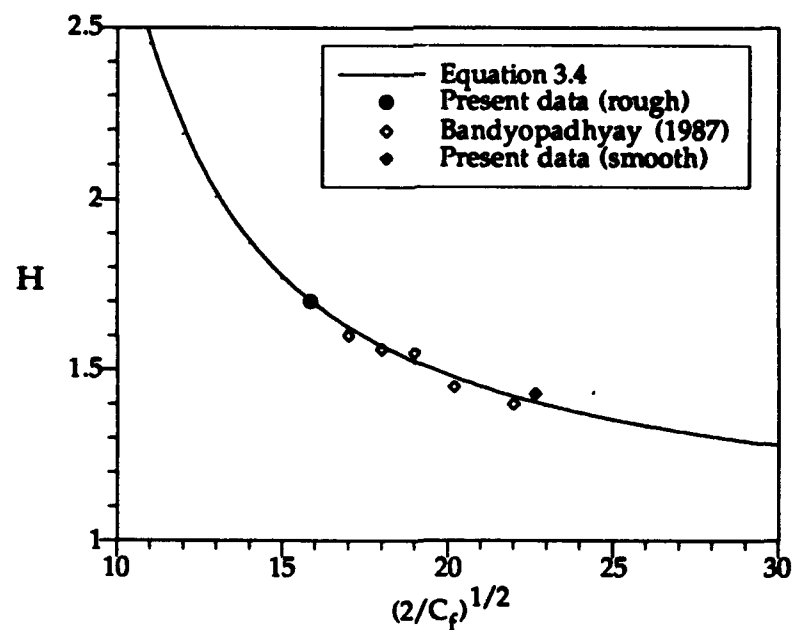


Figure 3.8 Comparison of skin friction results obtained by the profile matching method

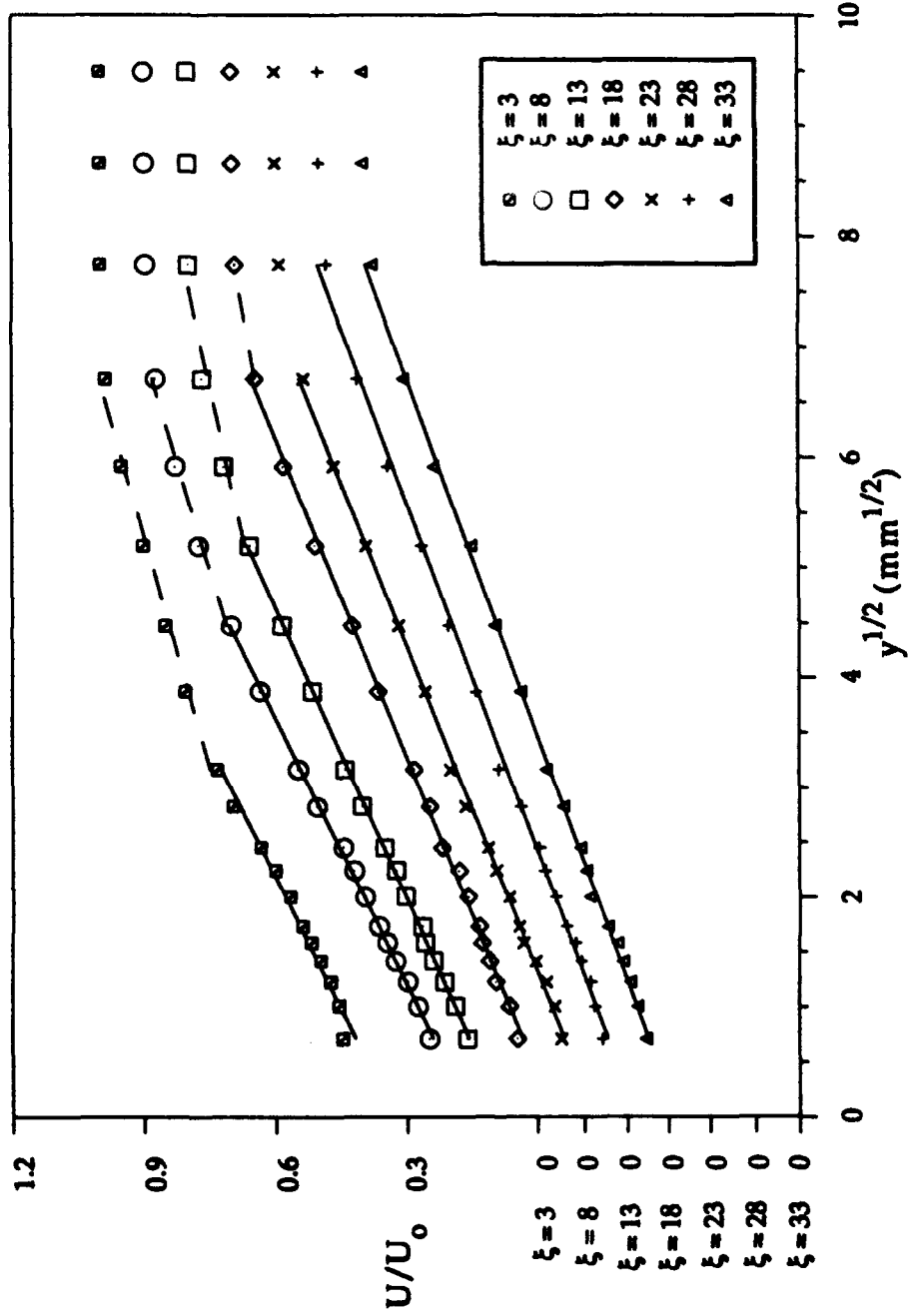


Figure 3.9 Half power plot of mean velocities showing the approximate location of the internal boundary layer from the knee point

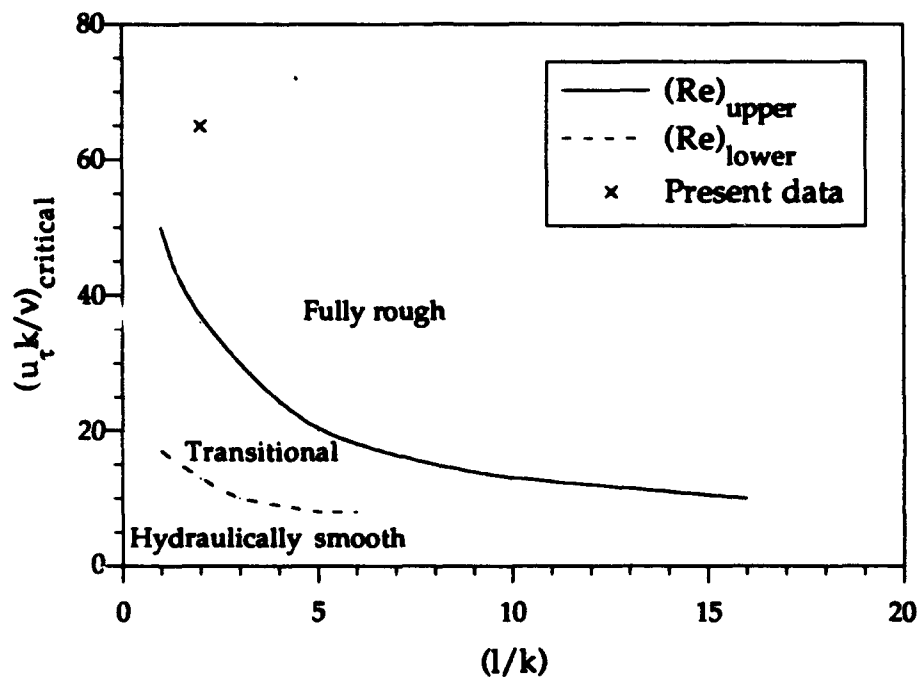


Figure 3.10 Variation of critical Reynolds numbers with the aspect ratio of roughness elements from Bandyopadhyay (1987)

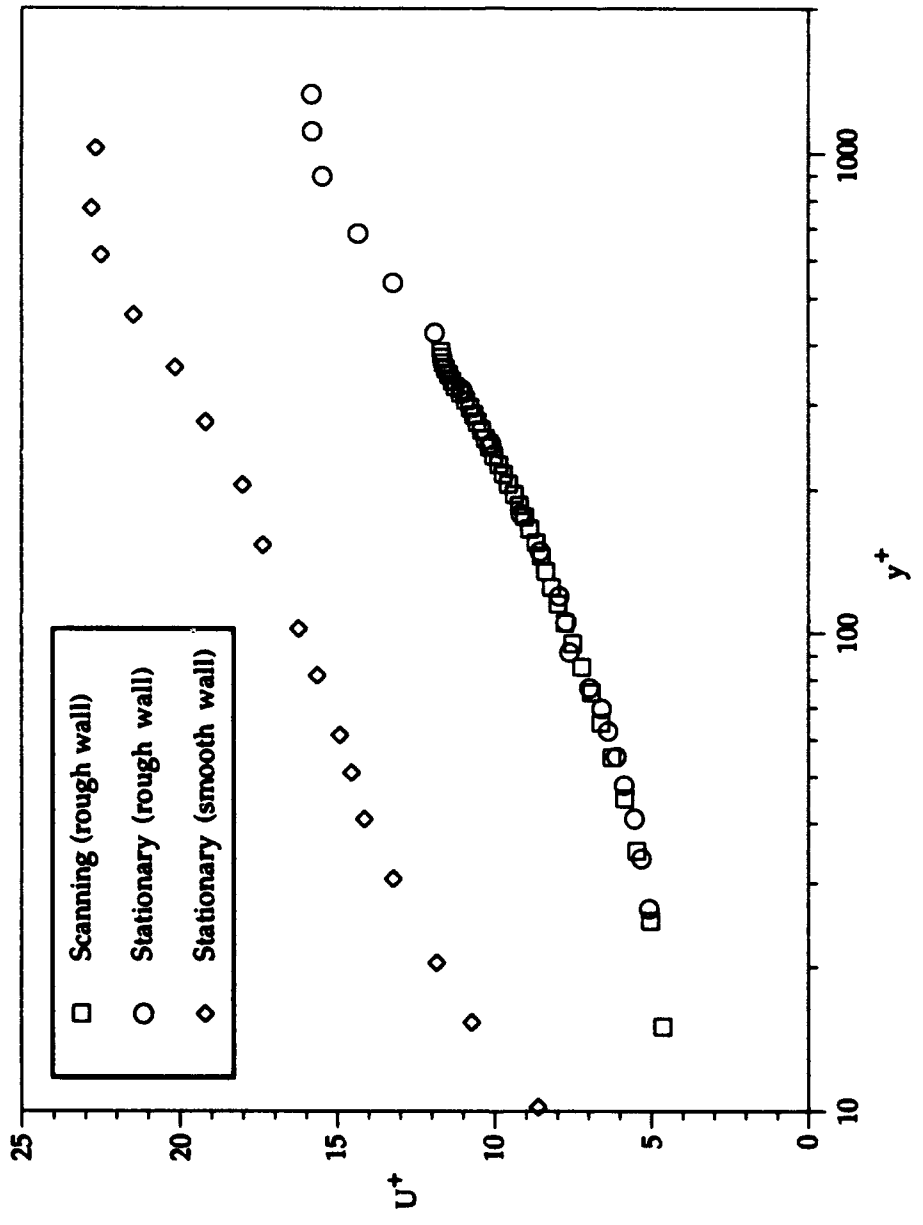


Figure 3.11 Mean velocity profile over the rough wall from scanning measurements compared with stationary measurements over rough and smooth walls.

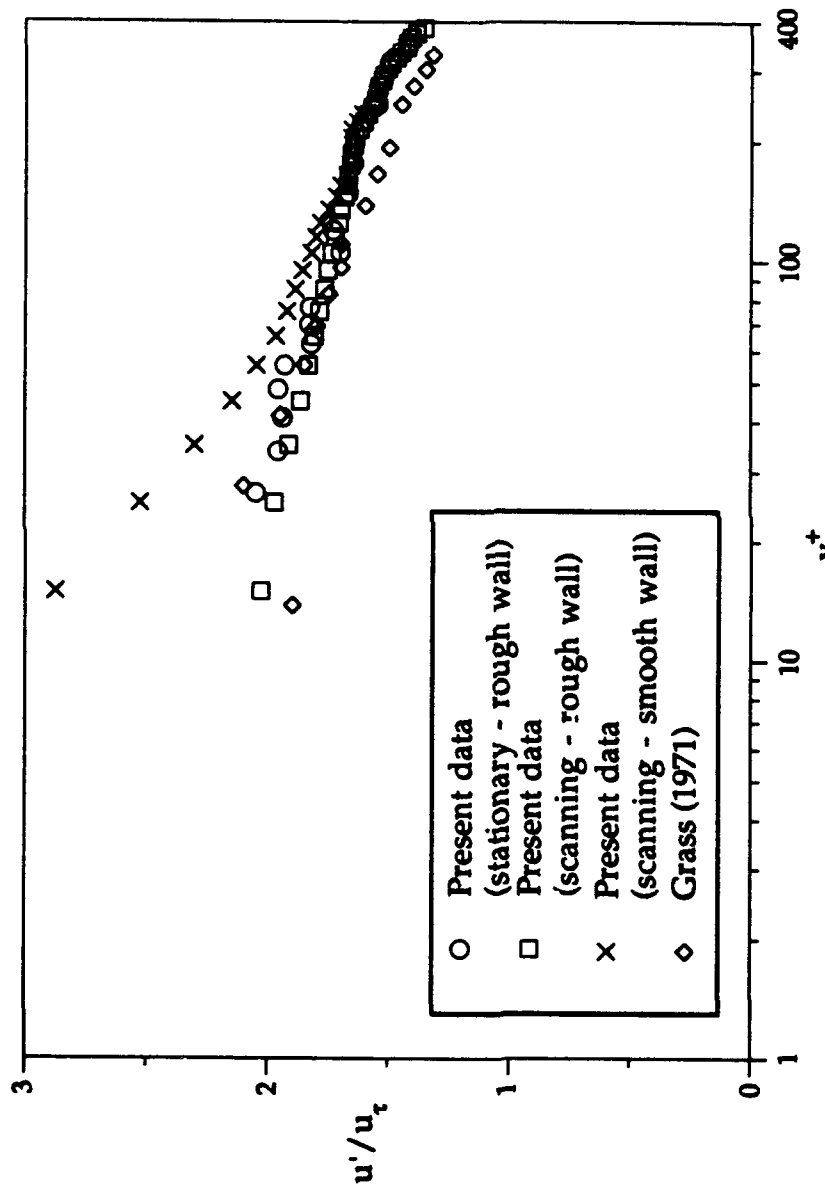


Figure 3.12 Scanning rms profile compared with stationary measurements,  
Grass (1971) and smooth wall profile.

## **CHAPTER 4**

### **RESULTS AND DISCUSSION**

Scanning data for smooth and rough walls were analyzed using both single point and spatial detection schemes. The results of single point detection were compared to other single point studies. Burst and ejection frequencies were determined and different possibilities for their scaling investigated. Categories of low and high speed spatial events were defined over the rough and smooth walls. Conditional sampling results for the spatial events are presented in this chapter. Characteristics of the spatial events over the rough and smooth wall are discussed.

#### **4.1 Single point detection**

In order to compare with other single point detection studies, a standard U-level detection was applied at  $y^+ = 35$  and  $65$ . The resulting ejections were grouped into bursts using the procedure of Barlow and Johnston (1985). This method calculates  $\tau_{\max}$ , the maximum time between ejections which can be grouped together in a burst. Details of this procedure are presented in Appendix B. Ensemble averages were then formed using the bursts aligned at

their leading edge. Burst and ejection frequencies were calculated at each bin height and different scaling parameters investigated.

#### **4.1.1 Single point detection for smooth wall**

Significant contour levels for the conditional samples were determined, as explained in section 2.5.2, to be  $|u/u_\tau| > 0.3$ . Conditionally sampled results are shown in Figure 4.1, which show the average of 536 bursts for detection at  $y^+ = 35$  and 552 bursts at  $y^+ = 65$ , all aligned at their leading edge. The contour levels in the figure are in intervals of  $|u/u_\tau| = 0.6$ . For both cases, velocity contours are centered around the detection location, which is characteristic of the single point detection scheme.

The high speed structure, though present in front of the low speed event at both detection heights, is weak and small. This is in contrast with the results of Bolton (1990), who used the same detection criteria at  $y^+ = 66$  on her scanning LDV measurements. She found the presence of a significant high speed structure in front of the low speed event as shown in Figure 4.2. The reason for this discrepancy between the single point results of Bolton and the present study are not known. Gan (1989), using the quadrant detection technique at  $y^+ = 30$  and 60, mapped the burst structure in the x-y plane. The bursts were aligned with the point of maximum

uv in the ensemble average. His results as shown in Figure 4.3 do not show the presence of any high speed fluid. The characteristics of the burst structure in terms of shape and magnitude of the contours is very similar to that found by the present study.

#### **4.1.2 Single point detection for rough wall**

Single point detection was performed at  $y^+ = 35$  and 65 in order to compare with the smooth wall case. Figure 4.4 shows the results of ensemble averaging 459 bursts at  $y^+ = 35$  and 492 at  $y^+ = 65$ , in contour levels of  $|u/u_\tau| = 0.6$ . There is no evidence of a significant high speed structure at either height, which is similar to what was observed over the smooth wall. The shape and extent of the structure at  $y^+ = 65$  is very similar to the smooth wall case, but the one at  $y^+ = 35$  is less elongated than that over the smooth wall. Therefore the presence of roughness elements in the flow has an effect on the structure of the burst event only when it is very close to the wall.

#### **4.1.3 Burst and ejection frequencies**

Burst and ejection frequencies at discrete bin heights were calculated for rough and the smooth wall. Results for the smooth

wall were described in section 3.1.2. Compared to the smooth wall,  $\tau_{\max}$  decreased by 15% over the rough wall. This implied that the number of ejections which could be grouped together into a burst decreased and the number of bursts with just one ejection increased.

As  $Re_0$  for the two experiments were different, the smooth wall results were extrapolated to the  $Re_0$  for the rough wall. This was done using the results of Coughran (1988), who found that for a smooth wall the ejection and burst frequencies normalized by the inner variables were constant over a broad range of  $Re_0$ .

It was found that at the same threshold, the burst and ejection frequencies increased over the rough wall, as shown in Figure 4.5. Three different types of scaling were investigated, in order to find scaling parameters that normalized the effect of surface roughness for the burst and ejection frequencies. The first of these, shown in Figure 4.6 was based on the inner variables ( $u_T$  and  $v$ ). It is clear that the inner variables fail to collapse data from the smooth and rough wall. The normalized burst and ejection frequencies over the rough wall are about half of that over the smooth wall.

Figure 4.7 shows the burst and ejection frequencies normalized by mixed variables ( $\delta$  and  $u_T$ ). The mixed scaling does better than the inner scaling but doesn't collapse the frequency data satisfactorily. For the outer scaling, shown in Figure 4.8, the normalizing variables are  $\delta$  and  $U_\infty$ . The ejection frequencies do

not collapse over the full range of  $y^+$ . There is good agreement between the smooth and rough wall frequency data for the burst frequencies. Therefore, outer variables seem to be the appropriate scaling parameters, though data over a range of Reynolds numbers would have to be considered to make a definite statement.

The fact that the outer scaling does a good job of collapsing the burst frequencies from the smooth and rough wall is contrary to what Raupach (1981) found from his measurements over a smooth wall and rough surfaces of different concentration. He found that the at any fixed detection threshold, mixed scaling collapsed the ejection frequency data from all the rough surfaces and the smooth surface. Coughran (1988) found that over a smooth wall, the burst and ejection frequencies scaled with inner variables for a range of Reynolds numbers. From the large difference in the normalized frequencies for the rough and smooth wall based on the inner variables, it is clear that inner scaling will not collapse data from both smooth and rough surfaces.

#### 4.2 Smooth wall spatial events

Bolton (1990) did conditional samples by dividing the events into categories of small, medium or large based on the size, and near or far based on the maximum height from the wall. There was

a large difference in the conditionally sampled structures depending on whether the detected structure had a maximum height near or far from the wall. Therefore in this study conditional sampling was done based on the maximum or minimum height of the event. The small and medium groups were combined, limiting the size of the events to  $2 < \text{size} < 32$ , which accounted for about 85% of the events. Categories were defined in terms of the range in which the maximum or minimum height of the event could lie. This ensured that events at about the same stage of their development were included in the ensemble averages.

#### **4.2.1 Low speed spatial events**

The low speed events were categorized based on their maximum height as bursts tend to move upwards from the wall. If one presumes that the maximum height of the burst is an indication of the stage of its development as it moves away from the wall, categories at increasing heights from the wall are an indication of how a burst evolves. A threshold of  $L_L = 0.7$  was picked for this analysis. Each category had about 200 events for the ensemble average. Details about each category are presented in Table 4.1.

**Table 4.1 Categories of low speed spatial events based on a range of maximum heights.**

<u>Category</u>	<u>Number of events</u>	<u>Location of maximum height of event (wall units)</u>
H1	160	$15 \leq \text{max} < 45$
H2	249	$45 \leq \text{max} < 65$
H3	208	$65 \leq \text{max} < 85$
H4	210	$85 \leq \text{max} < 105$
H5	272	$105 \leq \text{max} < 135$
H6	243	$135 \leq \text{max} < 165$
H7	205	$165 \leq \text{max} < 195$
H8	222	$195 \leq \text{max} < 225$
H9	647	$225 \leq \text{max} < 245$

Figures 4.9 (a) through (i) show a sequence of the low speed spatial event ensemble averages at different height categories. Each of the figures will be referred to by the height category. At H1 the low speed spatial event is very intense and close to the wall. At increasing height categories it becomes less intense and bigger. At height H4 it is completely detached from the wall. From height H5 to H9 the low speed spatial event remains about the same size and intensity.

Figure 4.9 also shows movement of the high speed structure associated with the low speed spatial event. At H1 a high speed structure appears over the low speed spatial event. At H2 this high

speed structure moves over and downstream of the low speed spatial event and by H3 is present both downstream and above the low speed spatial event. It has also increased in size and extends across the full range presented in the figure. At higher heights (H6 to H9), the high speed structure appears below the low speed spatial event.

#### 4.2.2 High speed spatial events

The high speed events were conditionally sampled based on their minimum height as sweeps are expected to move towards the wall. A threshold of  $L_H = 0.8$  was used for this analysis. Categories similar to the low speed spatial events were maintained to allow comparison at the same heights. The category H1 was divided into three sub-categories for more detail in the region  $15 \leq y^+ < 45$ . Details about each category are in Table 4.2.

Category H9 had very few events to give a good average and is not shown in Figures 4.10 (a) through (j), which show the results for the high speed spatial event at different categories. Starting from height H8, the high speed spatial event remains about the same size and intensity, till it reaches height H2. At categories closer to the wall the high speed spatial event becomes bigger and more intense as in H1C through H1A.

**Table 4.2 Categories of high speed spatial events based on a range of minimum heights.**

<u>Category</u>	<u>Number of events</u>	<u>Location of minimum height of event (wall units)</u>
H1A	232	15 ≤ min < 25
H1B	312	25 ≤ min < 35
H1C	148	35 ≤ min < 45
H2	215	45 ≤ min < 65
H3	181	65 ≤ min < 85
H4	153	85 ≤ min < 105
H5	258	105 ≤ min < 135
H6	264	135 ≤ min < 165
H7	326	165 ≤ min < 195
H8	282	195 ≤ min < 225
H9	48	225 ≤ min < 245

The low speed structure associated with the high speed spatial event is not spread out like the high speed structure associated with the low speed spatial events, but is present in small concentrated areas. The low speed structure is found below the high speed spatial event, from heights H8 to H4. At H3, the low speed structure is confined between the wall and the high speed spatial event. It is present upstream of the high speed event at this height. It becomes smaller, more intense and moves downstream of the high speed spatial event, as is clear from heights H3 to H1C.

At heights closer to the wall the low speed structure disappears from below the high speed event and instead appears above it.

The low speed spatial event detected at heights H1 through H3 has high speed fluid above it. The high speed spatial event has low speed fluid below it when detected at heights H1C through H3. Therefore the relative position of low and high speed fluid remains the same, though the events being detected are different for both cases.

#### 4.3 Rough wall spatial events

Conditional sampling was done over the rough wall following the same procedure as outlined for the smooth wall, which included grouping of events, selection of threshold and significant contour levels, etc. Since the scan range was larger for the rough wall, there were a greater number of categories. Similar categories were maintained in the common region as in the smooth wall, to allow a direct comparison with the spatial events over the smooth wall at the same heights. A description of low and high speed spatial events and structures associated with them over the rough wall follows. This includes comparisons with the smooth wall results.

#### 4.3.1 Low speed spatial events

A threshold of  $L_L = 0.8$  was used for this analysis, with categories being the same as over the smooth wall from height H1 to H8. The different categories based on the maximum height of the event are shown in Table 4.3.

**Table 4.3 Categories of low speed spatial events over rough wall based on a range of maximum heights.**

<u>Category</u>	<u>Number of events</u>	<u>Location of maximum height of event (wall units)</u>
H1	132	$15 \leq \text{max} < 45$
H2	169	$45 \leq \text{max} < 65$
H3	175	$65 \leq \text{max} < 85$
H4	165	$85 \leq \text{max} < 105$
H5	240	$105 \leq \text{max} < 135$
H6	262	$135 \leq \text{max} < 165$
H7	250	$165 \leq \text{max} < 195$
H8	227	$195 \leq \text{max} < 225$
H9	207	$225 \leq \text{max} < 255$
H10	193	$255 \leq \text{max} < 285$
H11	194	$285 \leq \text{max} < 315$
H12	196	$315 \leq \text{max} < 345$
H13	185	$345 \leq \text{max} < 375$
H14	559	$375 \leq \text{max} < 395$

The conditional sampling results for each of the above categories are presented in Figure 4.11 (a) through (n). The low speed spatial event is small and intense near the wall at height H1. It becomes bigger and loses some of its intensity when it reaches height H3. It detaches from the wall at height H5 and stays about the same size and intensity at increasing heights from the wall.

This behavior of the low speed spatial event is quite different from the smooth wall case, where it became smaller and decayed in intensity at increasing heights from the wall. On the rough wall, the low speed spatial event is bigger and maintains the same level of intensity from  $y^+ = 85$  to the maximum height in the scan range. This presence of the more intense low speed event at higher heights over the rough wall, compared to the smooth wall, is consistent with the region of greatest mixing moving outwards and being spread over a larger extent on rough walls as reported by Ligrani and Moffat (1986). The low speed event being bigger and more intense over the rough wall is consistent with the space-time correlation and Reynolds stress results of Sabot, Saleh and Comte-Bellot (1977).

The behavior of the high speed structure associated with the low speed spatial event is markedly different over the rough wall. Figure 4.12 shows both smooth and rough wall low speed spatial events at heights H2 and H3. The behavior of the high speed

structure associated with the low speed spatial event at other heights is similar. Unlike the smooth wall which has large expanses of high speed structure associated with the low speed spatial event, there is no significant amount of high speed structure associated with low speed spatial event over the rough wall.

#### 4.3.2 High speed spatial events

Table 4.4 shows the details about the conditionally sampled high speed spatial events sampled based on their minimum height at a threshold of  $L_H = 0.8$ . As for the smooth wall case, the category H1 was divided into three sub-categories for more detail in the region  $15 \leq y^+ < 45$  and categories similar to the low speed spatial events were maintained to allow comparison at the same heights. The conditional sampling results for each of the above categories are presented in Figure 4.13 (a) through (o). As the number of events in category H14 were too few to give a good average, it is not included in Figure 4.13.

The high speed spatial event over the rough wall behaves similar to what it did over the smooth wall. Starting at height H13, the high speed spatial event becomes smaller as it reaches H9. From height H8 on down, it maintains its size and intensity at the same levels, till it reaches height H2. When detected at lower heights it is

larger and more intense, as seen at heights H1A and H1B. The size and intensity of the high speed spatial event over the rough wall are almost identical to that over the smooth wall in the common region.

**Table 4.4 Categories of high speed spatial events over rough wall based on a range of minimum heights.**

<u>Category</u>	<u>Number of events</u>	<u>Location of minimum height of event (wall units)</u>
H1A	335	15 ≤ min < 25
H1B	162	25 ≤ min < 35
H1C	77	35 ≤ min < 45
H2	175	45 ≤ min < 65
H3	170	65 ≤ min < 85
H4	168	85 ≤ min < 105
H5	248	105 ≤ min < 135
H6	227	135 ≤ min < 165
H7	196	165 ≤ min < 195
H8	214	195 ≤ min < 225
H9	222	225 ≤ min < 255
H10	199	255 ≤ min < 285
H11	243	285 ≤ min < 315
H12	289	315 ≤ min < 345
H13	264	345 ≤ min < 375
H14	28	375 ≤ min < 395

The low speed structure associated with the high speed spatial event also behaves in a manner similar to what it did over the smooth wall. Very close to the wall, at height  $H_1$ , it appears above the high speed event and at higher heights it appears below the high speed event.

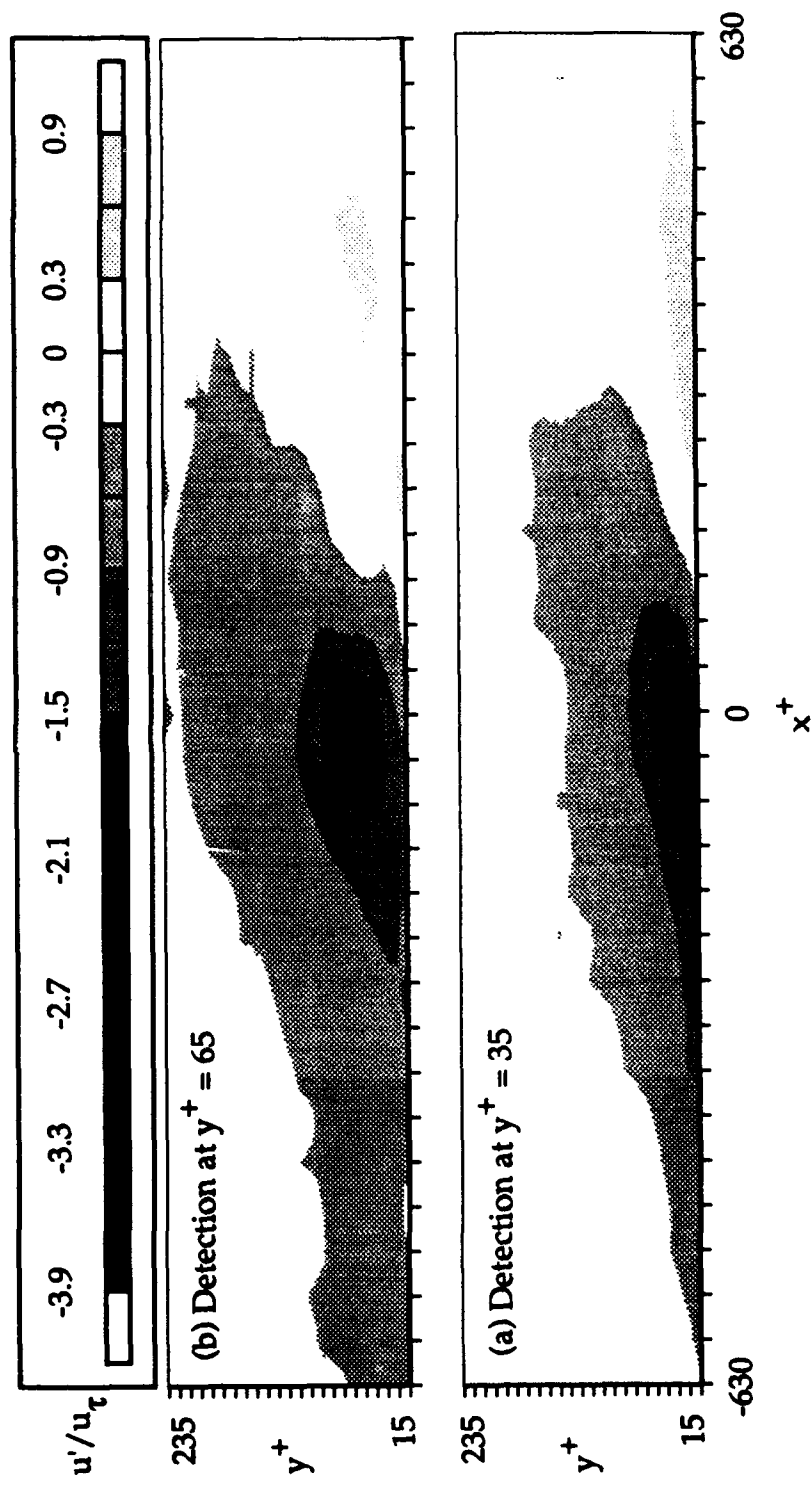


Figure 4.1 Single point detection results at detection heights of  $y^+ = 35$  and 65.

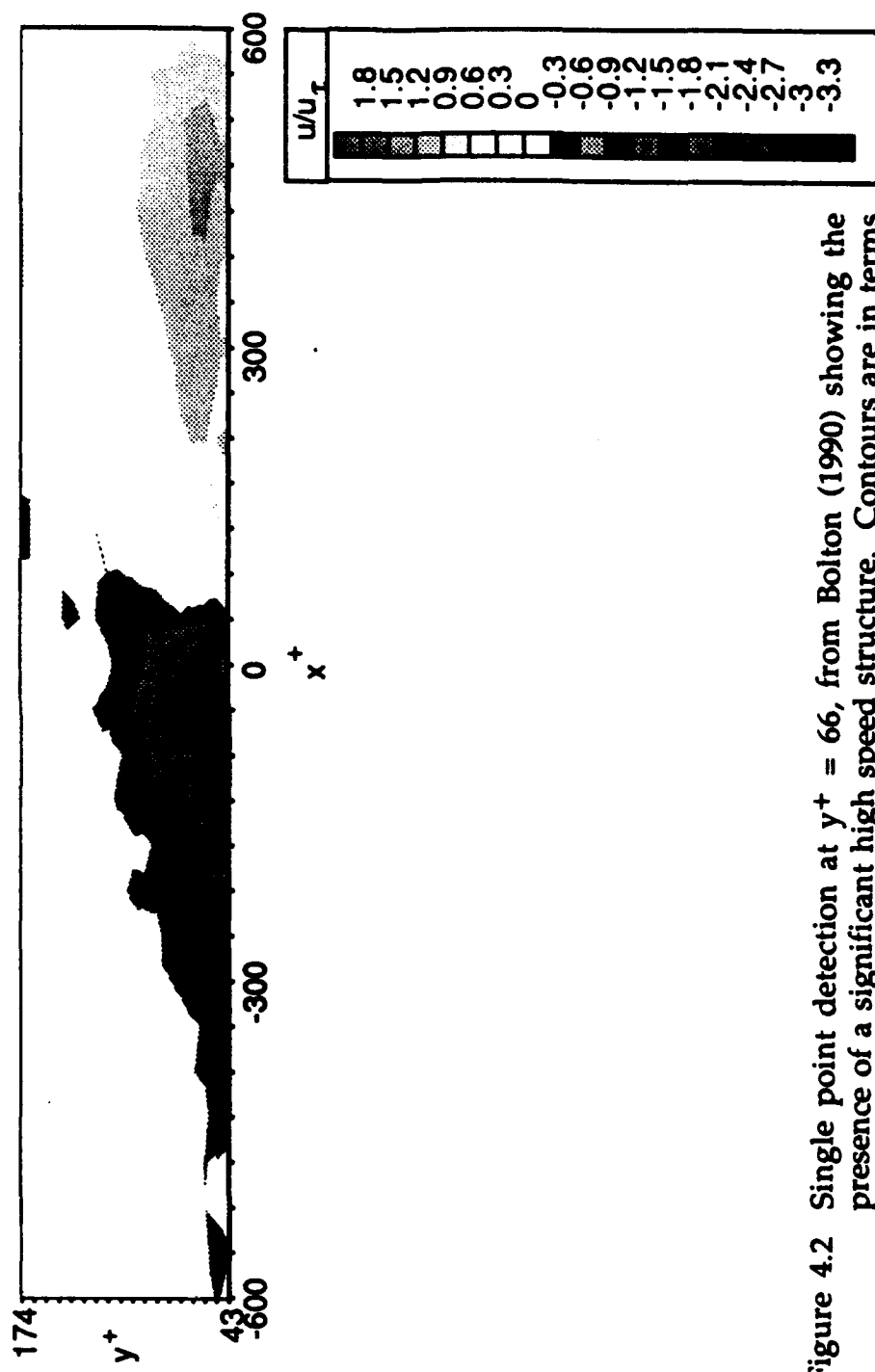


Figure 4.2 Single point detection at  $y^+ = 66$ , from Bolton (1990) showing the presence of a significant high speed structure. Contours are in terms of fluctuating velocities normalized by the friction velocity.

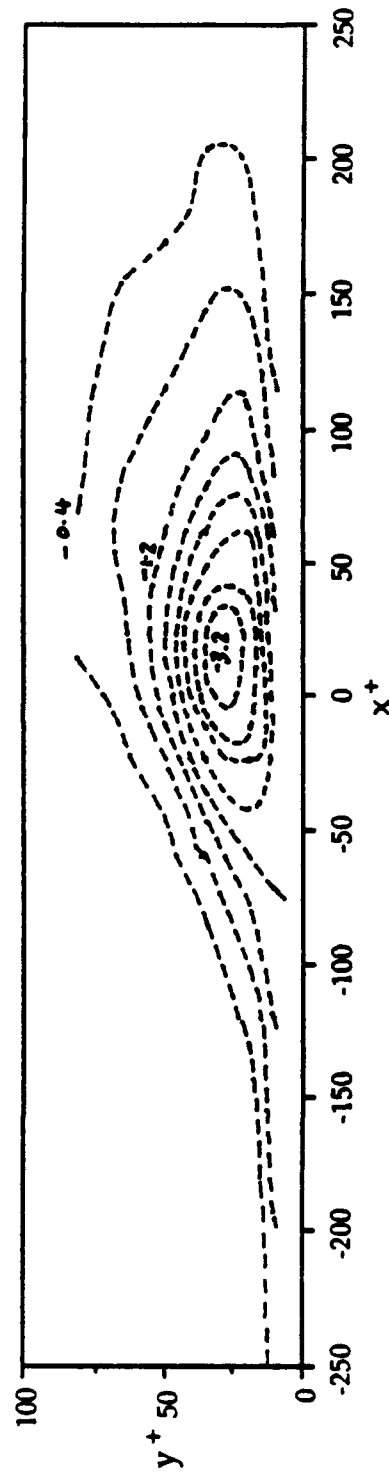


Figure 4.3 Single point detection at  $y^+ = 60$ , from Gan (1989) showing no high speed region.  
Contours are in terms of fluctuating velocities normalized by the friction velocity.

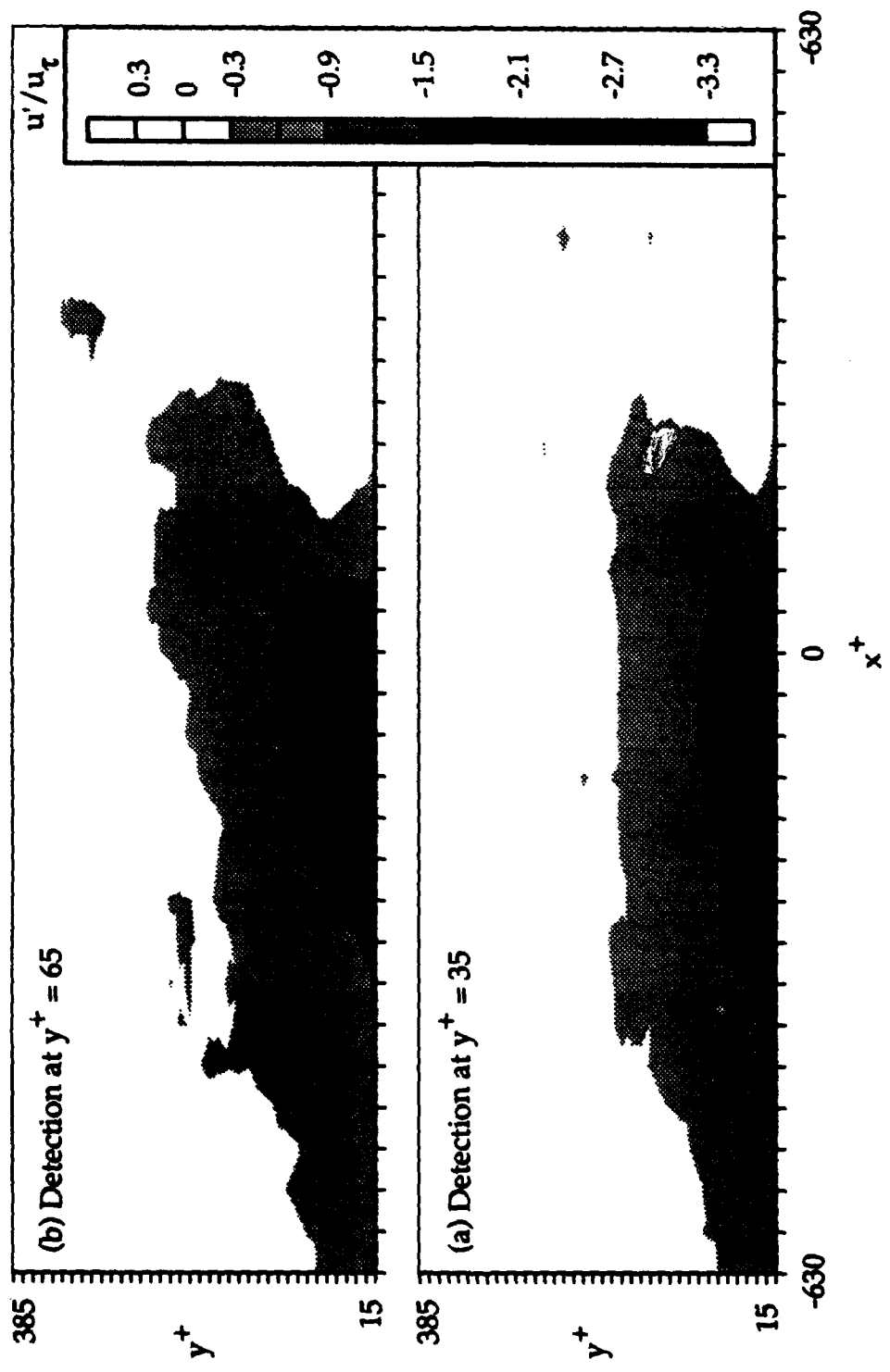


Figure 4.4 Single point detections over rough wall at  $y^+ = 35$  and 65

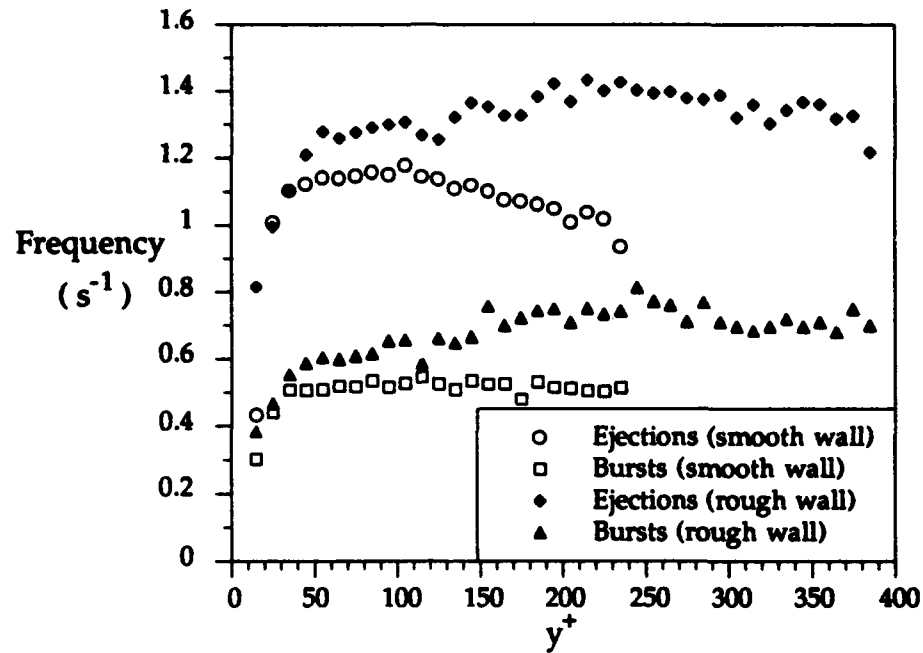


Figure 4.5 Burst and ejection frequencies over the smooth and rough wall.

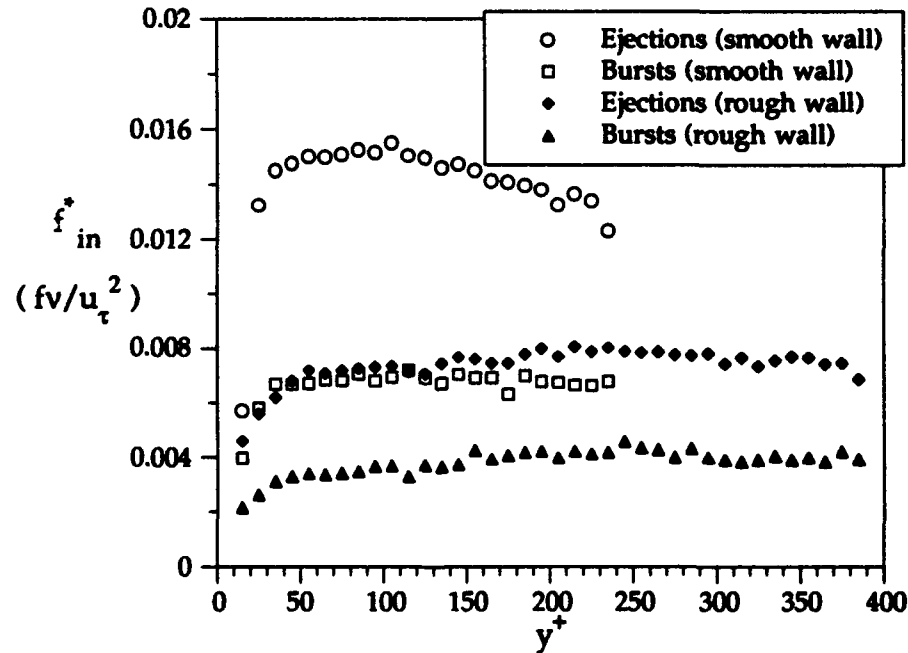


Figure 4.6 Burst and ejection frequencies scaled with inner variables.

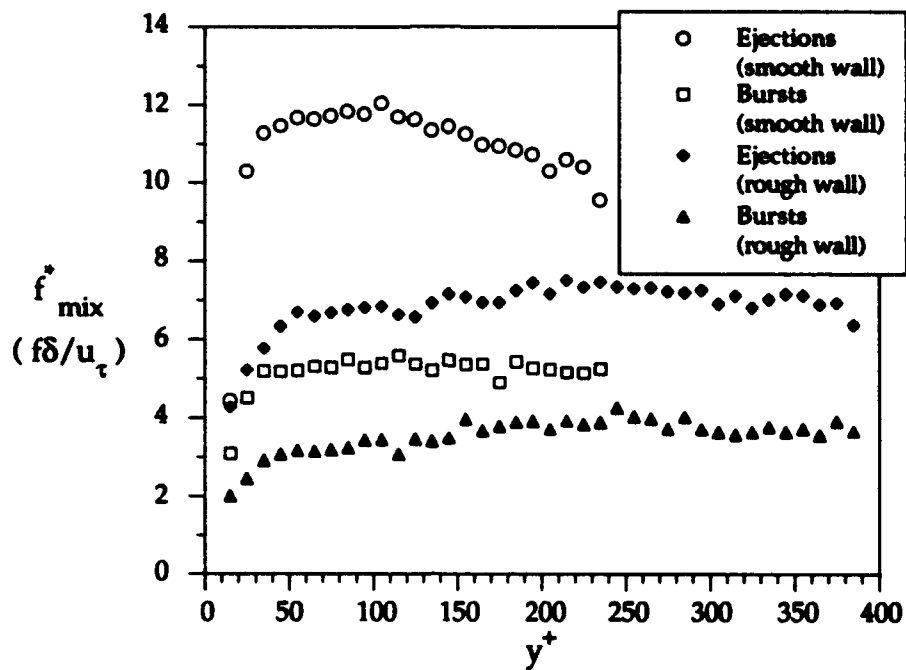


Figure 4.7 Burst and ejection frequencies scaled with mixed variables.

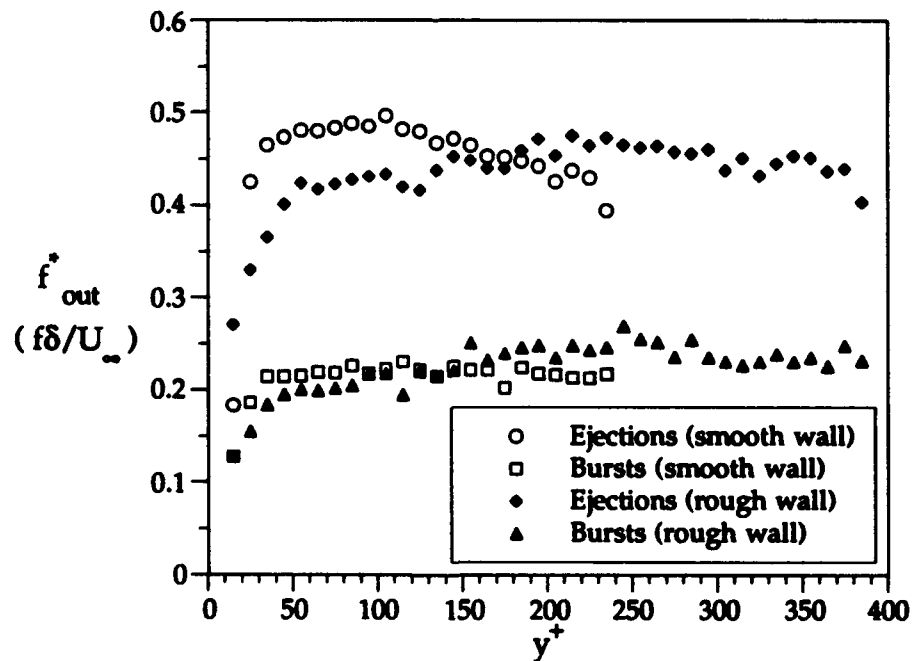
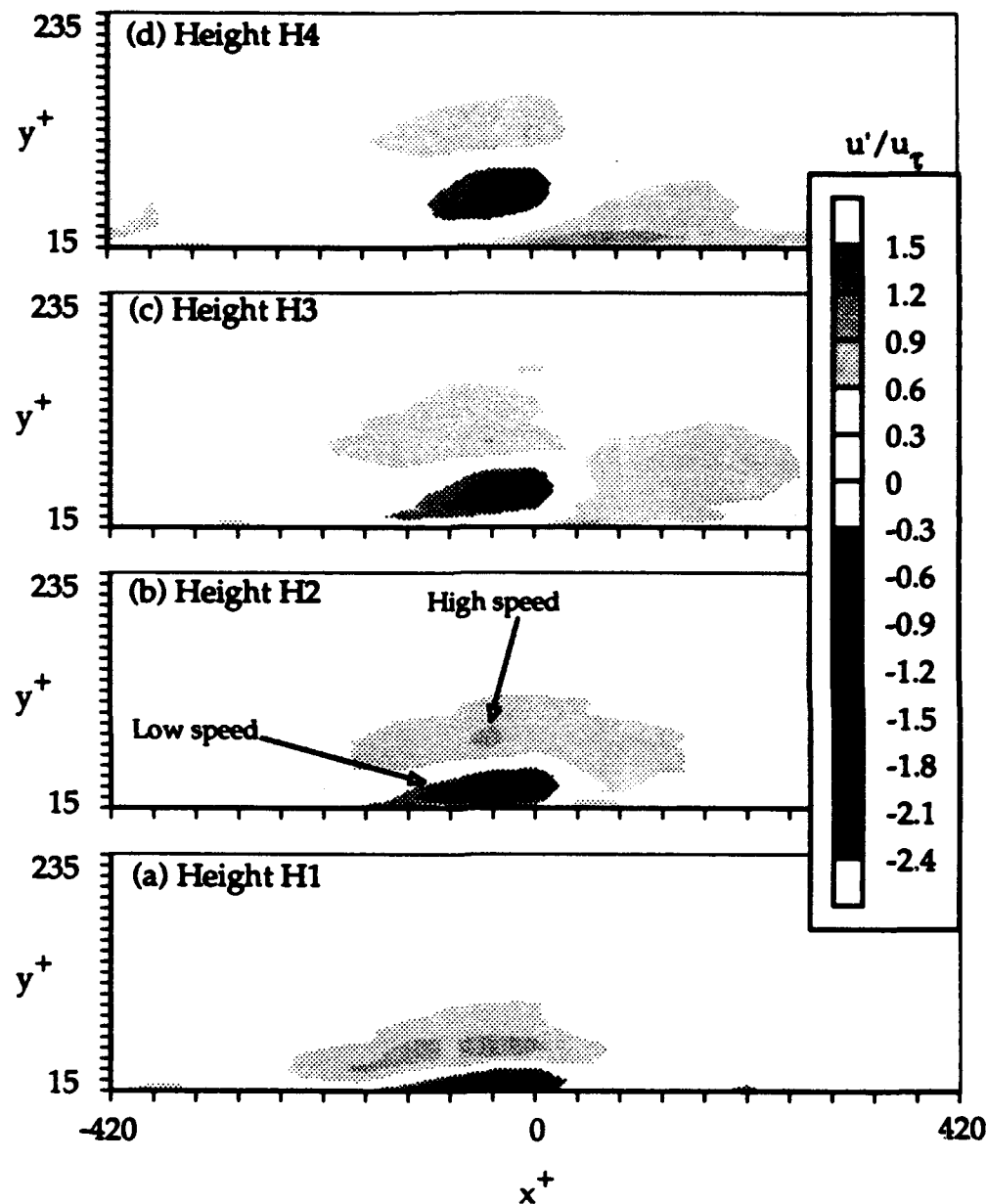
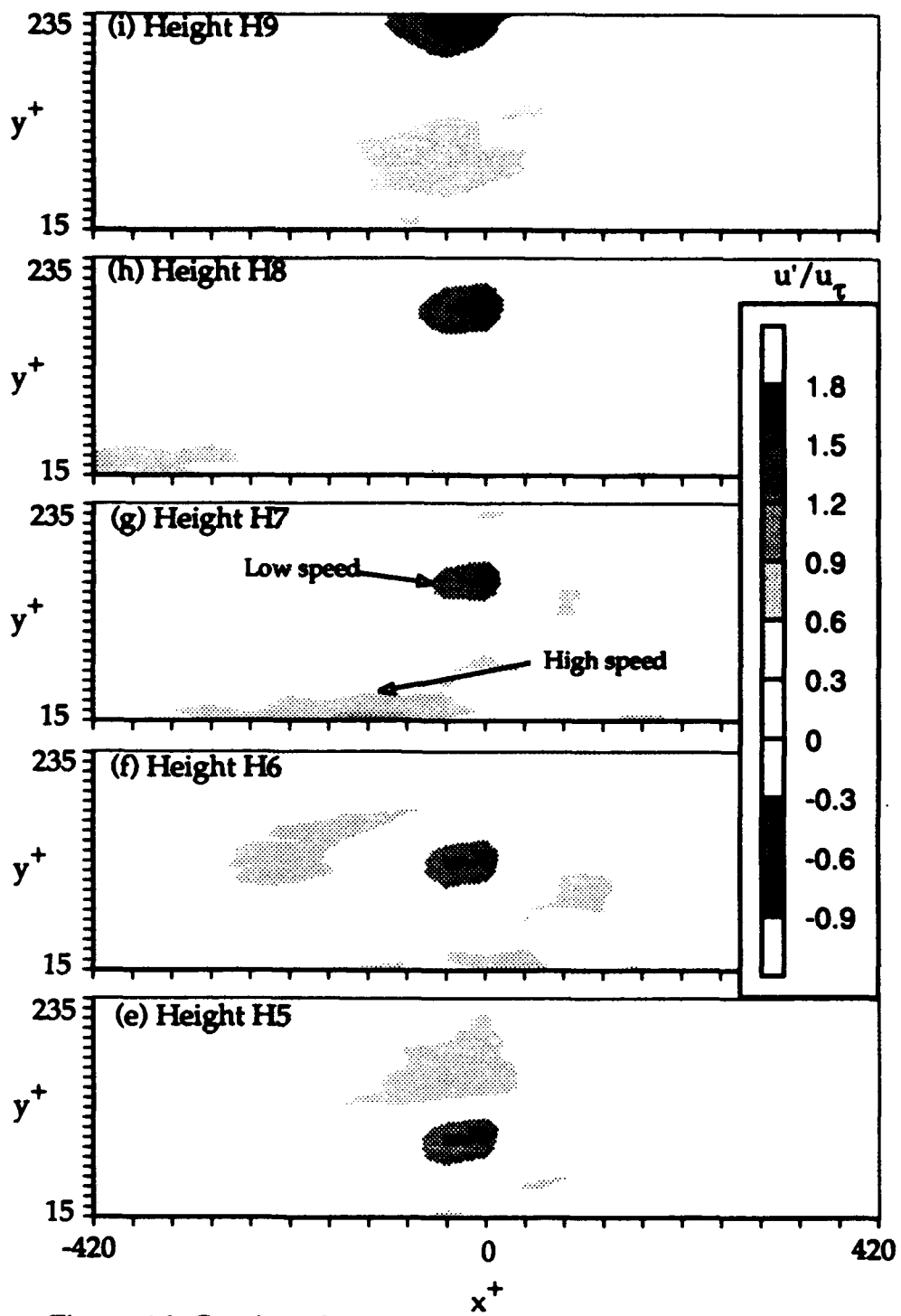


Figure 4.8 Burst and ejection frequencies scaled with outer variables.



**Figure 4.9** Conditional samples of low speed spatial events over the smooth wall at different height categories based on their maximum height from the wall. See Table 4.1 for details.



**Figure 4.9** Continued.

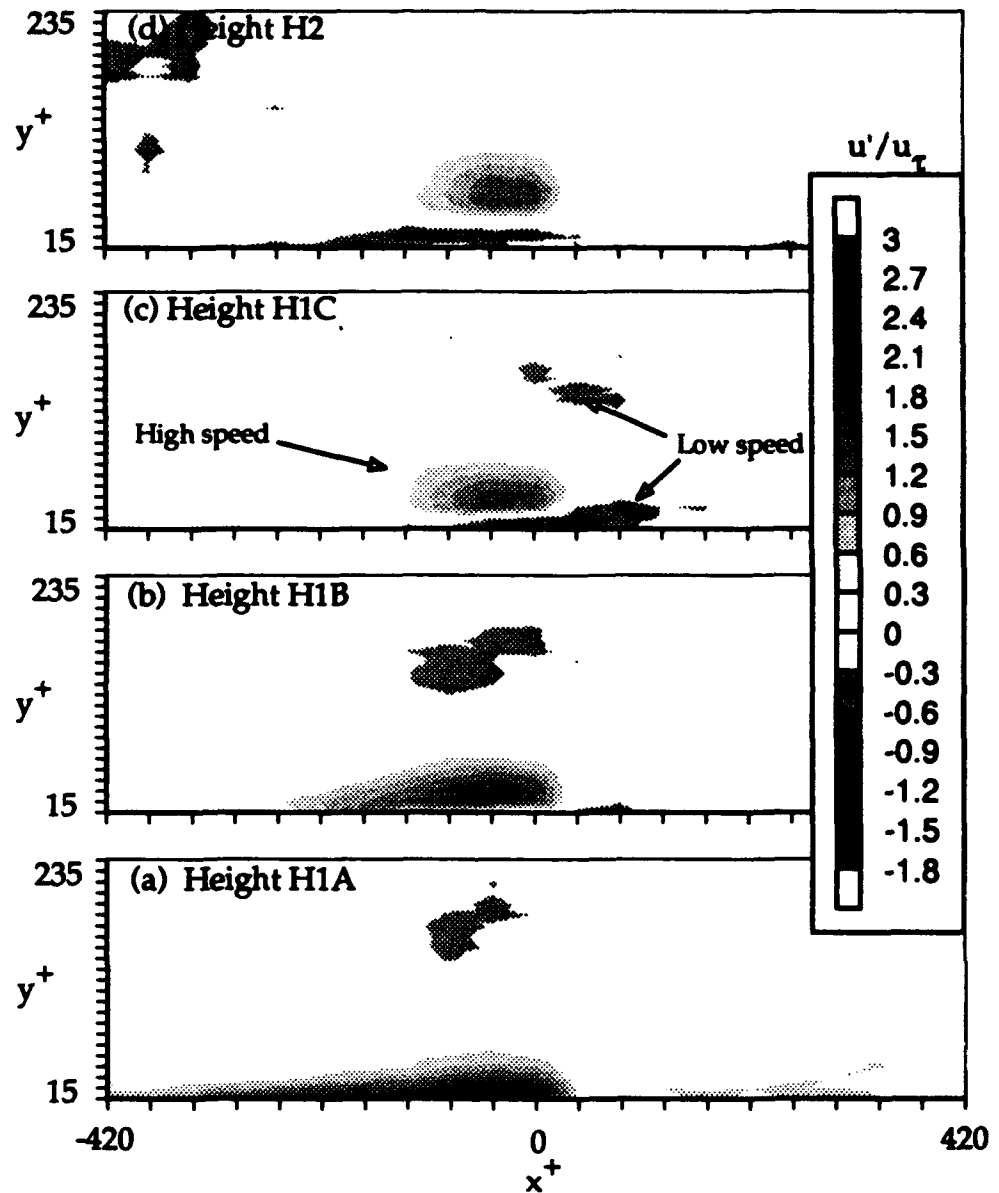


**Figure 4.10** Conditional samples of high speed spatial events over the smooth wall at different height categories based on their minimum height from the wall. See Table 4.2 for details.

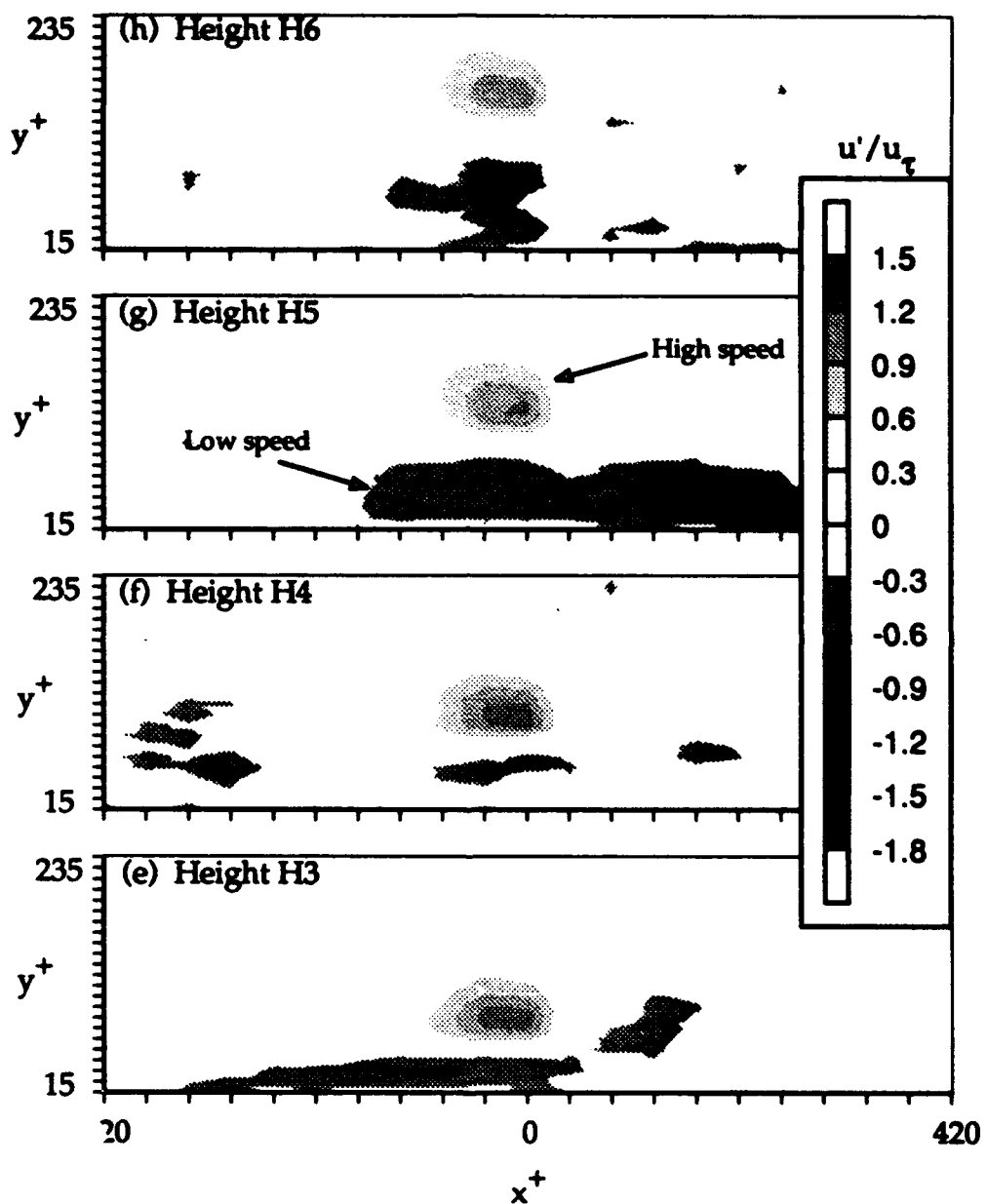


Figure 4.10 Continued.

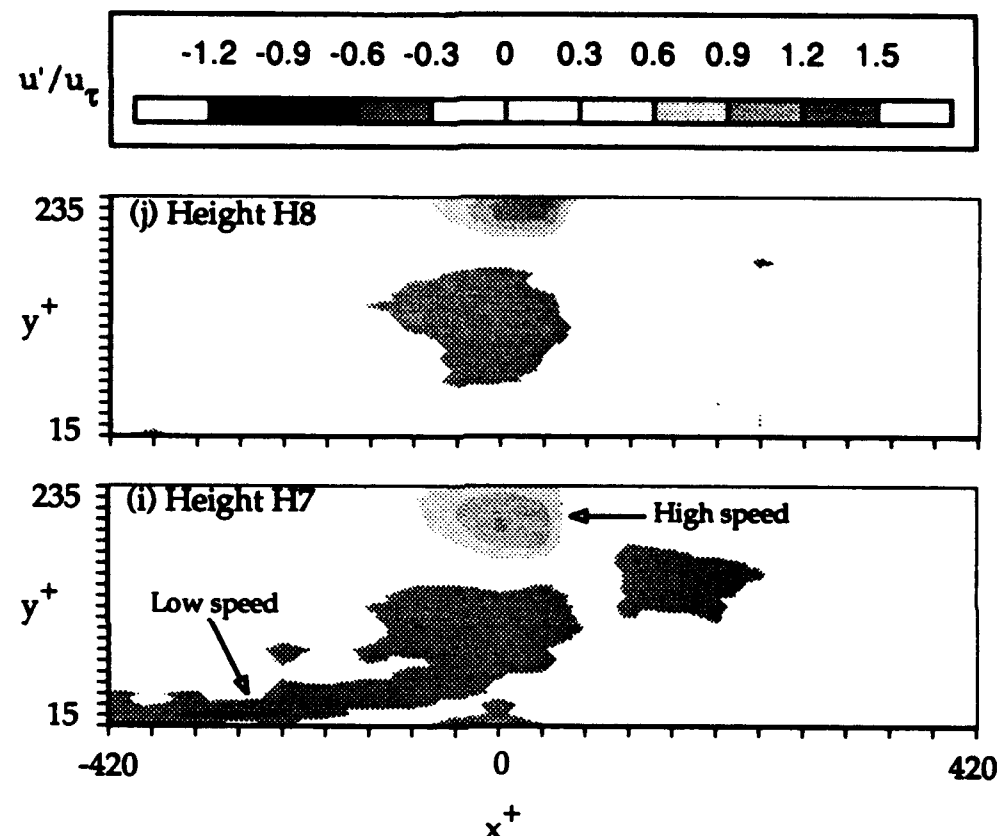


Figure 4.10 Continued.

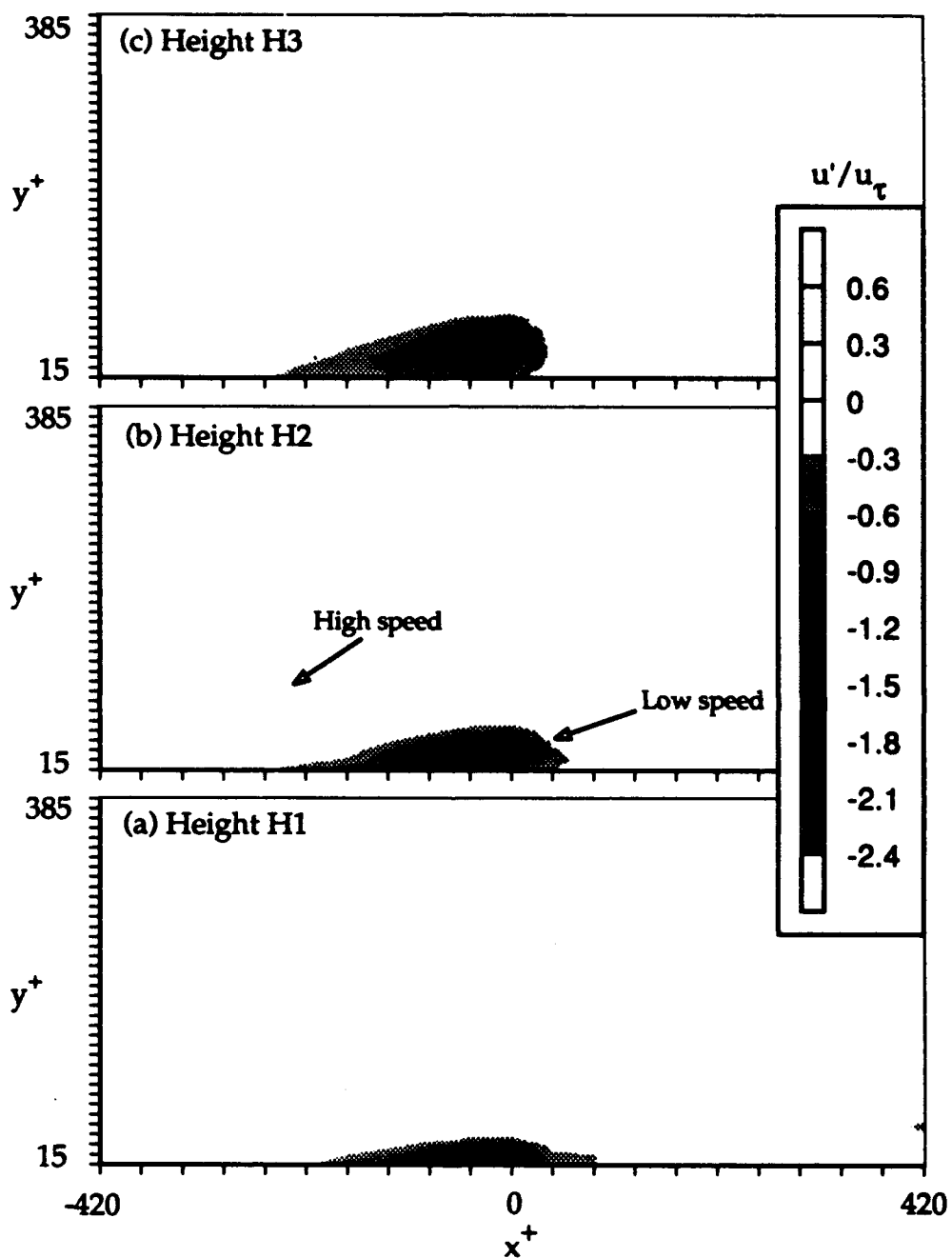


Figure 4.11 Conditional samples of low speed spatial events over the rough wall at different height categories based on their maximum height from the wall. See Table 4.3 for details.

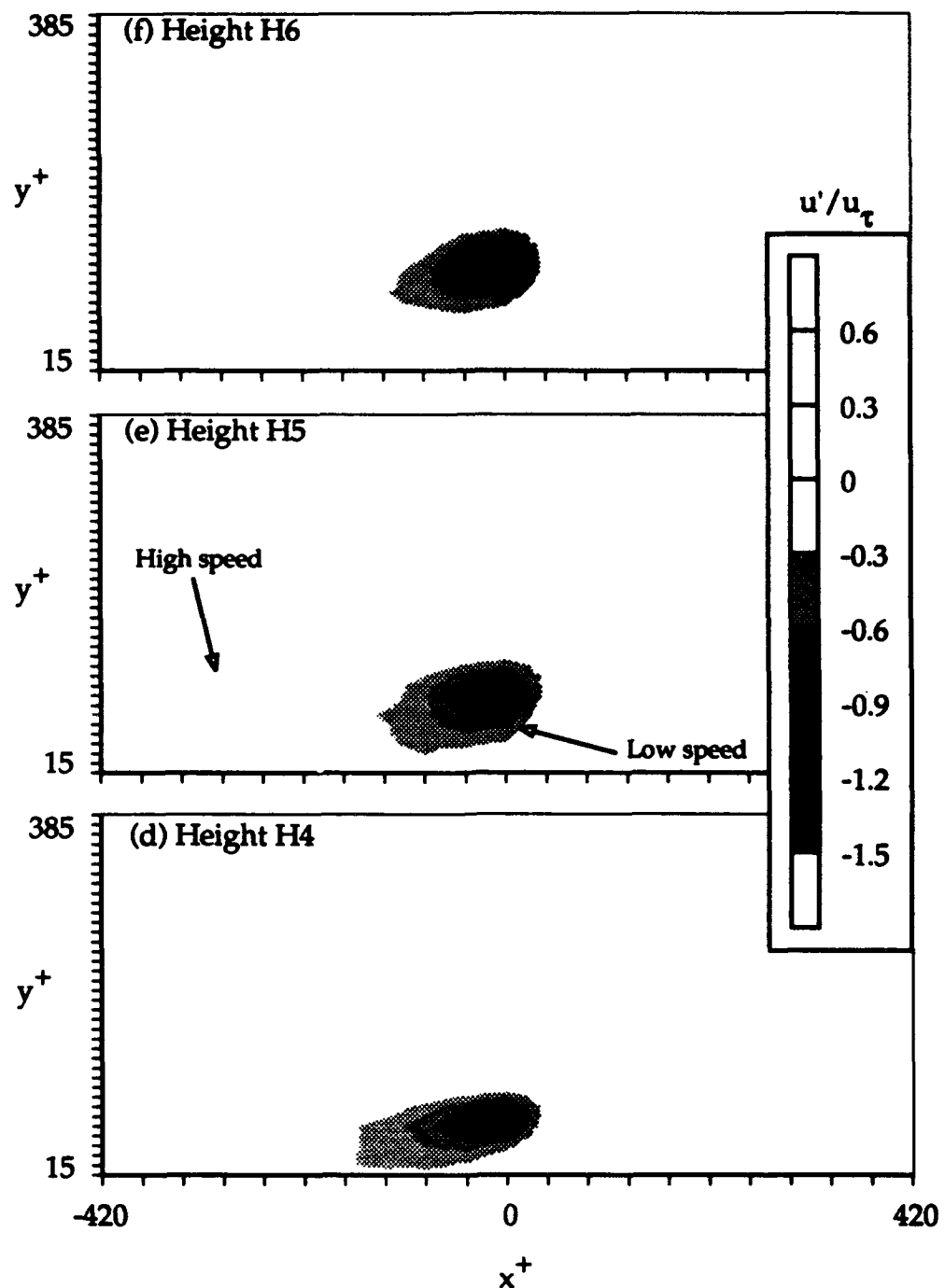


Figure 4.11 Continued.

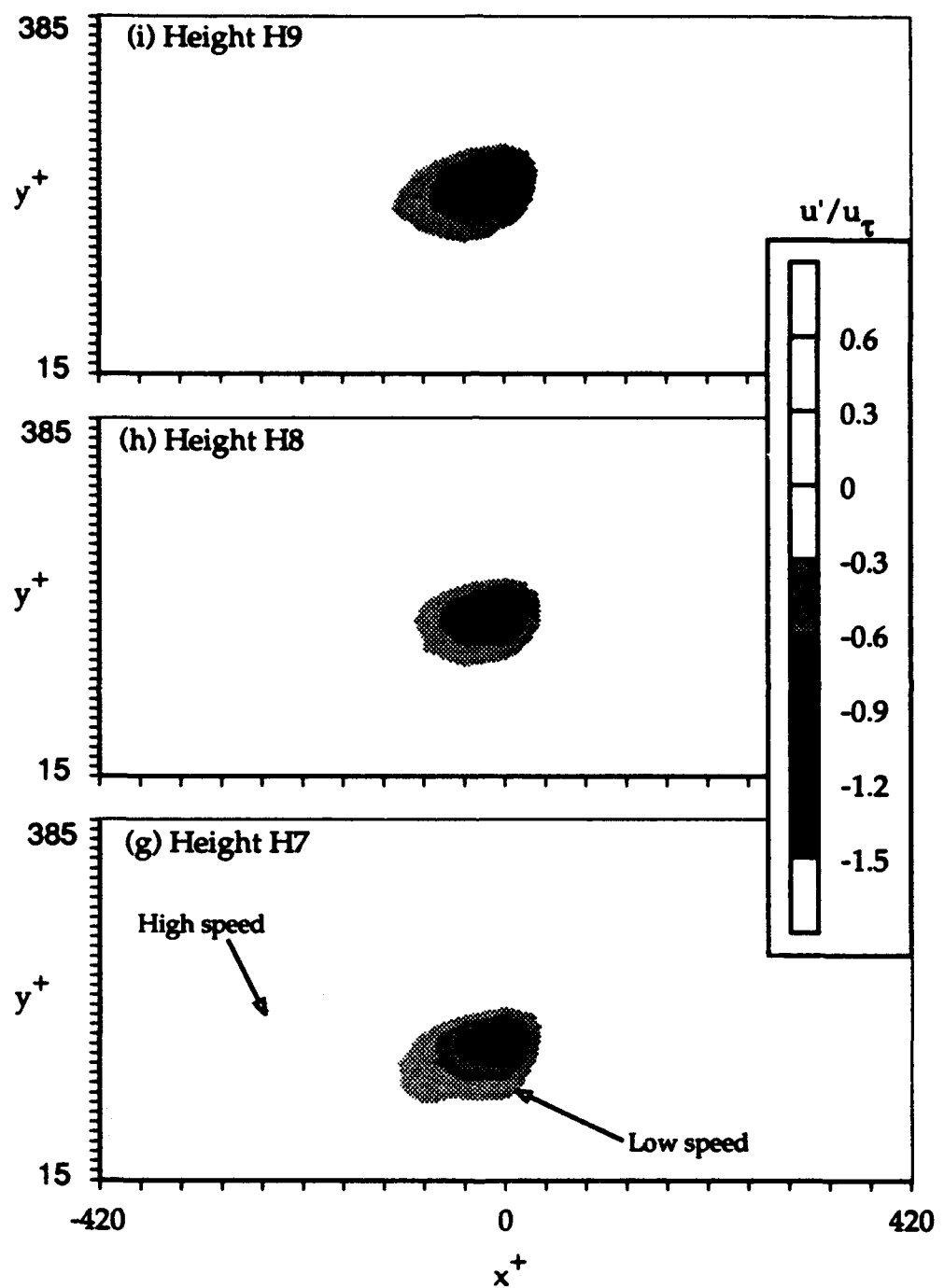


Figure 4.11 Continued.

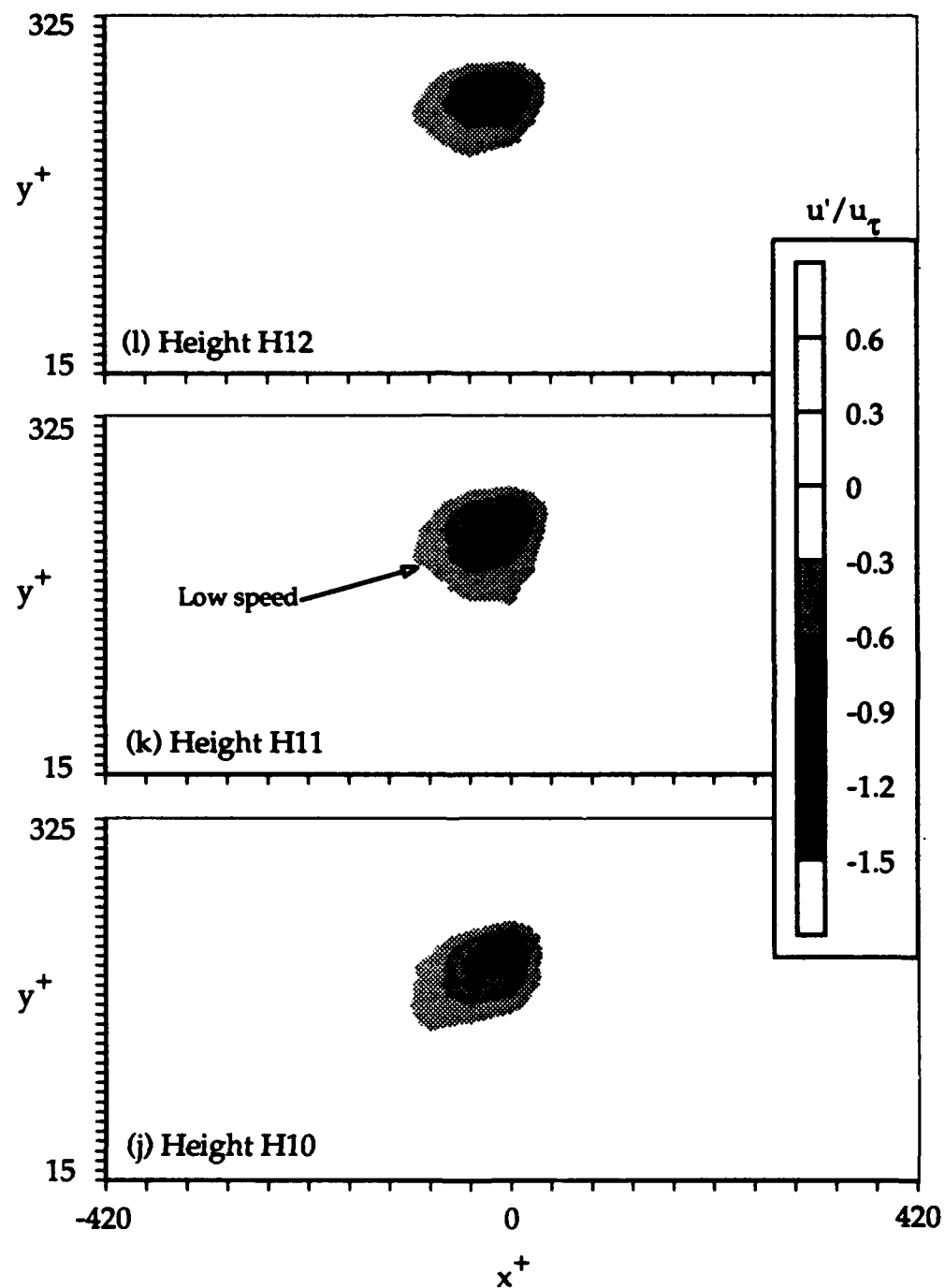


Figure 4.11 Continued.

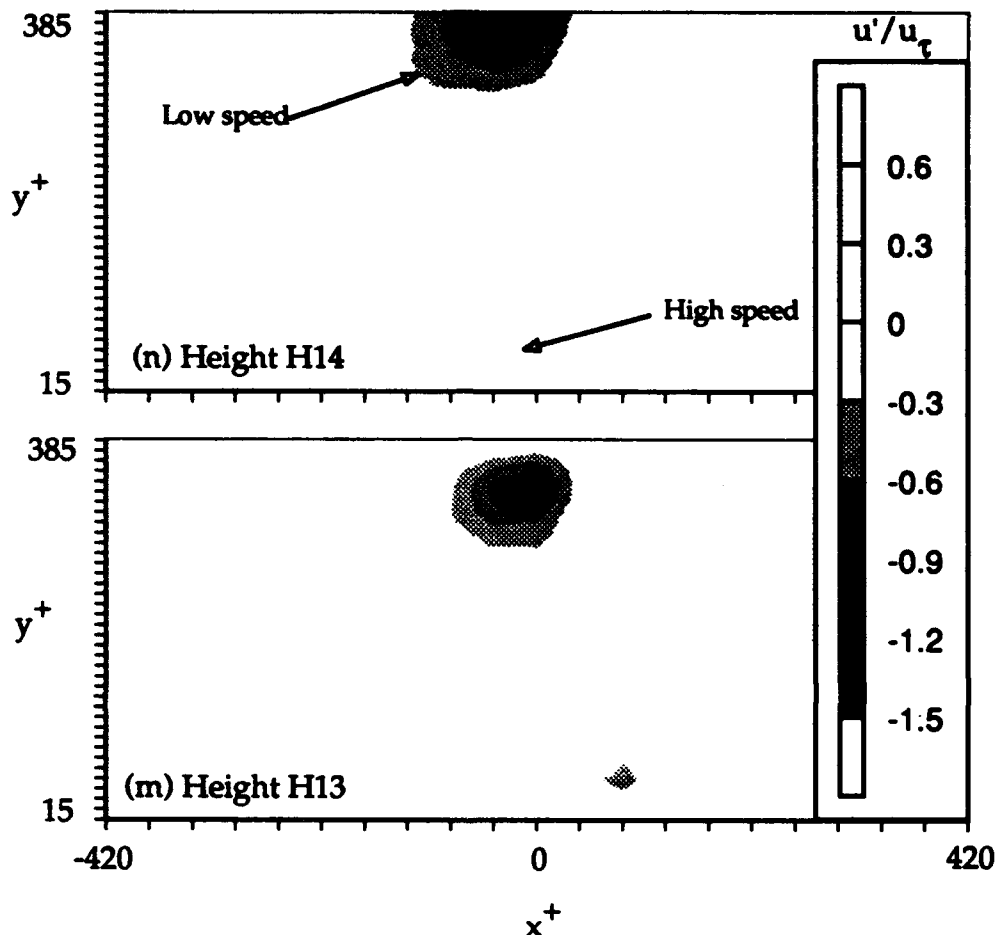


Figure 4.11 Continued.

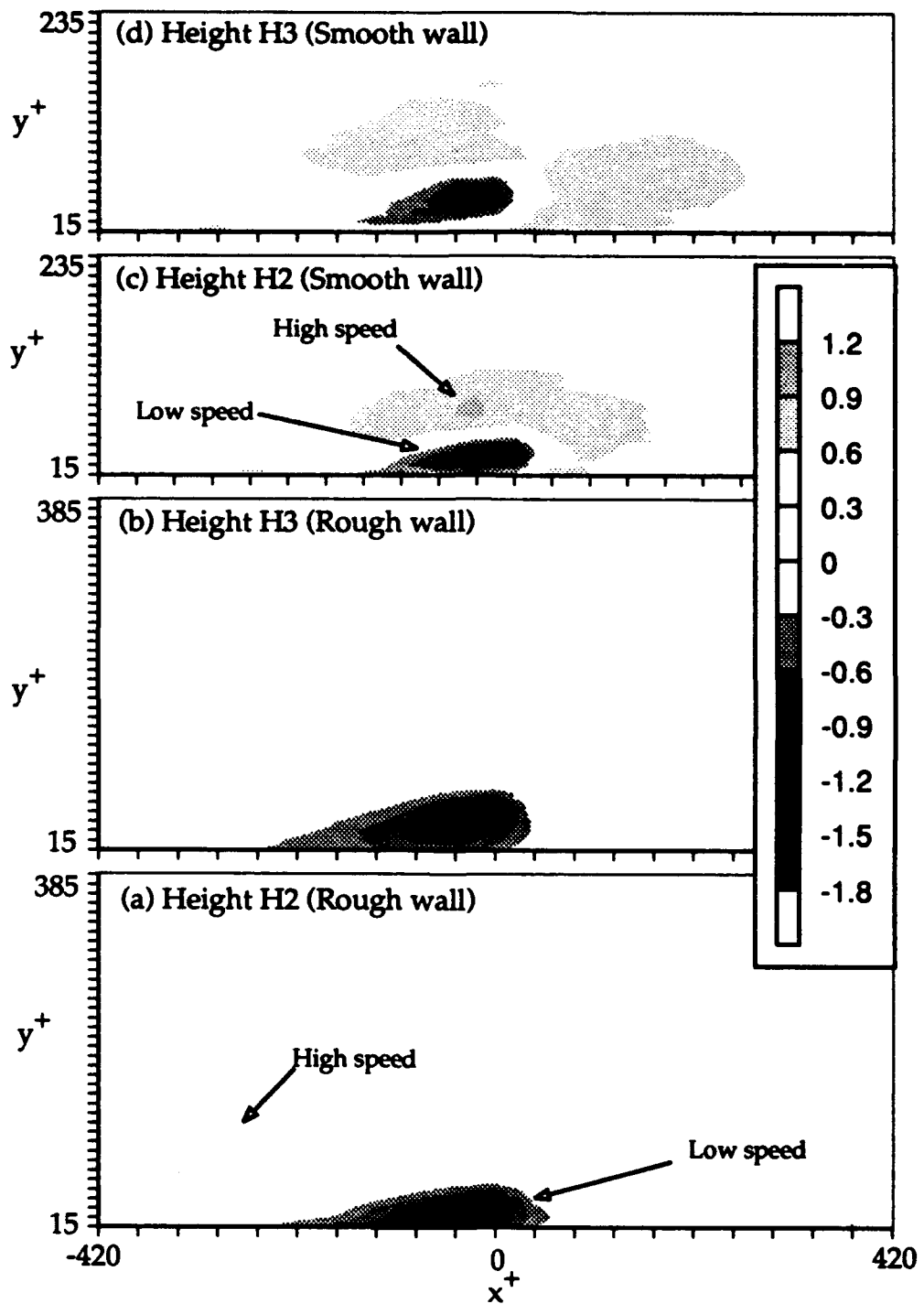


Figure 4.12 Smooth and rough wall low speed spatial events at heights H2 and H3.

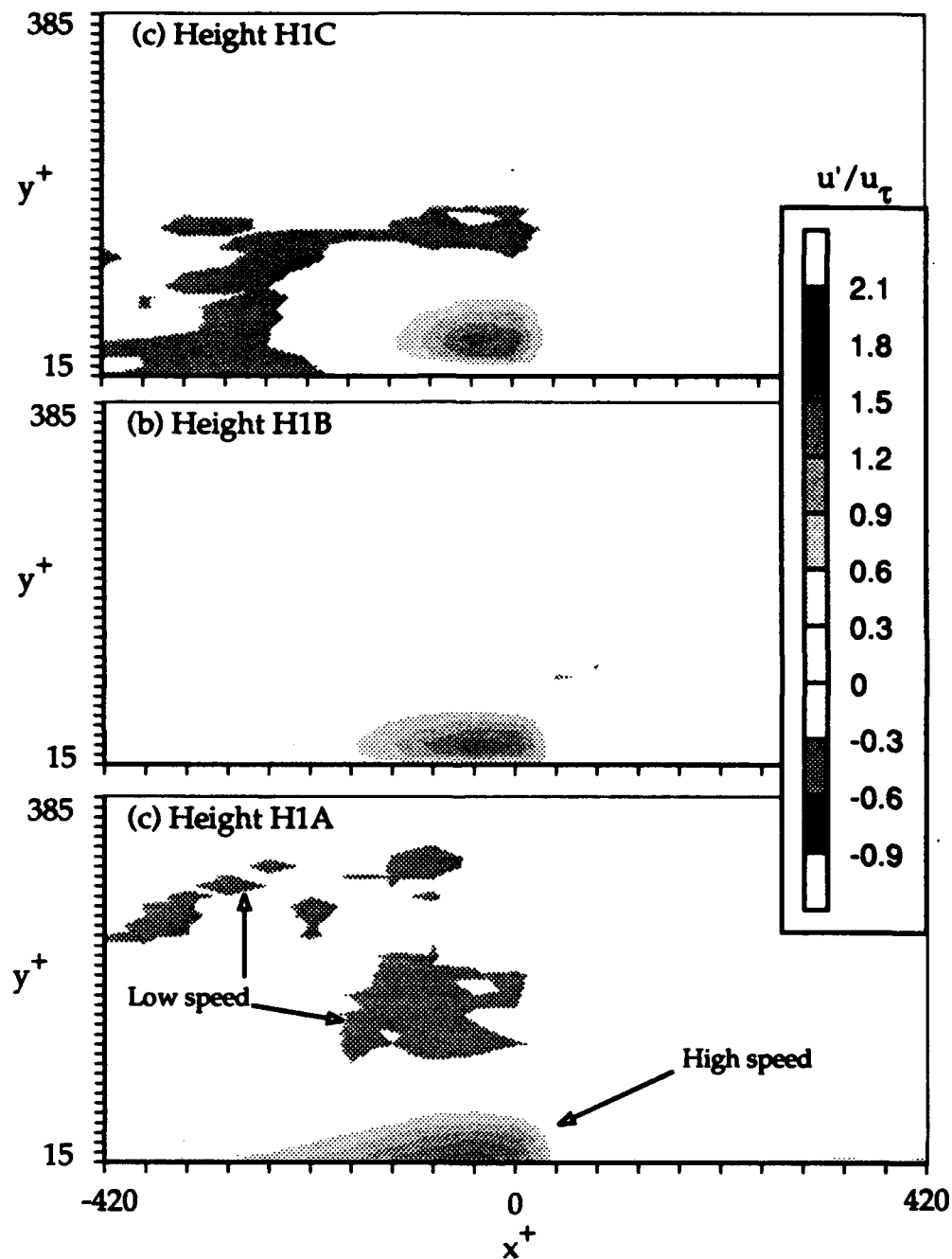


Figure 4.13 Conditional samples of high speed spatial events over the rough wall at different height categories based on their minimum height from the wall. See Table 4.4 for details.

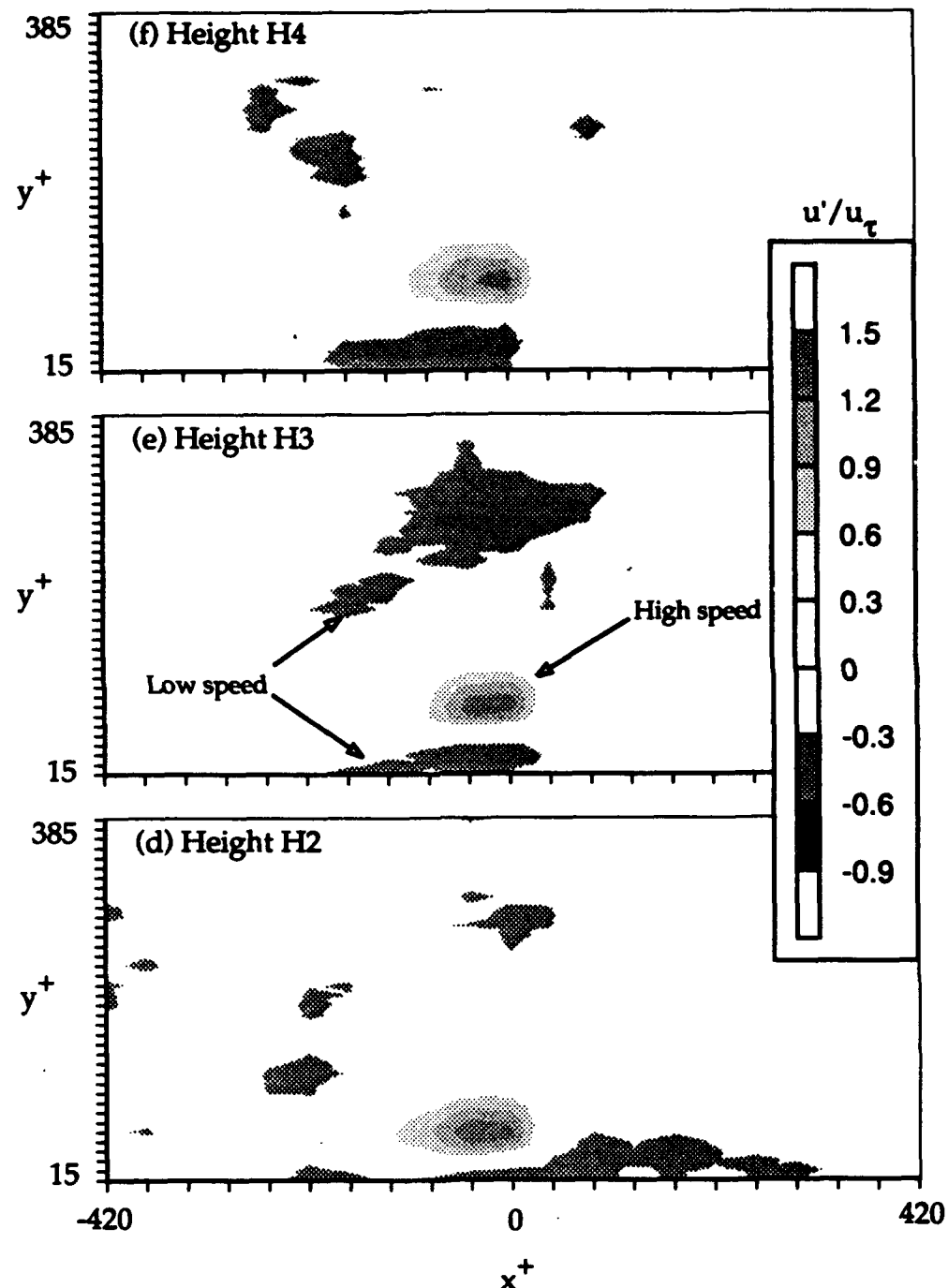


Figure 4.13 Continued.

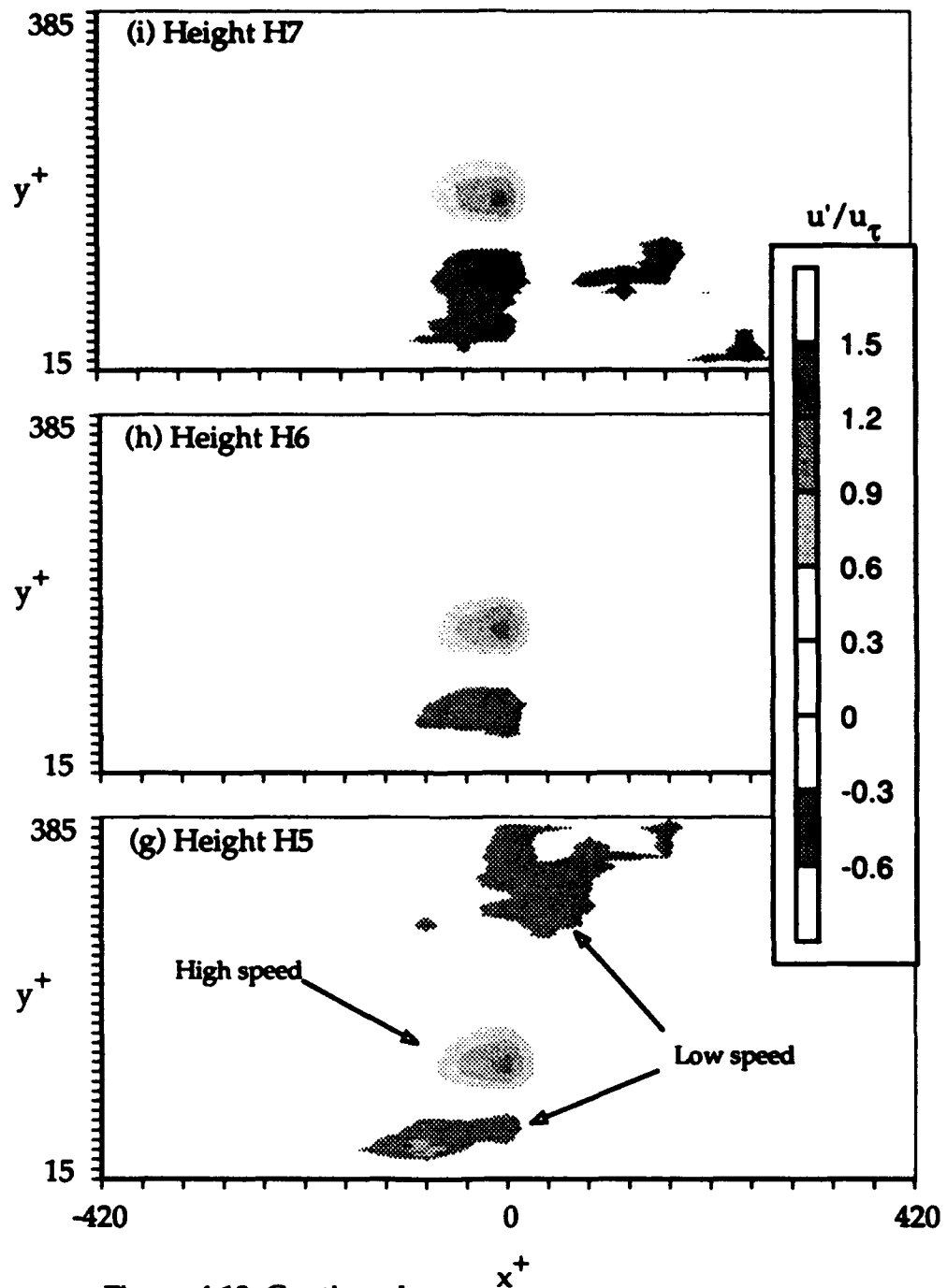


Figure 4.13 Continued.

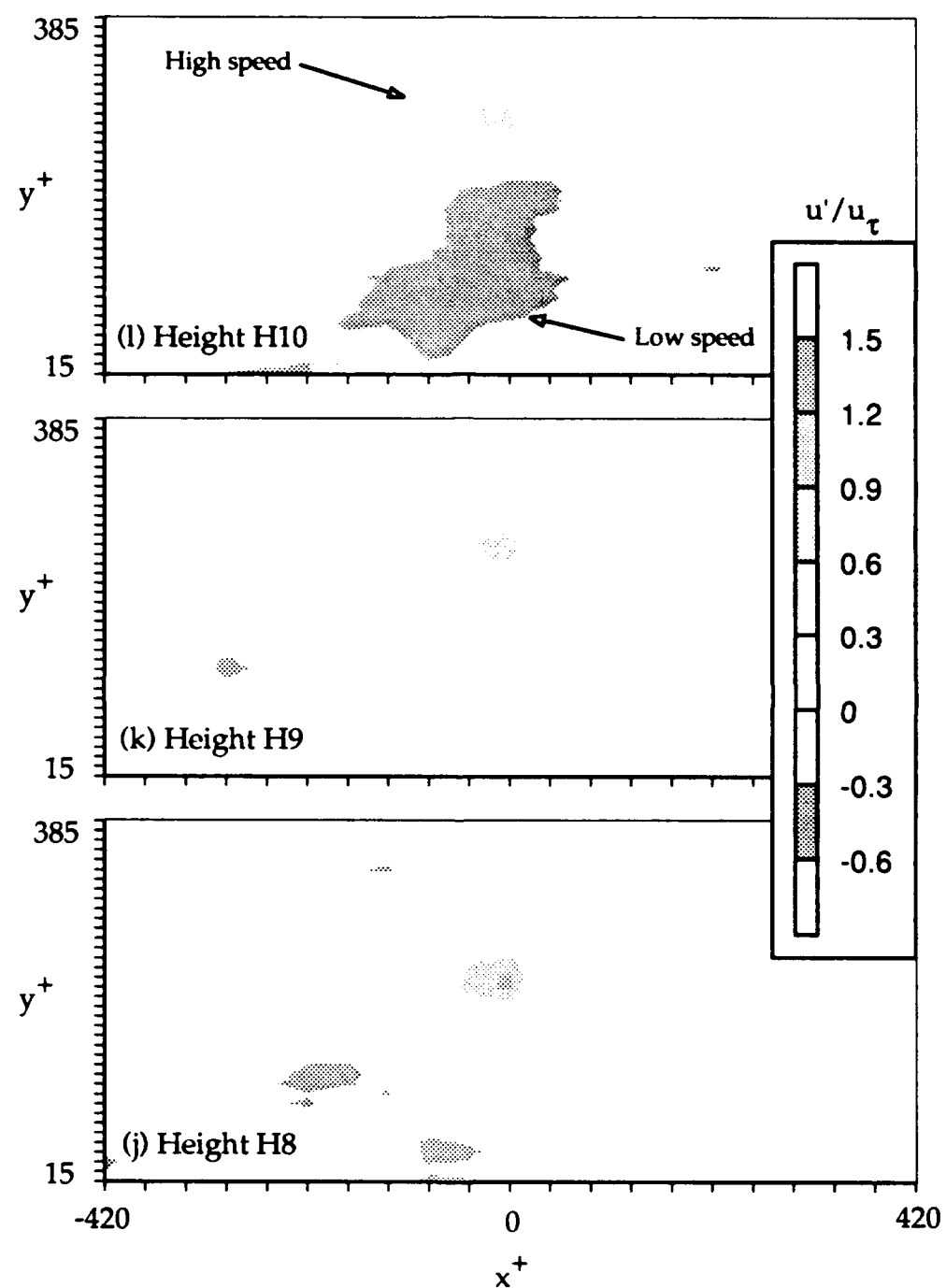


Figure 4.13 Continued.

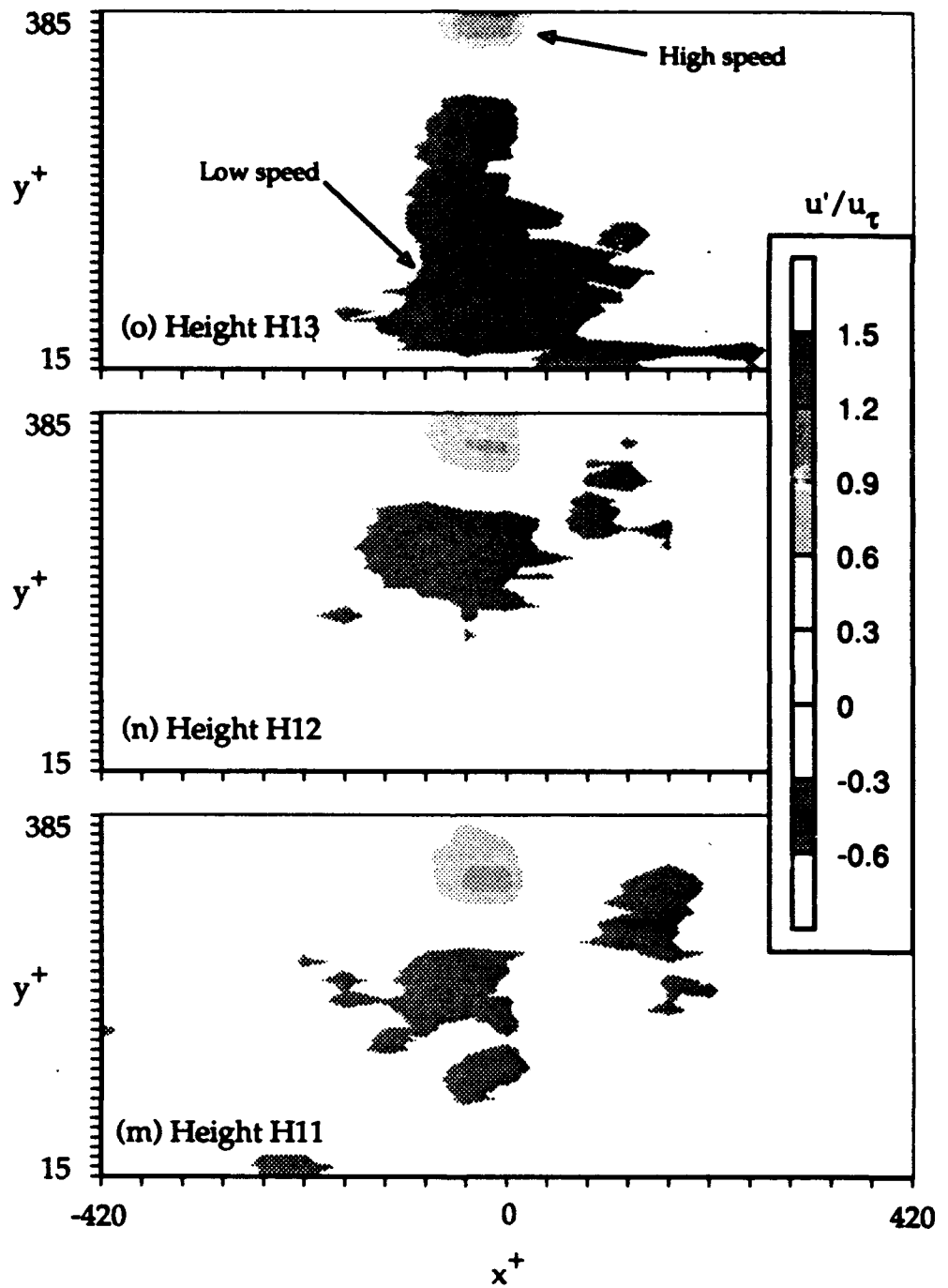


Figure 4.13 Continued.

## **CHAPTER 5**

### **CONCLUSIONS**

#### **5.1 Summary and conclusions**

The spatial detection technique has distinct advantages over single point detection techniques as bursts and sweeps can be categorized in terms of size and position of the event. Conditional sampling based on events of particular size and position from the wall significantly reduces smearing that necessarily occurs when events of all sizes and positions are grouped together, as with single point detection. Since the bursts increase in height as they eject from the wall, the height of the burst may be interpreted as indicating the stage of its development. By this interpretation conditional samples at increasing heights describes how the event evolves.

The presence of high speed structure along with the conditionally sampled low speed spatial event and vice versa, is a characteristic of the flow that is revealed by the spatial detection technique. Single point detection performed on the same data does not show any high speed structure associated with the burst because it groups events of all sizes and at different heights together. This

characteristic of the spatial detection scheme can give more insight into the interaction of coherent structures.

Over the smooth wall, the high speed fluid was seen above and in front of the low speed spatial event while it was near the wall, moving below it when it was detected at distances further away from the wall. This presence of high speed fluid, which originates in the outer part of the boundary layer, near the wall region suggests that there is interaction between the inner and outer parts of the boundary layer. The rough wall did not show any significant high speed fluid associated with the low speed spatial event. This is due to the fact that the bursting phenomenon over a rough surface is stimulated by the wall roughness unlike the smooth wall, where interaction with the high speed fluid from the outer region is speculated to initiate bursts.

The high speed spatial event, on the other hand, showed associated low speed fluid between itself and the wall when detected at heights close to the wall. This was true for both the rough and the smooth wall. This behavior is consistent with the fact that the low speed fluid originates from the wall region for both cases.

Compared to the smooth wall, the bursts were bigger and stronger over the rough wall, especially away from the wall. This is in agreement with Sabot, Saleh and Comte-Bellot (1977) who did space-time correlations and shear stress measurements in smooth

and rough wall pipes. They found that compared to smooth wall flows, ejections in rough wall pipe flows had larger mean periods of occurrence, larger mean time duration and length scale, and larger instantaneous shear stress peaks. Also, the presence of stronger low speed spatial events further away from the rough wall is consistent with Ligrani and Moffat (1986), who concluded that, because of more violent entrainment near a rough surface, the region of greatest mixing is moved further away from the wall and spread over a greater portion of the boundary layer. Grass (1971) found the ejection event at greater distances from the wall over rough surfaces, compared to the smooth wall.

The high speed spatial structure did not undergo any significant change over the rough surface. This is contrary to the study by Raupach (1981), who, from quadrant analysis, concluded that the magnitude of the sweep component (Reynolds stress generation associated with the fourth quadrant) increased with surface roughness.

At the same Reynolds number the proper scaling for burst and ejection frequencies from the smooth and rough wall is based on the outer variables, which is contrary to smooth wall results. Data over a range of Reynolds number has to be taken for a definite statement.

## 5.2 Recommendations for future work

The present study investigated the burst and sweep structures at two different surface roughness conditions. The measurements over the rough wall were made at a location where the flow had become self preserving, as required by the profile matching technique to predict the skin friction coefficient. This meant that changes in the characteristics of bursts and sweeps due to the rough surface had reached a state of equilibrium. Future studies should investigate the dynamics of the development in the characteristics of bursts and sweeps, which take place near the beginning of the rough surface. The dynamics will provide answers to the issues of cause and effect which are still not understood.

A major problem in studying coherent structures over rough surfaces is determining the skin friction coefficient. If measurements are to be made in the non-equilibrium region near the start of the roughness, a method of predicting the local skin friction coefficient which does not assume fully developed velocity profiles needs to be developed.

In the present study, outer variables were found to be the appropriate scaling parameters for collapsing the burst and ejection frequency data from the smooth and the rough wall. Further work, performed over a wide range of Reynolds numbers for different

roughness geometries and concentrations is required to make a definite statement about the scaling.

The controversy about the extent of interaction between the inner and outer regions of the boundary layer is still unresolved. To resolve this question, both regions have to be monitored simultaneously while different types of perturbations are applied to the boundary layer. The present study established that the scanning LDV along with the spatial detection technique is well suited for investigating the near wall structures. Experiments using the scanning LDV together with a flow visualization technique in the outer region will help resolve this controversy. Another possibility would be to increase the range of the scanning LDV and scan the whole boundary layer.

## **APPENDIX A**

### **UNCERTAINTY ANALYSIS**

Uncertainty of velocity contour levels, instantaneous scanning velocity measurements, normalized mean velocity measurements and probe volume position are presented in this appendix.

#### **A.1 Contour levels**

The uncertainty of velocity contour levels was determined by doing a conditional sampling analysis on random data. As the ensemble averages contain random events, the structures that result from the analysis are not significant. Results of this analysis are shown in Figure 2.11, which shows no significant structures in view with  $|u/u_\tau| > 0.3$ . Therefore the significant level for the velocity contour is  $|u/u_\tau| = 0.3$ .

#### **A.2 Instantaneous and mean velocity scanning measurements**

The scanning measurements include instantaneous velocity measurements and the normalized mean velocity values. The

uncertainty of instantaneous velocity measurements was calculated by scanning the freestream. As the turbulence intensity in the freestream is very low, a higher value is measured due to vibration during scanning measurements. The measured turbulence intensity was 1.6% compared to the actual 0.5%. This high value was a result of both scanning and signal processing uncertainties. Using Pythagorean summation, the uncertainty of the instantaneous scanning velocity measurements was calculated to be 3%.

The uncertainty of the normalized mean velocity measurements was influenced by the following factors: uncertainty in LDV measurements, uncertainty in calculation of  $u_T$ , bias error due to scanning and the precision error of the mean velocity measurements. The first two factors dominate the total uncertainty.

The uncertainty of LDV measurements consisted of bias uncertainty from error in determining the angle of the laser beams and the bias error due to the side wall curvature (which causes slight changes in the beam angle). The uncertainty of the angle between the beams was calculated to be 0.5%. The bias error due to the wall curvature was estimated to be less than 1%. Therefore the resulting bias uncertainty for the LDV measurements was 1.1%.

The uncertainty in calculating  $u_T$  depends on the uncertainty of locating the bottom wall and the uncertainty in the stationary

velocity measurements. The uncertainty in locating the wall was estimated to be  $\pm 0.1$  mm. The stationary velocity measurements have uncertainties depending on the turbulence intensity at that height. Each sample near the wall had a sampling time of 60 secs and a sample size of 12,288 measurements, with samples away from the wall having reduced sampling times with the same sample size. A range of uncertainties, from 3.5% near the wall, to 0.5% near the freestream were determined for the stationary mean velocity measurements. Uncertainties were determined by performing sequential perturbation, as outlined by Moffat (1988). The basic concept of this technique is as follows: two new values of  $u_T$  are calculated by perturbing each point, one at a time, by the uncertainty interval for the velocity measurement and wall location. The difference between the two new values and the original value for  $u_T$  represents the uncertainty in its measurement due to velocity measurement uncertainty and wall location uncertainty. By applying Pythagorean summation for all the points, and including the bias error due to LDV measurements, the total uncertainty in calculating  $u_T$  was  $\pm 2.7\%$ .

The precision error in the scanning mean velocity measurements was determined by finding the uncertainty of the mean from 18 subsets of the mean. The precision uncertainty in the

mean velocity was calculated to be 0.7%. The bias error due to scanning was estimated to be less than 0.5%.

From Pythagorean summation, the normalized mean velocity had a total bias error of  $\pm 2.9\%$  and a  $\pm 0.7\%$  precision error. Therefore the overall uncertainty of the normalized mean velocity was calculated to be  $\pm 3\%$ .

### A.3 Probe volume position

The probe volume position was calculated by scanning a hot wire placed at different heights in the scan range. Due to the phase lag between the actual position and voltage from the LVDT, two distinctly different voltages were measured during the upward and downward scans at the same position. Averages were calculated for the two voltages at each height and a straight line was fitted through them to give two equations for converting voltage to position; one for the upward scan and the other for the downward scan.

The total uncertainty of probe volume position depends on uncertainty of each height and voltage average used in the conversion equation, and the precision uncertainty of each individual voltage measurement. The uncertainty associated with each height was estimated to be  $\pm 0.1$  mm, while the uncertainty

associated with the voltage averages was  $\pm 0.003$  V. The precision uncertainty of each individual voltage measurement was 0.05 V. By using the method of sequential perturbation the total uncertainty in the probe volume was found to be  $\pm 0.2$  mm, which converts to a height of  $\pm 2$   $y^+$  units.

## APPENDIX B

### METHOD OF GROUPING EJECTIONS INTO BURSTS

The procedure of finding  $\tau_{\max}$ , the maximum time between ejections ( $T_E$ ) which are grouped into bursts, used in this study was similar to that used by Barlow and Johnston (1985). According to their study, the cut-off time can be obtained by plotting  $1 - F[T_E]$  against the ratio  $T_E/\bar{T}_E$ , where  $F[T_E]$  is the probability distribution of time between ejections and  $\bar{T}_E$  is the mean time between ejections.  $1 - F[T_E]$  is the same as the cumulative probability of a time being greater than a specific time between ejections,  $P[T > T_E]$ . In the present study  $P[T > T_E]$  was plotted in semi-log coordinates against the number of scans, as the data was arranged in terms of velocities at bin heights for successive scans in the y-t plane. Therefore, the cut-off time was calculated directly in terms of number of scans.

As the time between ejections from the same burst is less than those from different bursts, they follow different statistics as shown in Figure B.1. There are two distinct regions in the curve, corresponding to the time between ejections from the same burst (region 1) and time between ejections from different bursts

(region 2). By fitting a straight line through the linear portion of the data in region 2 and another, to the data in region 1,  $\tau_{\max}$  is found from their intersection. This process was repeated at each bin height to find  $\tau_{\max}$  which decreased with increasing height.

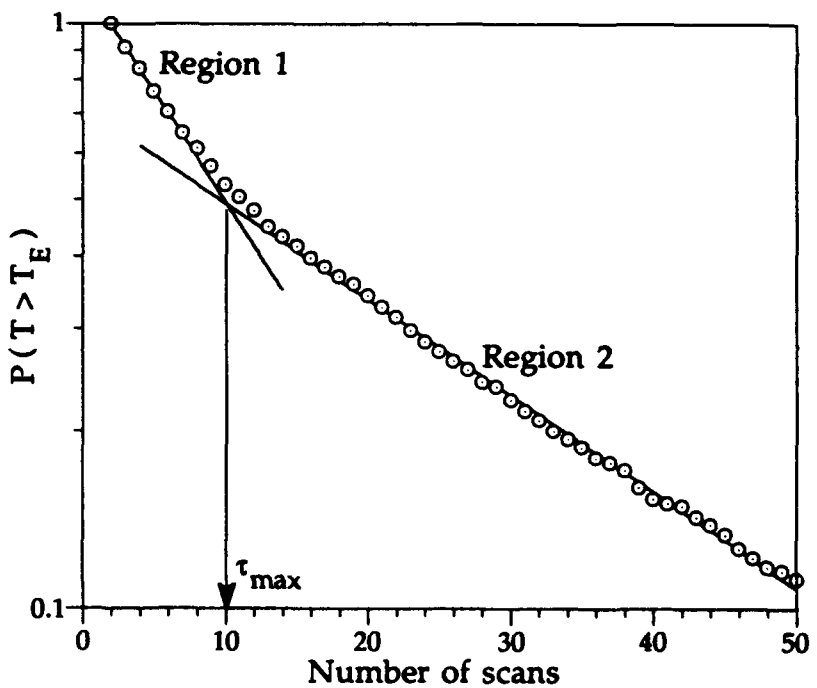


Figure B.1 Procedure of plotting time between ejections to get  $\tau_{\max}$  using the method by Barlow and Johnston (1985).

## APPENDIX C

### CALCULATION OF THE APPARENT ORIGIN

This technique was originally developed by Furuya et. al (1976). The underlying assumption in this method is to assume that the profile obeys equation (2.1) i.e. the log-law if the origin is chosen properly. Two sets of coordinate systems, one from the tip of the roughness elements and the other from the apparent origin are defined as shown in Figure C.1.

Let the displacement thickness in the  $y_T$  and  $y$  coordinates be defined as:

$$y = y_T + e,$$

$$\delta^* = \delta_T^* + \delta_e^*$$

and where,  $\delta_e^*$  is the displacement thickness in the range  $0 \leq y \leq e$ . Substituting these in (2.1), the following relationship is obtained:

$$\frac{U_\infty - U}{U_\tau} = -5.6 \log \frac{y_T U_\tau}{\delta_T^* U_\infty} - 5.6 \log \left[ 1 + \left( \frac{e U_\tau}{\delta_T^* U_\infty} \right) \left( \frac{y_T U_\tau}{\delta_T^* U_\infty} \right)^{-1} \right] + \left[ 5.6 \log \left( 1 + \frac{\delta_e^*}{\delta_T^*} \right) - 0.6 \right] \quad (C.1)$$

The above equation has been plotted for different values of the parameter  $(e U_\tau) / (\delta_T^* U_\infty)$  in Figure C.1. The last term in the above equation is a constant at a station and has been ignored in the plot

because it merely displaces the plot bodily. The measured profiles were superposed on Figure C.1 and 'e' was determined from the parameter which had the best agreement with the measurements.

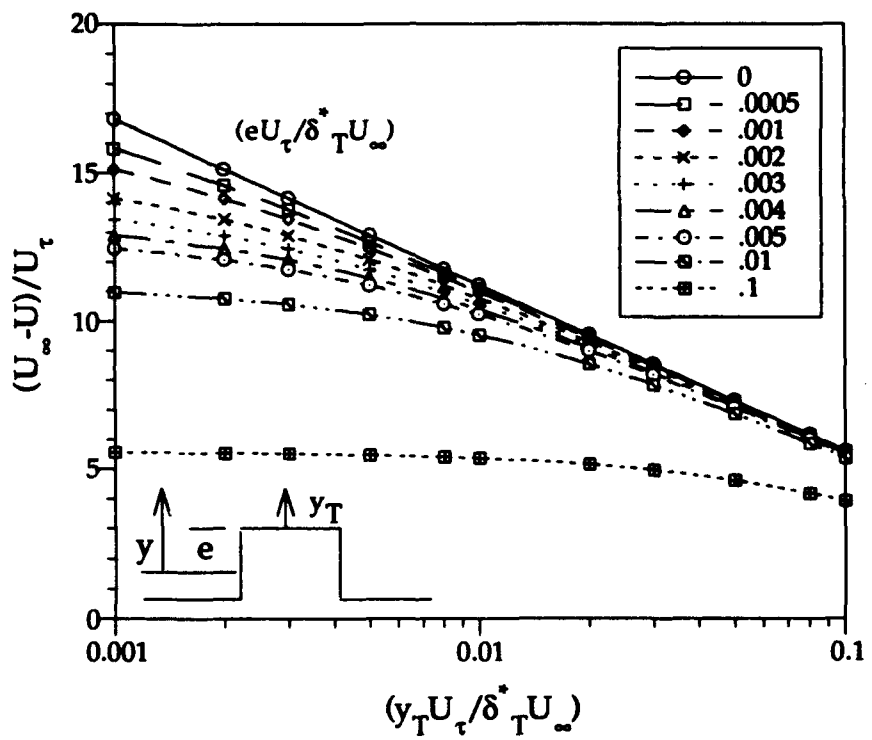


Figure C.1 Plot used to determine the error in origin by the method of Furuya et. al (1976).

## REFERENCES

Antonia, R. A. and Luxton, R.E. 1971 The response of a turbulent boundary layer to a step change in surface roughness, Part 1. Smooth to Rough. *J. Fluid Mech.* **48** (4), pp. 721-761.

Bandyopadhyay, P.R. 1987 Rough-wall turbulent boundary layers in the transition regime. *J. Fluid Mech.* **180**, pp. 231-266.

Barlow, R.S. and Johnston, J.P. 1985 Structure of turbulent boundary layers on a concave surface. *Report MD-47 under contract AFSOR-F49620-84-K-0004*, Stanford University.

Blackwelder, R.F. and Kaplan, R.E. 1976 On the wall structure of the turbulent boundary layer. *J. Fluid Mech.* **76**, 89.

Bogard, D.G. and Tiederman, W.G. 1987 Characteristics of ejections in turbulent channel flow. *J. Fluid Mech.* **179**, 1.

Bolton, B.L. 1990 Detection of coherent structures in a turbulent boundary layer using a scanning LDV sysstem. *M.S. Thesis*, The University of Texas at Austin.

Ciancarelli, C.R. 1988 Development of a scanner and signal processing system for laser anemometry. *M.S. Thesis*, The University of Texas at Austin.

Ciancarelli, C.R., Bogard, D.G., and Gan, C.L. 1988 Measurement precision of an LDV scanning system. *AIAA Symposium on Fluid Dynamics*, Reno, Nevada AIAA-88-0501.

Coles, D.E. and Hirst, E.A. (Eds.) 1969 Computation of turbulent boundary layers. *Proc. 1968 AFSOR-IFP-Stanford Conference*, 2, Stanford University.

Coughran, M.T. 1988 Interdependence of large and small scale structures in a turbulent boundary layer. *PhD dissertation*, The University of Texas at Austin.

Furuya, Y., Miyata, M. and Fujita, H. 1976 Turbulent boundary layer and flow resistance on plates roughened by wires. *J. Fluids Engineering* 98 (4), pp. 635-644.

Gan, C.L. 1989 The burst structure and its associated flow field in a turbulent boundary layer. *M.S. Thesis*, The University of Texas at Austin.

Gan, C.L. and Bogard, D.G. 1991 Study of the convection velocities of the burst and sweep structures in a turbulent boundary layer. *Eighth Symposium on Turbulent Shear Flows*, Munich, Germany.

Grass, A.J. 1971 Structural features of turbulent flow over smooth and rough boundaries. *J. Fluid Mech.* 50 (2), pp. 233-255.

Johansson, A.V., Alfredsson, P.H. and Eckelmann, H. 1987 On the evolution of shear-layer structures in near-wall turbulence. *Advances in Turbulence - Proc. 1st. European Turbulence Conference*, G. Comte-Bellot and J. Mathieu, eds., Springer-Verlag, pp. 383-390.

Ligrani, P.M. and Moffat, R.J. 1986 Structure of transitionally rough and fully rough turbulent boundary layers. *J. Fluid Mech.* 162, pp. 69-98.

Lu, L.J. and Smith, C.R. 1985 Image processing of hydrogen bubble flow visualization for determination of turbulence statistics and bursting characteristics. *Experiments in Fluids* 3, 349.

Lu, S.S. and Willmarth, W.W. 1973 Measurements of the structure of the Reynolds stress in a turbulent boundary layer. *J. Fluid Mech.* 60, 481.

Moffat, R.J. 1988 Describing the uncertainties in experimental results. *Experimental Thermal and Fluid Science* 1, pp. 3-17.

Nakagawa, H. and Nezu, I. 1977 Prediction of the contributions to the Reynolds stress from bursting events in open-channel flows. *J. Fluid Mech.* 80 (1), pp. 99-128.

Nychas, S.G., Hershey, H.C. and Brodkey, R.S. 1973 A visual study of turbulent shear flow. *J. Fluid Mech.* 61 (3), pp. 513-540.

Offen, G.R. and Kline, S.J. 1974 Combined dye-streak and hydrogen bubble visual observations of a turbulent boundary layer. *J. Fluid Mech.* 62 (2), 223.

Perry, A.E., Lim, K.L. and Henbest, S.M. 1987 An experimental study of the turbulence structure in smooth- and rough-wall boundary layers. *J. Fluid Mech.* 177, pp. 437-466.

Purtell, L.P., Klebanoff, P.S. and Buckley, F.T. 1981 Turbulent boundary layer at low Reynolds number. *Phys. Fluids* 24 (5), 802.

Raupach, M.R. 1981 Conditional statistics of Reynolds stress in rough-wall and smooth-wall turbulent boundary layers. *J. Fluid Mech.* 108, pp. 363-382.

Robinson, S.K. 1991 Coherent motions in the turbulent boundary layer. *Annual Rev. Fluid Mech.* 23, pp. 601-639.

Robinson, S.K., Kline, S.J. and Spalart, P.R. 1988 Quasi-coherent structures in the turbulent boundary layer: Part II. Verification and new information from numerically simulated flat-plate layer. Zoran P. Zaric Memorial International Seminar on Near-wall Turbulence, Dubrovnik, Yugoslavia.

Sabot, J., Saleh, I. and Comte-Bellot, G. 1977 Effects of roughness on the intermittent maintenance of Reynolds shear stress in pipe flow. *Phys. Fluids* 20 (10), 150.

Smits, A.J. and Wood, D.H. 1985 The response of turbulent boundary layers to sudden perturbations. *Ann. Rev. Fluid Mech.* 17, pp. 321-358.

Spalding, D.B. 1961 A single formula for the "law of the wall". *J. Appl. Mech.* 28 E(3), 455.